

DESIGN AND DEVELOPMENT OF BIOMIMETIC HYDROGEL INTERFACES FOR
ENHANCED BIOELECTRICAL SIGNAL ACQUISITION

By

Daniela Nikoloska

Bachelor of Science in Electrical Engineering
University of Nevada, Las Vegas
2023

A thesis submitted in partial fulfillment
of the requirements for the

Master of Science in Engineering – Electrical Engineering

Department of Electrical and Computer Engineering
Howard R. Hughes College of Engineering
The Graduate College

University of Nevada, Las Vegas
December 2025

©Copyright by Daniela Nikoloska, 2026
All Rights Reserved



Thesis Approval

The Graduate College
The University of Nevada, Las Vegas

November 10, 2025

This thesis prepared by

Daniela Nikoloska

entitled

Design and Development of Biomimetic Hydrogel Interfaces for Enhanced Bioelectrical
Signal Acquisition

is approved in partial fulfillment of the requirements for the degree of

Master of Science in Engineering – Electrical Engineering
Department of Electrical and Computer Engineering

Shengjie Zhai, Ph.D.
Examination Committee Chair

Alyssa Crittenden, Ph.D.
*Vice Provost for Graduate Education &
Dean of the Graduate College*

Biswajit Das, Ph.D.
Examination Committee Member

Mei Yang, Ph.D.
Examination Committee Member

Hui Zhao, Ph.D.
Graduate College Faculty Representative

ABSTRACT

Every second, human skin processes over one million sensory signals while maintaining properties such as electrical conductivity, mechanical adaptability, and regenerative capability that surpass all synthetic materials. Contemporary bioelectronic devices prove inadequate when contacting skin surfaces due to poor adhesion and electrical contact issues that prevent effective sensing. Despite advancements in wearable and bioelectronic technologies, current devices face major drawbacks when interfacing with human skin, particularly in maintaining firm adhesion, conformability, and low-noise electrical signal acquisition.

This research focuses on the development of a biomimetic hydrogel-based interface for bioelectronic sensing. Specifically, a hybrid hydrogel system composed of polydopamine (PDA)-doped polyacrylamide (PAM) was devised to mimic the functional characteristics of natural skin. Within this soft, hydrated matrix, various conductive and reinforcing dopants including iron oxide (Fe_3O_4) nanoparticles, graphene nanoplatelets (xGNP), and lithium chloride (LiCl) were incorporated in different combinations to tune the hydrogel's conductivity, and mechanical integrity while strengthening bioelectrical performance and skin adhesion.

The synthesized hydrogel composites were characterized using a suite of physicochemical, mechanical, and electrical tests to evaluate adhesion performance, stretchability, biocompatibility, and signal fidelity. Results demonstrated that a formulation containing all three dopants (Fe_3O_4 , xGNP, and LiCl) as the best-performing composition, achieving the most favorable balance. The results show that such a biomimetic hydrogel can enable more reliable long-term biosignal monitoring in applications such as wearable health devices, biomedical diagnostics, human-machine interfaces, and soft robotics.

ACKNOWLEDGEMENTS

I would first like to thank my advisor, Dr. Shengjie Zhai, for his belief in me. He welcomed me into his team when I was still an undergraduate student, and I will always be grateful that he took a chance on me so early. Thank you for allowing me to contribute to so many projects and for bringing humor into every conversation. Your enthusiasm and positive spirit made even the toughest moments feel manageable.

Next, I would like to thank my committee members Dr. Hui Zhao, Dr. Mei Yang, and Dr. Biswajit Das. Thank you for your guidance, for answering every question I had along the way, and for believing in my work.

Thank you to my friend Bryan Jacome, who was not only my ever-patient test subject for the ECG signal acquisition testing, but also my trusted chemistry guru. I'm grateful for your explanations and for allowing me to use the scale in your lab when ours decided not to cooperate.

To my parents, I extend my sincere gratitude for your steady support, your many sacrifices, and enduring belief in me. Your encouragement meant everything as I worked toward this goal. To my sisters, my lifelong cheer team, thank you for being there every step of the way. And to Max, thank you for helping me stay grounded, all while completing your own thesis alongside me.

I am also grateful to the friends I've made during my years living in Las Vegas and for the coworkers who supported me along the way. Your presence made this process more enriching and memorable. I'll end with a quote from a world I love:

“All we have to decide is what to do with the time that is given to us”

– J.R.R. Tolkien

TABLE OF CONTENTS

ABSTRACT.....	iii
ACKNOWLEDGEMENTS	iv
LIST OF TABLES.....	ix
LIST OF FIGURES	x
LIST OF ABBREVIATIONS.....	xvi
CHAPTER 1: INTRODUCTION.....	1
1.1 Background and Motivation	1
1.2 Research Objectives.....	2
CHAPTER 2: LITERATURE REVIEW.....	4
2.1 Human Skin Structure and Mechanisms.....	4
2.2 Previous Research on Electronic Skin Platforms.....	5
2.2.1 Article by Zhu et al.	5
2.2.2 Article by Roy et al.	6
2.3 Hydrogel-Based Sensing Platforms	7
2.3.1 Multi-Component Conductive Hydrogel Composites (PDA-PAM Systems).....	7
2.3.2 Modulus Matching and Electrical Bio Integration.....	10

2.4 Mechanical Testing Approaches	12
CHAPTER 3: MATERIALS AND METHODOLOGY	13
3.1 Reagents and Experimental Materials	13
3.2 Synthesis of Hydrogels: PDA-PAM and Fe ₃ O ₄ /xGNP/LiCl (2.8 wt%)	13
3.2.1 Synthesis of PDA-PAM Hydrogel	13
3.2.2 Addition of Fe ₃ O ₄ , xGNP, and LiCl Dopants	14
3.3 Structural Characterization via SEM	17
3.4 Self-Healing	17
3.5 Mechanical Testing: Tensile, Compression, and Adhesion	18
3.5.1 Tensile	20
3.5.2 Compression	21
3.5.3 Adhesion	21
3.6 Electrical Testing	22
3.6.2 Conductivity	22
3.6.3 Chronoamperometry	23
3.6.4 Cyclic Voltammetry	23
3.7 Electrophysiological Signal Acquisition (ECG Signals)	23
3.7.1 Electrode Fabrication and Experimental Setup	23
3.7.2 ECG Signal Quality Criteria and Metrics	26

CHAPTER 4: RESULTS AND DISCUSSION.....	28
4.1 Synthesis of Hydrogels: PDA-PAM and Fe₃O₄/xGNP/LiCl (2.8 wt%) Results	29
4.1.1 PDA-PAM Hydrogel Synthesis Results.....	29
4.1.2 Addition of Fe ₃ O ₄ , xGNP, and LiCl Dopants Results	30
4.3 Self-Healing Performance	34
4.4 Mechanical Properties: Tensile, Compression, and Adhesion	35
4.4.3 Adhesion Results.....	46
4.5 Electrical Testing Evaluation	48
4.5.1 Conductivity Results	48
4.5.2 Chronoamperometry Results	51
4.5.3 Cyclic Voltammetry Results.....	53
4.6 Physiological Signal Sensing (ECG Signals).....	59
4.6.1 Control Group Results	59
4.6.2 Experimental Group Results	69
4.6.3 Comparison Results	79

CHAPTER 5: CONCLUSION	92
5.1 Summary of Findings	92
5.2 Limitations.....	95
5.3 Future Research Directions.....	96
APPENDIX A: BUILD AND CONTROL INFORMATION OF TENSILE DEVICE	98
REFERENCES.....	103
CURRICULUM VITAE	107

LIST OF TABLES

Table 3.1: Composition summary of PDA–PAM-based hydrogel variants	15
Table 4.1: Photographs of cured hydrogel samples The xGNP/LiCl 2.8% sample failed to hold shape.	30
Table 4.3: Performance summary of test 2.....	87
Table 4.4: Performance summary of test 3.....	91
Table A.1: Electrical connections between the LabJack T7-Pro, stepper driver, and load cell....	99

LIST OF FIGURES

Figure 2.1. Structural schematic of human skin layers.	4
Figure 2.2 Schematic of the triple-network hydrogel architecture designed by Roy et al., integrating defect-rich MoS ₂ , PDA nanoparticles, and thiolated pullulan (Pul-SH) [6].	6
Figure 2.3. – Schematic of mussel foot adhesion mechanism and catechol-rich protein secretion in an underwater environment (created with BioRender.com).	8
Figure 3.1. Schematic of the synthesis route for the Fe ₃ O ₄ /LiCl/xGNP-doped PDA–PAM composite hydrogel (created with BioRender.com).	17
Figure 3.2 Tensile device apparatus.	19
Figure 3.3 Stress-strain relationship demonstrating characteristic properties from tensile tests.	20
Figure 3.4 The control electrodes (left strip) contain the red-tinted PDA–PAM hydrogel, and the optimal electrodes (right strip) contain the black composite hydrogel.	24
Figure 3.5 (Left) Schematic of the standard 12-lead ECG electrode configuration, including four limb leads (RA, LA, RL, LL) and six precordial chest leads (V1–V6). (Right)	25
Figure 3.6 Schematic of a typical ECG signal with labeled P-QRS-T components.	27
Figure 4.1 Visual confirmation of dopamine polymerization. Solution before (left) and after one hour of oxidation (right).	29
Figure 4.3 SEM images of hydrogel internal morphology: a) PAM, b) PDA–PAM, and c) Fe ₃ O ₄ /xGNP/LiCl (2.8 wt%) @ PDA–PAM.	33

Figure 4.4 Demonstration of self-healing in the Fe ₃ O ₄ /LiCl/xGNP-doped PDA–PAM composite hydrogel.	34
Figure 4.5 Photographic comparison of hydrogels during tensile loading.	35
Figure 4.6 Tensile stress–strain curves of all the hydrogel formulations except for xGNP/LiCl 2.8 %.	36
Figure 4.7 Tensile modulus of the hydrogel formulations.	38
Figure 4.8 Tensile strength (ultimate stress) of the hydrogel formulations	39
Figure 4.9 Tensile toughness (energy absorption, area under the stress–strain curve) of the hydrogel formulations.....	40
Figure 4.10 Photographs of the compression testing setup.....	41
Figure 4.11 Compressive stress–strain curves for each hydrogel group.....	42
Figure 4.12 Compressive modulus, or average stiffness, of each hydrogel formulation.....	43
Figure 4.13 Compressive strength, the maximum stress before failure, of each hydrogel composite.	44
Figure 4.14 Adhesion demonstration of the PDA–PAM control group (top panel) and Fe ₃ O ₄ /xGNP/LiCl PDA–PAM experimental group (bottom panel).....	46
Figure 4.15 Average DC conductivity (σ_0) of doped PDA–PAM hydrogel formulations extracted from impedance spectroscopy.....	48

Figure 4.16 compares the best-performing LiCl-2.8% hydrogel directly to the PDA–PAM and PAM controls.	50
Figure 4.17 presents the mean chronoamperometric (CA) responses for all experimental and control hydrogel formulations, averaged over four replicates per group.....	51
Figure 4.18 Cycle 3 - Average cyclic voltammetry curves comparing all experimental hydrogel variants.....	53
Figure 4.19 CV comparison of LiCl-doped versus control hydrogels (cycle 3). The.....	54
Figure 4.20 Anodic peak currents ($I_{p,c}$) derived from CV measurements.	56
Figure 4.21 Cathodic peak currents ($I_{p,c}$) derived from CV measurements	57
Figure 4.22 Control Group Test 1 – At Rest. (12 Lead Stacked ECG) Segment shown corresponds to $t = 8$ s	59
Figure 4.23 Control Group Test 1- At Rest (ECG Grid View) Segment shown corresponds to $t = 8$ s.....	60
Figure 4.24 Control group test 1 - At rest (power spectral density of lead II). Segment shown corresponds to $t = 8$ s.	61
Figure 4.25 Control group test 2 - squat (12 lead stacked ECG). Segment shown corresponds to $t = 13$ s.....	62
Figure 4.26 Control group test 2 - squats (ECG grid view). Segment shown corresponds to $t = 13$ s.....	63

Figure 4.27 Control group test 2 - squats – (power spectral density of lead II). Segment shown corresponds to t =13 s.	64
Figure 4.28 Control group test 3 - push ups (12 lead stacked ECG) Segment shown corresponds to t = 20 s.....	65
Figure 4.29 Control group test 3 - push-ups (ECG grid view). Segment shown corresponds to t = 20 s.....	66
Figure 4.30 Control group test 3 – push-ups (power spectral density of lead II) Segment shown corresponds to t = 20 s.	67
Figure 4.31 Experimental group test 1 – at rest (12 lead stacked ECG). Segment shown corresponds to t =7 s	69
Figure 4.32 Experimental group test 1- at rest (ECG grid view). Segment shown corresponds to t =7 s.....	71
Figure 4.33 Experimental group test 1 – at rest (power spectral density of lead II) Segment shown corresponds to t = 7 s.....	72
Figure 4.34 Experimental group test 2 – squats (12 lead stacked ECG). Segment shown corresponds to t = 93 s.	73
Figure 4.35 Experimental group test 2 - squats (12 lead stacked ECG). Segment shown corresponds to t = 93 s.	74
Figure 4.36 Experimental group test 2 - squats (power spectral density of lead II). Segment shown corresponds to 93 s	75

Figure 4.37 Experimental group test 3 – push-ups (12 lead stacked ECG). Segment shown corresponds to $t = 0$ s.	76
Figure 4.38 Experimental group test 3 – push-ups (ECG Grid View). Segment shown corresponds to $t = 0$ s	77
Figure 4.39 Experimental group test 3 – push-ups (power spectral density of lead II). Segment shown corresponds to $t = 0$ s.....	78
Figure 4.40 Test 1- at rest (stacked comparison graph)	80
Figure 4.41 Test 1- at rest (12-lead grid comparison graph).....	81
Figure 4.42 Test 1- at rest (PSD lead II comparison graph).....	82
Table 4.2 Performance summary of test 1.	83
Figure 4.43 Test 2- squats (stacked comparison graph).....	84
Figure 4.44 Test 2- squats (12-lead grid comparison graph).....	85
Figure 4.45 Test 2- squats (PSD lead II comparison graph)	86
Figure 4.46 Test 3- push-ups (stacked comparison graph).....	89
Figure 4.47 Test 3- push-ups (12-lead grid comparison graph).....	90
Figure 4.48 Test 3- push-ups (PSD lead II comparison graph).....	90
Figure A.1 Snapshot of the complete LabVIEW block diagram for the custom tensile testing VI.	101

Figure A.2 Screenshot of the LabVIEW VI front panel during a test. 102

LIST OF ABBREVIATIONS

EEG	Electroencephalography
EMG	Electromyography
ECG	Electrocardiography
CH	Conductive Hydrogel
PAM	Polyacrylamide
PDA	Polydopamine
PI	Polyimide
ECM	Extracellular Matrix
DC	Direct Current
LiCl,	Lithium chloride
xGNP	Graphene nanoplatelets
Fe ₃ O ₄	Iron Oxide
NPs	Nanoparticles
DA	Dopamine hydrochloride
AM	Acrylamide
APS	Ammonium persulfate
BIS	N, N'-methylenebisacrylamide

NaOH	Sodium hydroxide
TEMED	Tetramethylethylenediamine
UTS	Ultimate Tensile Strength
PANNI	Polyaniline
CA	Chronoamperometry
CV	Cyclic Voltammetry

CHAPTER 1: INTRODUCTION

1.1 Background and Motivation

A non-invasive window into human internal physiology is attainable through the capture of bioelectrical signals, providing reliable insight into overall health. These signals reveal important information about neural, cardiac, muscular, and dermal activity. Bioelectrical signals such as those recorded in electroencephalography (EEG), electromyography (EMG), and electrocardiography (ECG) [1]. The effectiveness of such monitoring, however, is contingent upon the quality of contact between biological tissue and the sensing material. Conventional electrode systems often struggle to maintain signal fidelity under dynamic biological conditions, such as perspiration, deformation, and motion. These drawbacks reduce their viability in biomedical contexts. An alternative approach lies in the use of conductivity hydrogels due to their mechanical properties that mimic natural tissue [2].

Composed of water-swollen polymer networks, these materials maintain conformal contact through their viscoelastic and hydration-driven behavior [3]. The water-rich composition of Conductive hydrogels allows for continuous ionic transport, supporting stable conductivity. These attributes reduce motion artifacts and interfacial impedance, two persistent problems in dry electrodes [1],[4]. Dry electrodes tend to detach easily or require frequent repositioning, leading to inconsistent readings. An added benefit of conductive hydrogels comes from their extracellular matrix (ECM) mimicking network, further improving tissue compatibility and lowering the potential for inflammation during prolonged wear [5]. Numerous research groups have developed polydopamine-based conductive hydrogels, demonstrating that polydopamine-doped polyacrylamide (PDA-PAM) systems achieve strong tissue adhesion, stable electrical conductivity, and reliable long-term performance [2],[4]-[8].

Commercial tensile testers, while highly accurate, are often costly, difficult to modify, and ill-suited for low modulus, hydrated samples like conductive hydrogels [9]. Open-source tensile systems have been developed using accessible components such as DC motors, load cells, and programmable microcontrollers. This work designs and develops both a polydopamine-based hydrogel system and a custom tensile testing platform to characterize soft materials.

1.2 Research Objectives

The primary objective of this work is to develop and evaluate a hydrogel platform suitable for wearable bioelectronic sensing. To this end, two specific aims were pursued. The process can be broken down into the following steps:

- (a) Design and fabricate a custom tensile testing device optimized for soft, hydrated materials.
- (b) Integrate a microcontroller-driven actuator, load cell, and real-time data acquisition module.
- (c) Synthesize a PDA-PAM hydrogel composite incorporating LiCl, xGNP, and Fe₃O₄ nanoparticles with tunable electrical conductivity, mechanical compliance, and strong adhesion to biological surfaces.
- (d) Characterize the hydrogel's properties through mechanical testing, electrochemical testing, and twelve-lead ECG recording under resting and motion states.

Both components were evaluated independently and in tandem to confirm functionality for soft material testing.

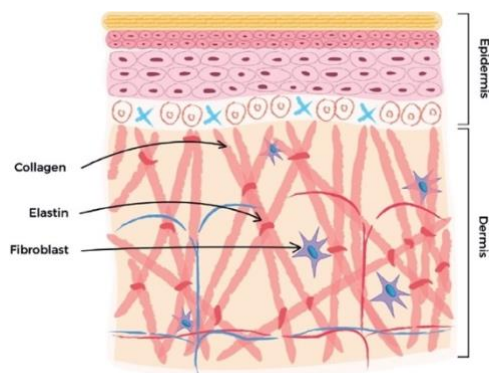
1.3 Thesis Organization

This thesis is structured into five chapters that collectively address the dual aims of developing conductive hydrogels for electronic skin and creating a custom tensile testing system. Chapter 1 introduces the research motivation and objectives to establish the problem statement. Chapter 2 provides a literature review contextualizing the significance of hydrogel-based electronics and custom testing infrastructure. Chapter 3 covers materials and methods in full detail. It begins with the chemical components and fabrication process for the PDA–PAM hydrogel and its modified variants incorporating LiCl, xGNP, and Fe₃O₄. The chapter then describes the structure property characterization workflow, including SEM imaging, tensile testing through the custom-built device, and electrical testing via conductivity, chronoamperometry, and cyclic voltammetry. The final section explains how twelve-lead ECG testing was used to evaluate the hydrogel’s performance under both static and motion conditions. Chapter 4 reports the corresponding results and discussion. Chapter 5 consolidates the study’s findings, addresses limitations in the experimental approach, and recommends next steps for optimizing hydrogel interfaces in wearable sensing platforms.

CHAPTER 2: LITERATURE REVIEW

2.1 Human Skin Structure and Mechanisms

Human skin is a multi-layered organ composed of the epidermis, dermis, and hypodermis. It serves as a mechanical and biochemical barrier that protects internal tissues from physical trauma, pathogens, UV exposure, and dehydration [10]. The dermis contributes most to mechanical strength due to its dense collagen network, while the hypodermis provides cushioning and thermal insulation. Skin exhibits nonlinear, viscoelastic behavior with anisotropic mechanical properties. Reported values of Young's modulus vary significantly across different anatomical locations, typically ranging from 0.1 to 2 MPa, with localized regions exhibiting moduli as low as 25-200 kPa. More specifically, the Young's modulus of human skin has been measured at 29 ± 88 kPa, while muscle tissue exhibits a modulus of 10 ± 106 kPa [2]. The epidermis can withstand tensile strains up to ~ 30 before failure [2]. This strain tolerance is supported by the layered architecture of skin. Dense collagen bundles in the dermis and hydrated structures in the epidermis work together to absorb strain, as illustrated in Figure 2.1.



©MINERVA Research Labs. all rights reserved

Figure 2.1. Structural schematic of human skin layers. Fibroblasts in the dermis generate collagen and elastin networks that define the tissue's mechanical framework. Adapted from MINERVA Research Labs Ltd [11].

Skin performs multimodal sensing, including strain, pressure, and temperature across the skin's depth. Mechanoreceptors embedded within the dermis and epidermis transduce mechanical deformation into electrical signals [11]. Hydration status directly influences ionic conductivity and tissue responsiveness. The hydrated matrix of the skin not only provides mechanical resilience but also maintains the electrochemical environment necessary for signal transmission. Together, these features establish skin as a mechanically resilient and electrochemically active interface.

2.2 Previous Research on Electronic Skin Platforms

Electronic skins replicate the sensing and mechanical behavior of human skin through flexible, low-profile materials. Conventional platforms use substrates like PI, PET, and PDMS due to their durability [12]. However, their moduli typically in the MPa to GPa range remain orders of magnitude higher than those of human tissue. This mechanical mismatch can lead to interfacial strain accumulation, signal degradation, and delamination under dynamic loading.

2.2.1 Article by Zhu et al.

To overcome this mechanical mismatch, researchers have turned to soft materials such as hydrogels and nanocomposite elastomers. These alternatives offer low modulus, high hydration, and ionic conductivity for tissue-level integration [6]. Among these, PDA has attracted interest for its dual role in adhesion and electronic stability. Zhu et al designed a sandwiched strain sensor composed of Ag nanoparticles embedded between dual-layer polyurethane textiles [13]. The fibrous configuration achieved stretchability above 200% while maintaining high gauge sensitivity across the full strain window. This sensor demonstrated low hysteresis and real-time responsiveness under complex loading modes, including twisting, compression, and bending. Although this design reduces modulus mismatch, the system still relies on dry contact, ultimately leading to a limitation in bioenvironments.

2.2.2 Article by Roy et al.

Roy et al. developed a 3D-printed, triple-network hydrogel incorporating PDA and defect-rich MoS₂ nanosheets, resulting in a matrix that is conductive, stretchable, and dermally compliant [6]. This system achieved multimodal responsiveness while preserving structural integrity under cyclic load. The underlying crosslinking architecture is depicted in Figure 2.2, illustrating the coordinated role of Michael addition, ionic bonding, and nanosheet interactions.

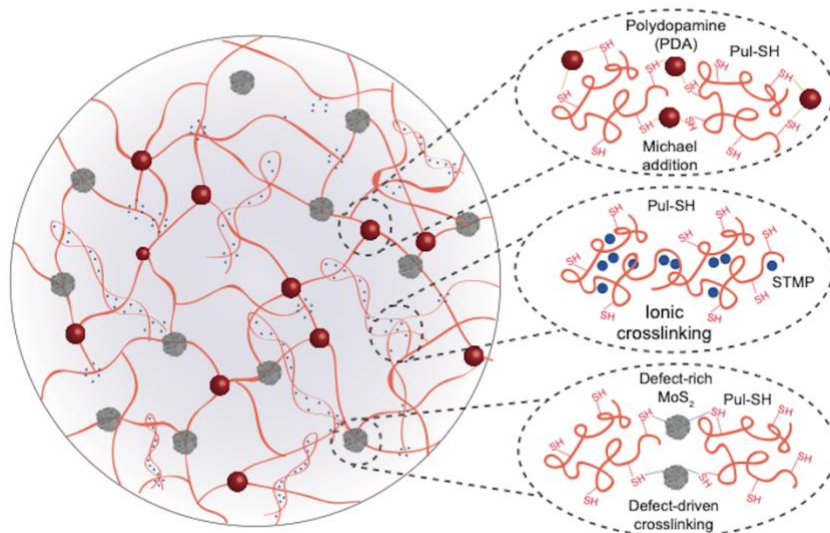


Figure 2.2 Schematic of the triple-network hydrogel architecture designed by Roy et al., integrating defect-rich MoS₂, PDA nanoparticles, and thiolated pullulan (Pul-SH) [6].

2.3 Hydrogel-Based Sensing Platforms

2.3.1 Multi-Component Conductive Hydrogel Composites (PDA-PAM Systems)

Polyacrylamide (PAM) hydrogels augmented with polydopamine (PDA) represent a biomimetic design merging covalent and non-covalent bonding within one matrix. PDA, a polymerized catecholamine inspired by mussel chemistry, can covalently integrate into the PAM network (e.g. via Michael addition or Schiff-base reactions of oxidized quinones with polymer amines) while also forming non-covalent interactions [5]. The resulting single-network hydrogel is dual-crosslinked by permanent covalent bonds (from a crosslinker such as BIS) and a multitude of dynamic bonds from PDA [5]. This dual bonding nature endows the composite with superb stretchability and high toughness. Particularly, the PDA–PAM hydrogels can impart formidable adhesion to substrate surfaces using reversible bonds as well as irreversible covalent links under oxidative conditions. This combination mimics the mussel’s strategy of using catechols for both interfacial binding and cohesive crosslinking, resulting in a hydrogel that is extensible, tough, self-healing, and strongly adhesive even in wet conditions. In short, PDA-PAM hydrogels leverage a mussel-inspired dual bonding mechanism to achieve a resilient yet adhesive network, providing an ideal basis for biointerfacial electrodes.

Marine mussels, *Mytilus* spp., owe their adhesive prowess to specialized mussel foot proteins rich in 3,4-dihydroxy-L-phenylalanine (DOPA, a catecholic amino acid). These proteins are secreted from the mussel foot onto surfaces in the form of a phase-separated fluid or coacervate as shown in Figure 2.3. The coacervate deposition is central to underwater adhesion. Mfp-3 and Mfp-5, containing 10–30 mol% DOPA, form a condensed, water-immiscible adhesive that spreads on the target and displaces interfacial water [14]. When exposed to oxygen or higher pH, a portion of DOPA oxidizes to quinone, forming covalent crosslinks that solidify the adhesive plaque. PDA

reproduces this natural chemistry by offering catechol and amine groups that mimic Mfp-3 and Mfp-5 functionality.

Mytilus californianus Mussel Adhesive Plaque

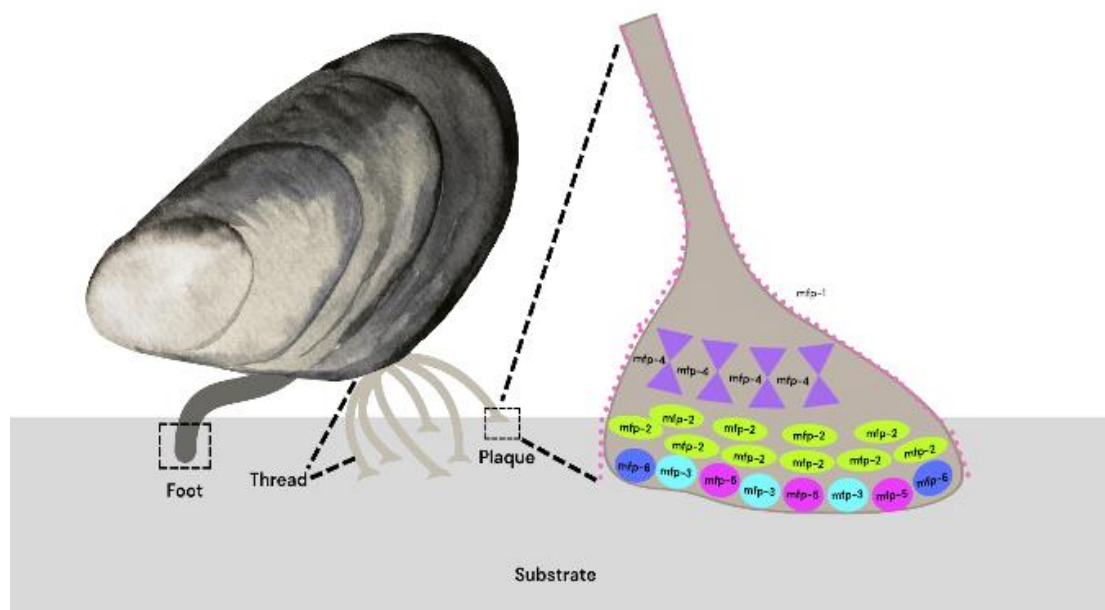


Figure 2.3. – Schematic of mussel foot adhesion mechanism and catechol-rich protein secretion in an underwater environment (created with BioRender.com). The mussel foot delivers Mfp proteins that coacervate at the interface, allowing DOPA residues to bind the substrate. Subsequent oxidation of DOPA to quinone and interactions with metal ions lead to crosslinked plaque formation.

The conductivity of hydrogel-based electrodes can be introduced by incorporating conductive fillers that exploit PDA's surface chemistry for uniform dispersion. Prior approaches include mixing in carbon-based nanomaterials such as graphene or carbon nanotubes (CNTs) in the PDA–PAM matrix [15]. As well as adding intrinsically conductive polymers like polypyrrole

(PPy) or polyaniline (PANI) [16]. Each strategy has merits and limitations. For instance, percolating networks of graphene or CNT can endow hydrogels with electronic conductivity but achieving a uniform dispersion and strong interfacial bonding is difficult. Agglomeration or slip at the hydrogel filler interface can weaken mechanical properties. Conductive polymers (PPy, PANI) can be polymerized within hydrogels to form a semi-interpenetrating network that conducts electrons. However, these rigid conjugated polymer networks often introduce brittleness under repeated deformation [16]. Another approach has been to use ionic conductors, by loading hydrogels with high-concentration electrolytes or ionic liquids. Such ionically conductive hydrogels leverage mobile ions to carry charge and can maintain conductivity even at high strains [17]. Nonetheless, purely ionic conductors can suffer from dehydration over time and generally have higher resistivity than metallic fillers. Hybrid strategies have surfaced to synergistically combine these mechanisms. For example, Ren et al. and Chen et al. confirmed that encapsulating Fe₃O₄ nanoparticles within a polydopamine shell prevents nanoparticle aggregation and enhances electrochemical responsiveness, all without degrading the hydrogels soft compliance [18] [19]. These findings collectively demonstrate that integrating ionic dopants, high-aspect-ratio conductors, and magnetic nanoparticles can link both ionic and electronic conduction domains in one network [16; 19; 20; 21].

Guided by these advances, the present work expands upon the conventional PDA-PAM framework by incorporating a lithium salt (LiCl), graphene nanoplatelets (xGNPs), and Fe₃O₄ nanoparticles. The chosen additives each fulfill a specific role in the Fe₃O₄/LiCl/xGNP-doped PDA-PAM hydrogel. LiCl is added as a dissociated ionic salt to confer ionic conductivity and improve the hydrogel's environmental stability. LiCl provides a high concentration of charge carriers (Li⁺, Cl⁻) that can rapidly migrate under an electric field, thus lowering the impedance of

the hydrogel [17]. Next, exfoliated graphene nanoplatelets (xGNP) are included to form a percolating electronic conduction network. xGNP has excellent electrical conductivity, when dispersed within the gel, these nanoplatelets connect to form conductive pathways that electrons can travel along. This boosts the composite's conductivity by orders of magnitude. Graphene reinforces the hydrogel mechanically due to its high strength and large surface area for polymer-filler interactions. The Fe_3O_4 nanoparticles serve multiple synergistic functions. Fe_3O_4 itself is a magnetic, semi-conductive nanoparticle that can contribute to charge transport and can be remotely activated by magnetic fields. Integration into the hydrogel is improved by coating Fe_3O_4 with PDA. The PDA shell provides adhesive functional groups that graft into the polymer network preventing nanoparticle aggregation. In this work's system, the Fe_3O_4 NPs become an integral crosslinking point and endow the hydrogel with stimulus-responsive behavior. The resultant hydrogel composite embodies the principles of bio-inspired interface engineering. Chapter 3 will detail the synthesis for fabricating this $\text{Fe}_3\text{O}_4/\text{LiCl}/\text{xGNP}$ -doped PDA-PAM hydrogel.

2.3.2 Modulus Matching and Electrical Bio Integration

Flexible bioelectronic implants and sensors must closely match the mechanical softness of living tissue to achieve unified integration. Most “flexible” electronic materials still exhibit moduli on the order of tens of MPa, creating a stark stiffness mismatch at the biotic–abiotic interface [6]. Hydrogels and other soft polymer networks offer a solution, as they can be engineered with elastic moduli in the tens of kPa comparable to natural tissues like human skin (~130 kPa) or muscle (~10 kPa) [12]. This tissue-mimicking compliance is imperative for bio-integration: a softer device minimizes interfacial stress and movement artifacts, allowing more stable, intimate contact between the device and moving tissues. Indeed, hydrogel-based electronic skins have tissue-like

softness and stretchability that mirror human skin, dramatically reducing interfacial resistance and motion-induced signal noise.

Modulus matching can be achieved by tuning the polymer network architecture and incorporating soft, bio-inspired ingredients. For example, a triple-crosslinked nanocomposite hydrogel (pullulan with PDA* and MoS₂ crosslinkers) was formulated to replicate skin's elasticity, yielding a Young's modulus of ≈ 42 kPa, within the range of soft physiological tissue. By adjusting crosslink density and nanoparticle content, the hydrogel's stiffness was modulated from ~ 16 kPa (single crosslink) up to ~ 60 kPa (triple crosslink), without compromising stretchability [6]. In another design, incorporating polydopamine (PDA) nanoparticles into a polymer network not only introduced bio-inspired catechol adhesion but also slightly softened the matrix. A PDA-doped hydrogel electrode exhibited ultralow Young's moduli of ~ 3.5 – 6.9 kPa (with similarly low storage moduli) [1]. This modulus is orders of magnitude lower than that of conventional metallic or polymeric electrodes and is much closer to the softness of skin, enabling the hydrogel to conform perfectly to irregular, dynamic tissue surfaces. Such tissue-like compliance (even allowing the hydrogel to imprint a fingerprint pattern) is vital. It virtually eliminates biomechanical mismatch at the interface, keeping the device comfortably coupled to moving skin without irritation or delamination.

Achieving electrical bio-integration is equally important, requiring the material to conduct signals effectively while remaining soft. A common approach is to introduce conductive fillers or dopants into the soft matrix to create percolating electrical pathways without significantly stiffening it [2]. For instance, Gong et al. developed a PVA/P(AA-co-AM) hydrogel with PDA-decorated carbon nanotubes (PDA@CNTs) uniformly dispersed throughout the network. The CNT nano-network endowed the hydrogel with an electrical conductivity on the order of 10^0 S/m

(approximately 3.8 S/m in this case), while the bulk of the material remained a high-water-content, soft gel [2]. Similarly, multi-network hydrogels loaded with mobile ions or intrinsically conductive polymers can reach conductivities of tens of Siemens per meter, all the while maintaining extracellular-matrix-like softness. The result is a bioelectronic interface that is both mechanically and electrically matched to the body. The soft, ionic-conducting hydrogel skin provides low interfacial impedance and intimate contact, which dramatically improves signal fidelity. For example, a PDA-nanoparticle-infused hydrogel electrode showed an impedance below 50 Ω at 100 Hz (in the EEG frequency range), far lower than traditional gel or dry electrodes [1]. By matching the give of living tissue and holding steady electrical contact, these materials stay comfortable to wear and consistent in performance.

2.4 Mechanical Testing Approaches

Although commercial tensile systems are highly accurate, the cost, size, and inability to be adjusted remain as prevalent issues [15]. Gels exhibit very low elastic moduli and can sustain large deformations. Accurately capturing such low stresses and high strains demands exceptional force sensitivity and displacement resolution. Many universal testers were originally designed for stiffer materials and lack the needed low-range accuracy for soft samples [17]. Another challenge is the gripping control for these types of samples. Hydrogels tend to slip or tear if clamped with conventional hard grips. Special grips are required to avoid slippage and failure of the specimen when testing soft tissues [9]. High end biomaterial testing platforms do exist such as CellScale's UniVert and similar systems however these commercial solutions are expensive. On the order of \$30-40k for an entry level setup [9]. Given the limitations above, researchers have increasingly turned to custom-built tensile platforms to test soft materials.

CHAPTER 3: MATERIALS AND METHODOLOGY

3.1 Reagents and Experimental Materials

Analytical grade chemicals including dopamine hydrochloride (DA), acrylamide (AM), ammonium persulfate (APS), N, N'-methylenebisacrylamide (BIS), sodium hydroxide (NaOH), and tetramethylethylenediamine (TEMED) were procured for this research. Additional materials incorporated for the composite hydrogel synthesis included lithium chloride (LiCl), graphene nanoplatelets (xGNP), and iron (III) chloride hexahydrate and ($\text{FeCl}_3 \cdot 6\text{H}_2\text{O}$) and sodium acetate (NaOAc), used for the solvothermal synthesis of Fe_3O_4 nanoparticles. No further purification was performed on any of the reagents prior to use. All aqueous solutions and experimental preparations were made using deionized water exclusively.

3.2 Synthesis of Hydrogels: PDA-PAM and Fe_3O_4 /xGNP/LiCl (2.8 wt%)

3.2.1 Synthesis of PDA-PAM Hydrogel

A polydopamine (PDA) polyacrylamide hydrogel was prepared using free-radical polymerization. The experiment begins by dissolving 0.0065 g of polydopamine powder into 7 mL of 1 M NaOH (pH 11) in a beaker. This creates a highly basic medium (pH 11) that triggers oxidation of dopamine monomers into polydopamine. The dopamine solution is stirred gently for at least an hour at room temperature. During which the color gradually changes, typically darkening to a brown/black hue.

While the PDA is polymerizing, we measure out acrylamide and cross-linker. To avoid premature reactions, this step is performed in an ice bath (0-5 °C). Into the preformed PDA solution, we slowly add 2.6 g of acrylamide (AM), 0.25 g of ammonium persulfate (APS), and 0.003 g of N, N'-methylenebisacrylamide (BIS). The solution is stirred continuously as each solid dissolves. The calculated concentrations after mixing and before adding TEMED are

approximately: [AM] \approx 4.57 M (since 2.6 g in 0.008 L), [BIS] \approx 2.43 mM, [APS] \approx 0.137 M. The mixture is stirred in the ice bath for about 10 minutes to ensure homogeneity. While the solution is still in the ice bath, we then add 20 μ l of TEMED into the stirred mixture. Once TEMED is mixed in, the polymerization reaction begins rapidly. The reactive mixture is poured into molds: either a 3D-printed rectangular mold or a cylindrical mold, depending on the intended characterization tests. Gelation typically completes within 15 – 30 minutes, however we let the gel set for at least 1 hour. The formulation corresponds to a dopamine loading of 2.5 wt.% relative to acrylamide.

3.2.2 Addition of Fe₃O₄, xGNP, and LiCl Dopants

To systematically evaluate the effects of different conductive, magnetic, and ionic dopants, a total of six doped PDA–PAM hydrogel formulations were prepared using varied combinations of Fe₃O₄ nanoparticles, graphene nanoplatelets (xGNP), and lithium chloride (LiCl).

Each hydrogel is identified by a short label used consistently throughout this thesis for figures, tables, and discussion. Full compositions and scientific names are summarized in Table 3.1. All formulations use a constant PDA loading of 2.5 wt% relative to acrylamide unless otherwise specified. Unless otherwise stated, PDA–PAM hydrogel is designated as the control group. Fe₃O₄/xGNP/LiCl (2.8 wt%) @ PDA–PAM serves as the experimental group in Sections 3.4.3, 3.4.4, and 3.7, and in corresponding Chapter 4 results.

Short Label	Full Name	Fe ₃ O ₄ (g)	xGNP (g)	LiCl (g)
Fe ₃ O ₄	Fe ₃ O ₄ nanoparticles (NPs)	0.013	-	-
Fe ₃ O ₄ /xGNP	Fe ₃ O ₄ + xGNP	-	0.052	-
Fe ₃ O ₄ /LiCl 2.8%	Fe ₃ O ₄ + LiCl (2.8 wt %)	0.013	-	0.3
xGNP/LiCl 2.8%	xGNP + LiCl (2.8 wt %)	-	0.052	0.3
LiCl 2.8%	Fe ₃ O ₄ + xGNP + LiCl (2.8 wt %)	0.013	0.052	0.3
LiCl 4.6%	Fe ₃ O ₄ + xGNP + LiCl (4.6 wt %)	0.013	0.052	0.5

Table 3.1: Composition summary of PDA–PAM-based hydrogel variants. Formulations are labeled by short identifiers used in all figures and discussion. All quantities listed are per batch (~7 mL final volume).

Among all tested variants, the Fe₃O₄/xGNP/LiCl (2.8 wt%) PDA–PAM hydrogel demonstrated the most favorable balance of ionic conductivity, adhesion, and mechanical compliance. This formulation was therefore selected as the reference “experimental group” for downstream comparisons. The synthesis involved the following protocol: The Fe₃O₄ and xGNP powders were first wetted with a few drops of ethanol to improve dispersibility and then dispersed in 2.00 mL of 1 M NaOH (pH 11) using bath sonication for 20 min while maintaining the temperature below 30 °C. Any remaining aggregates were broken by short, intermittent probe-sonication bursts on ice. Separately, dopamine hydrochloride (0.0065 g) was dissolved in 5.00 mL of 1 M NaOH (pH 11) under gentle stirring to initiate self-oxidation of dopamine into PDA. Immediately following dissolution, the Fe₃O₄/xGNP nanoparticle stock was introduced into the dopamine solution to allow polymerization and coating to occur simultaneously. The mixture was

stirred at room temperature for 90 min as the dopamine polymerized and deposited uniformly onto the nanoparticle surfaces, producing a stable PDA-coated $\text{Fe}_3\text{O}_4/\text{xGNP}$ dispersion with a dark brown–black coloration indicative of successful coating.

After polymerization, LiCl (0.300 g) was added to the PDA–nanoparticle dispersion and stirred until fully dissolved to introduce mobile ions. The mixture was then cooled in an ice bath (0–5 °C) to slow polymerization and ensure uniform mixing. Acrylamide (2.600 g) and BIS (0.003g) were added sequentially and stirred until fully dissolved, forming a homogeneous monomer solution. Polymerization was initiated by adding ammonium persulfate (0.25 g) followed by 20 μL of TEMED to catalyze free-radical generation. The solution was briefly vortexed to maintain even nanoparticle suspension and rapidly cast into pre-prepared molds within 60–90 seconds before gelation. Curing was completed at room temperature over 12 hours, yielding a dark, uniform $\text{Fe}_3\text{O}_4/\text{LiCl}/\text{xGNP}$ -doped PDA–PAM hydrogel with well-dispersed fillers.

The cured gels were demolded and rinsed three times in fresh deionized water (15 min per rinse, total 30–45 min) to remove unreacted monomers, free PDA, and excess salts while avoiding prolonged leaching of LiCl. After the final rinse, the hydrogel surfaces were gently blotted with KIM wipes and stored hydrated until testing. Figure 3.1 illustrates the schematic synthesis process for the $\text{Fe}_3\text{O}_4/\text{LiCl}/\text{xGNP}$ -doped PDA–PAM hydrogel, showing nanoparticle dispersion, PDA coating, LiCl doping, and polymerization into the final conductive network.

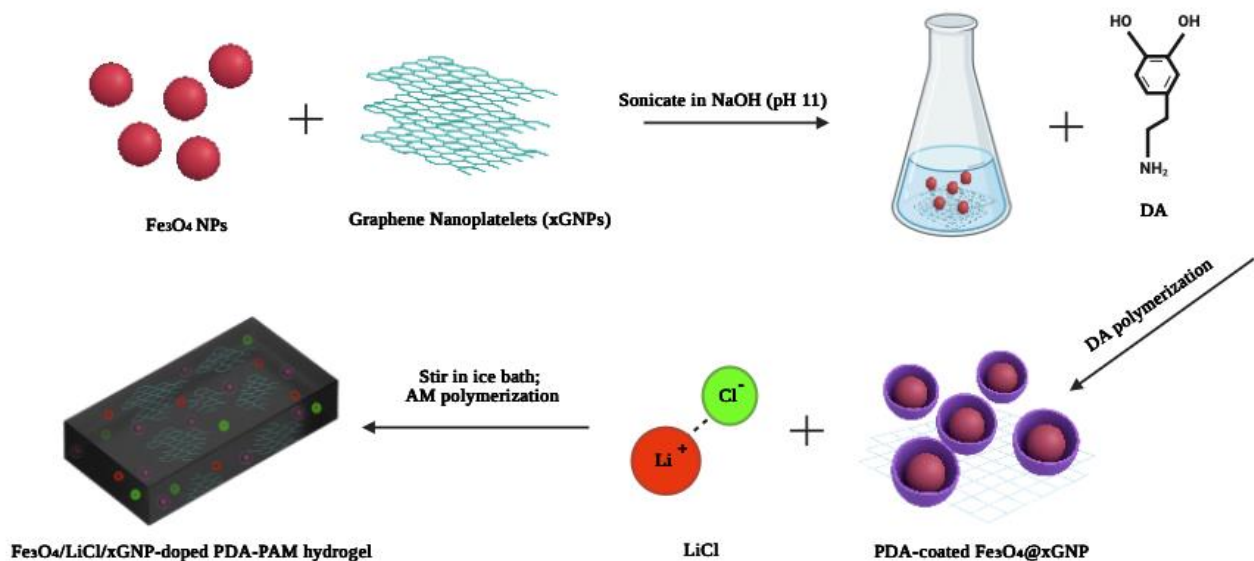


Figure 3.1. Schematic of the synthesis route for the $Fe_3O_4/LiCl/xGNP$ -doped PDA–PAM composite hydrogel (created with BioRender.com).

3.3 Structural Characterization via SEM

The internal morphology of the PAM, PDA–PAM hydrogels (2.5 wt.% DA/AM), and $Fe_3O_4/xGNP/LiCl$ (wt. 2.8%) doped PDA-PAM hydrogel were examined using scanning electron microscopy (TESCAN VEGA) operated at 15 keV and 300 pA. Prior to imaging, the hydrogels were freeze-dried and subsequently sectioned to expose the cross-sectional structure for analysis.

3.4 Self-Healing

The self-healing capability of the PDA–PAM hydrogel doped with Fe_3O_4 nanoparticles, LiCl, and xGNP (graphene nanoplatelets) was determined by means of a simple cut-and-repair experiment. A cylindrical gel sample (length ~16 cm, diameter ~13 cm) was cleanly severed into two pieces using a razor blade. Immediately after cutting, the fresh surfaces were placed back in contact, aligning the original shape, and the assembly was left undisturbed to heal under ambient

conditions (≈ 22 °C) for 12 hours. No external stimulus (such as heat, pH change, or chemical healing agent) was applied. The self-recovery relied purely on the intrinsic dynamic bonds within the hydrogel. After the 12 h healing period, the sample was carefully picked up and manually stretched by hand to assess the strength of the healed interface.

3.5 Mechanical Testing: Tensile, Compression, and Adhesion

The tensile testing device was constructed around a rigid aluminum T-slot frame that supports a vertical motion stage. Linear translation is provided by a G1610 ballscrew with a 10 mm lead and 800 mm stroke, coupled to a NEMA 23 stepper motor rated at 1200 rpm. The drive is powered through a 24 V DC supply and controlled by a DM542T digital driver, with step and direction pulses generated from a LabJack T7-Pro. A uniaxial load cell with a 22 N range is mounted in line with the moving stage, with excitation, ground, and signal lines interfaced through the LabJack to allow force and displacement to be acquired on the same system. An overview of the assembled apparatus is shown in Figure 3.2.



Figure 3.2 Tensile device apparatus.

System operation follows a two-stage process. A Lua script executed through Kipling configures the motor registers prior to each run, after which a LabVIEW virtual instrument provides control during testing. The VI allows the operator to set motion direction and speed, converts motor steps to displacement using the screw lead, and calculates engineering strain from the sample gauge length. Force readings are scaled to stress values, and stress–strain data are displayed and logged in real time. Further construction details, wiring tables, and software interfaces are provided in Appendix A.

3.5.1 Tensile

Uniaxial tensile testing is used to measure the following mechanical properties: Young's modulus, yield strength, and ultimate tensile strength (UTS). [15]. In a tensile test, a hydrogel sample is pulled until failure to produce a stress-strain curve, from Young's modulus (slope in the initial linear region), UTS (peak stress), and toughness (energy absorption, equal to area under the curve) are procured, as shown in the following Figure 3.3.

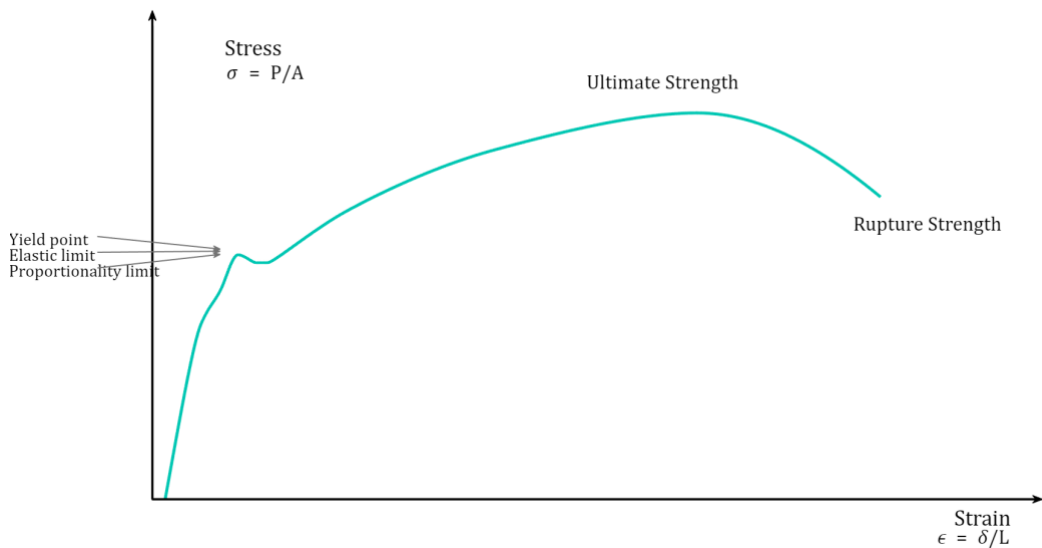


Figure 3.3 Stress-strain relationship demonstrating characteristic properties from tensile tests.

For a sample of initial cross-sectional area A_c and length L_0 , the engineering stress (σ) and strain (ϵ) are defined as:

$$\sigma = \frac{F}{A_c}, \quad \epsilon = \frac{\Delta L}{L_0}$$

where F is the applied force and ΔL is the extension. From the stress-strain data, one can determine the Young's modulus E , and is calculated like so:

$$E = \frac{\Delta\sigma}{\Delta\varepsilon}$$

3.5.2 Compression

Besides tension, hydrogels are characterized in compression to evaluate their behavior under squeezing loads. In a uniaxial compression test, a cylindrical gel is pressed between plates while recording stress-strain [6]. This yields the compressive modulus which is analogous to Young's modulus and compressive strength at failure or at a set strain. Due to their high-water content, most hydrogels are nearly incompressible and can sustain very large high-water content since the water simply redistributes under pressure. Compressive stress-strain curves of soft gels typically show an initial low modulus that stiffens dramatically at higher strain.

3.5.3 Adhesion

The adhesive capability of both hydrogel formulations, the control group and the experimental group, was qualitatively assessed on five representative substrates with distinct textures: plastic, glass, metal, cardboard, and foam. These materials were selected to encompass a range of surface energies and textures. Each substrate was cleaned and dried prior to testing to ensure consistent surface conditions. A simple lift-and-hold method was employed to visually demonstrate the hydrogel's adhesive strength. A strip of freshly prepared gel (~4 mm thick) was partially adhered to the substrate while the opposite end was attached to a gloved index finger. The finger was lifted vertically to suspend the substrate against gravity using only the hydrogel's cohesive and adhesive forces.

3.6 Electrical Testing

The electrical performance of the PDA–PAM conductive hydrogel (2.5 wt% DA/AM) was evaluated using a Bio-Logic SP-300 electrochemical workstation in a two-electrode configuration. Four replicate samples were prepared under identical conditions to ensure reproducibility. Each sample was cast into a rectangular mold with copper tape affixed at opposing ends prior to gelation. This configuration defined an effective conduction path length of 12 mm and a uniform cross-sectional area for current transport. The instrument's alligator clips were attached directly to the exposed copper tape, with the working electrode lead connected at one end and the counter/reference leads connected at the opposite ending.

3.6.2 Conductivity

Potentiostat electrochemical impedance spectroscopy (PEIS) was employed first to determine bulk conductivity. The applied perturbation amplitude was maintained 5-10 mV with logarithmic frequency spacing across the range of 10^6 and 10^2 Hz. At each frequency point, data acquisition involved averaging over ten cycles following an initial stabilization period. The real-axis intercept at high frequency of the Nyquist plot was taken as the bulk resistance, R_b . Conductivity was calculated according to:

$$\sigma = \frac{L}{R_b \times A}$$

where $L = 3.5$ cm is the electrode spacing, $A = 0.48$ cm² is the cross-sectional area, and R_b is the measured bulk resistance. The cross-sectional dimensions (width x height) = 1.2 cm, $T = 0.4$ cm. Volume = $3.5 \times 1.2 \times 0.4 = 1.68$ cm³. Values from all samples were averaged and reported as mean \pm standard deviation.

3.6.3 Chronoamperometry

Chronoamperometry (CA) was employed to further examine the time-dependent charge transport under steady bias. The gels were polarized at a constant potential of 0.01 V vs E_{oc} for duration of 600 s. Current was recorded at 0.1 s intervals with an E range of -2.5 to +2.5 V, and I range of 1 mA, and bandwidth set to 8. The data was interpreted in the context of Cottrell's relationship,

$$i = \frac{nFAC_0\sqrt{D}}{\sqrt{\pi t}}$$

where $i(t)$ is the current at time t , n is the number of electrons transferred, F is Faraday's constant, A is the electrode area, C_0 is the bulk concentration of electroactive species, and D is the diffusion coefficient.

3.6.4 Cyclic Voltammetry

Cyclic voltammetry was conducted to assess the redox stability of the hydrogel electrodes. The potential was swept from -0.5 V to +0.5 V at a scan rate of 0.05 V s⁻¹ for ten consecutive cycles. The voltammograms were analyzed for repeatability and the presence of anodic or cathodic peaks.

3.7 Electrophysiological Signal Acquisition (ECG Signals)

3. 7.1 Electrode Fabrication and Experimental Setup

Electrocardiogram (ECG) measurements were performed to evaluate the ability of the hydrogel electrodes to acquire physiological signals with high fidelity and stable skin contact. The test electrodes were prepared by modifying standard pre-gelled Ag/AgCl ECG electrode housings (snap connector type). The factory gel was carefully removed from each electrode's cavity, leaving

the Ag/AgCl sensing element and adhesive foam backing. The cavity was then filled with freshly synthesized hydrogel, using one of two formulations: the control group or experimental group. The hydrogels were allowed to polymerize and dry in situ within the electrode housings for several hours and the original adhesive foam layer was re-applied to seal the cavity. The two hydrogel types were visually distinguishable by tint: the PDA–PAM control gel appeared translucent reddish-brown, whereas the Fe₃O₄/xGNP/LiCl-loaded gel was an opaque black. This distinction is displayed in Figure 3.4, which shows the completed hydrogel-filled electrodes side by side.

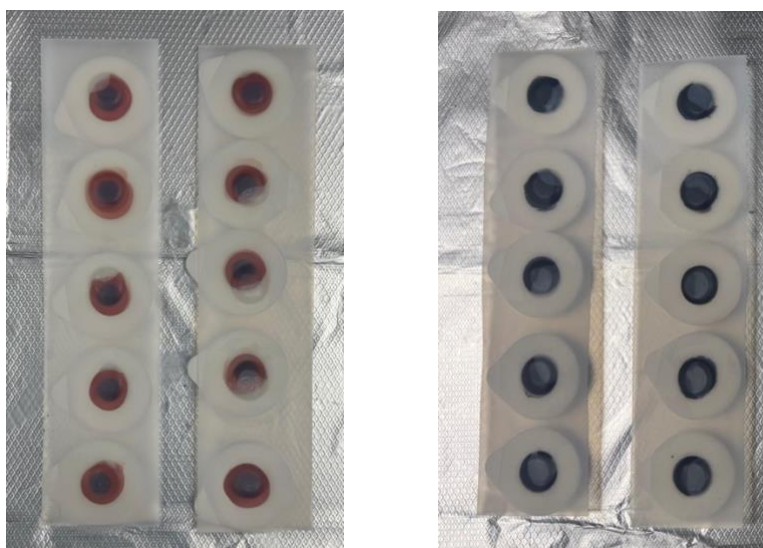


Figure 3.4 The control electrodes (left strip) contain the red-tinted PDA–PAM hydrogel, and the optimal electrodes (right strip) contain the black composite hydrogel. Each unit retains the white foam backing and Ag/AgCl snap, with the hydrogel occupying the central cavity.

All ECG recordings were performed on a healthy adult male following informed consent. Prior to electrode application, the subject's chest and limb areas were cleaned with 70% isopropanol and allowed to dry fully to reduce skin impedance and ensure secure electrode adhesion. Electrodes were then positioned according to the standard 12-lead resting ECG configuration (Figure 3.5), which includes 10 physical electrodes: 4 limb electrodes (RA, LA, RL, LL) and 6 precordial electrodes (V1–V6) distributed across the chest.

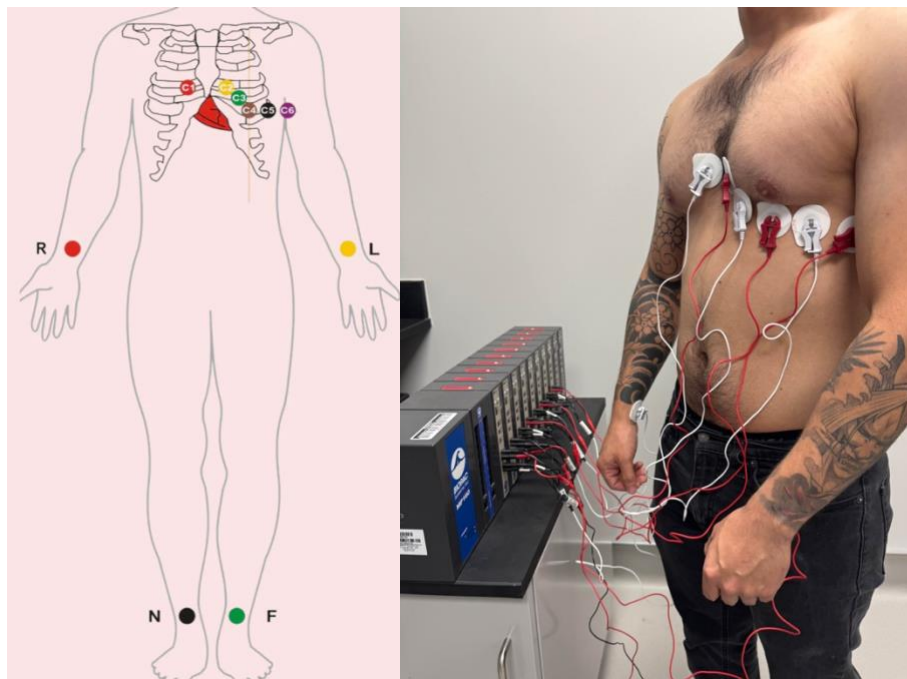


Figure 3.5 (Left) Schematic of the standard 12-lead ECG electrode configuration, including four limb leads (RA, LA, RL, LL) and six precordial chest leads (V1–V6). (Right) Test subject instrumented with modified hydrogel-filled electrodes connected to the BIOPAC MP160 system during ECG acquisition.

The subject was instrumented once per group, and each group was tested across three physical states in the following order:

1. Resting state
2. Squat activity (10 continuous standing squats)
3. Push-up activity (10 full push-ups)

A short rest was given between each phase to stabilize heart rate. The control group electrodes were always tested first across all three states, followed by complete removal and reapplication of fresh electrodes from the experimental group in the same positions and test sequence. This approach minimized positional variance and allowed for within-subject comparisons of performance under identical conditions. ECG signals were acquired using a BIOPAC MP160 system equipped with a standard ECG amplifier module and AcqKnowledge software.

3.7.2 ECG Signal Quality Criteria and Metrics

To evaluate and compare the performance of the hydrogel electrodes during ECG acquisition, several signal quality criteria were defined. These were based on waveform morphology, noise characteristics, and quantitative metrics. An ideal ECG signal should have a steady baseline, well defined P-QRS-T complexes, minimal noise, and consistent cardiac cycles across leads. The main structural elements of an ECG signal are mapped in Figure 3.6, which depicts the P wave, QRS complex, and T wave.

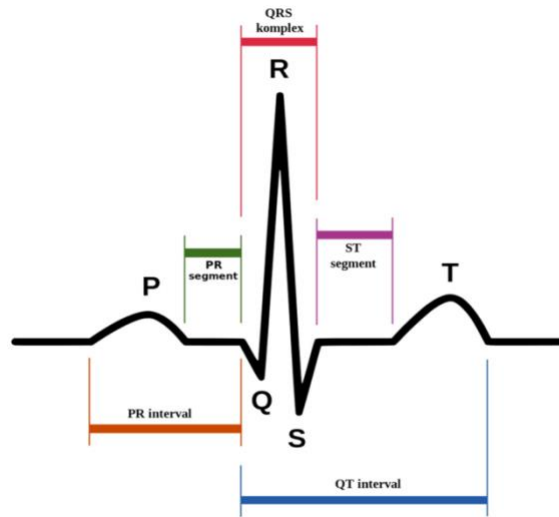


Figure 3.6 Schematic of a typical ECG signal with labeled P-QRS-T components.

The PQRST sequence provides the core structure of a typical cardiac cycle and serves as the reference for all signal quality checks. The P wave marks atrial depolarization and should appear smooth and consistent. The PR interval represents the conduction delay through the AV node, while the QRS complex captures rapid ventricular depolarization. A narrow, steep QRS complex indicates good resolution of fast voltage transitions. The ST segment and T wave reflect ventricular repolarization, with the T wave expected to follow a predictable morphology. The QT interval spans the duration of ventricular activity. Any deviation in these features such as missing P waves, distorted QRS complexes, or elevated noise during the T wave are treated as a sign of signal degradation.

Quantitative assessment focused on signal-to-noise ratio (SNR), baseline drift, R-wave sharpness, and inter-lead variation. SNR was calculated using the following expression:

$$SNR (dB) = 10 * \log_{10}\left(\frac{P_{signal}}{P_{noise}}\right)$$

where P_{signal} was measured within the 0.5–40 Hz band to reflect true cardiac activity, while P_{noise} accounted for unwanted interference from higher frequencies and baseline drift. A higher SNR indicates stronger signal clarity and less contamination. Baseline wander, typically from motion or poor adhesion, appeared as slow drift and was evaluated across 10-second segments. Motion artifacts were identified by irregular spikes or waveform distortion unrelated to normal ECG shape. Consistency across beats was assessed by examining R-wave alignment and T-wave uniformity over time. Differences in amplitude or baseline levels between leads indicated potential instability in electrode contact. These factors combined formed the basis for evaluating hydrogel performance under both resting and dynamic conditions.

CHAPTER 4: RESULTS AND DISCUSSION

4.1 Synthesis of Hydrogels: PDA-PAM and Fe₃O₄/xGNP/LiCl (2.8 wt%) Results

4.1.1 PDA-PAM Hydrogel Synthesis Results

For the synthesis of the PDA-PAM hydrogel, the first step is an alkali-induced polymerization of dopamine (DA). In basic conditions, DA monomers are oxidized and self-polymerize into polydopamine (PDA). This process is accompanied by a distinct color change of the solution from colorless to a dark brown hue, as shown in Figure 4.1.

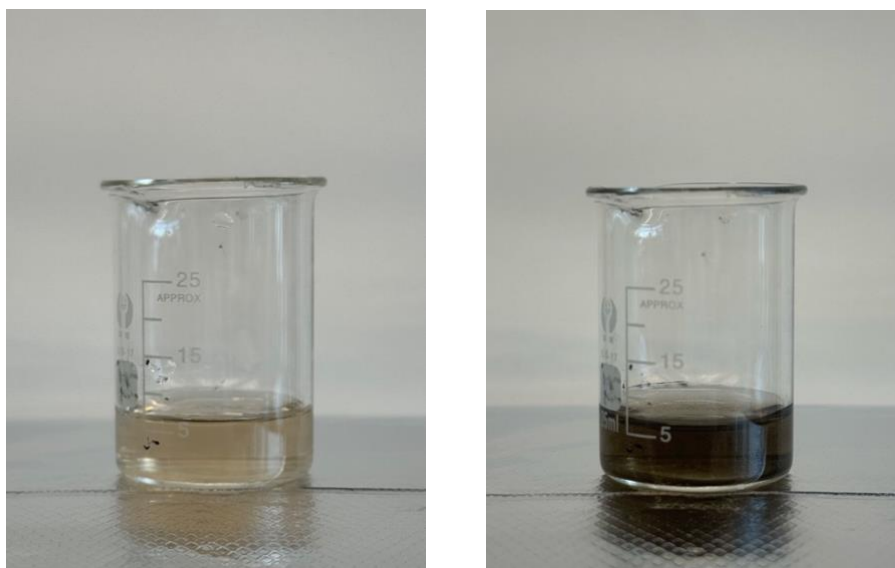


Figure 4.1 Visual confirmation of dopamine polymerization. Solution before (left) and after one hour of oxidation (right).

Once PDA formation is initiated, the PDA chains become integrated into the growing poly(acrylamide) network. In the subsequent free radical polymerization step, acrylamide (AM) monomers (in the presence of an APS initiator and BIS crosslinker) are co-polymerized to form

the PAM hydrogel network, while PDA is simultaneously incorporated. The catechol groups on the PDA chains can interact.

4.1.2 Addition of Fe₃O₄, xGNP, and LiCl Dopants Results

The cured hydrogel samples are shown in Table 4.1. The undoped PAM control gel appears transparent and colorless, with a uniform cured shape. Incorporating dopamine into the PAM network, PDA-PAM, yields a homogeneously tinted slightly red brown but intact gel.

Short Label	Appearance
PAM	
PDA-PAM	
Fe ₃ O ₄	
Fe ₃ O ₄ /xGNP	
Fe ₃ O ₄ /LiCl 2.8%	
xGNP/LiCl 2.8%	
LiCl 2.8%	
LiCl 4.6%	

Table 4.1: Photographs of cured hydrogel samples The xGNP/LiCl 2.8% sample failed to hold shape.

Addition of Fe_3O_4 nanoparticles produces a uniformly black gel that still holds its form. In contrast, the formulation containing only graphene nanoplatelets (xGNP) and LiCl could not form a self-supporting gel. This xGNP/LiCl sample remained excessively fluid and failed to retain any defined shape. This behavior is consistent with known limitations of high-water content hydrogels, which often exhibit markedly poor mechanical strength. Since the xGNP/LiCl 2.8% could not retain shape, it was excluded from subsequent mechanical testing in Section 4.4.

The experimental hydrogel was prepared by first dispersing Fe_3O_4 and xGNP together in an alkaline NaOH solution. The solution was vigorously probe-sonicated in 5 min pulses for a total of 20 min. The dispersion was immersed in an ice bath throughout sonication to keep the temperature below $\approx 30^\circ\text{C}$. This temperature control is paramount as excessive heating can accelerate dopamine oxidation and cause uncontrolled PDA formation, whereas cooling ensures a uniform dispersion of NPs and graphene without premature polymerization. Figure 4.2 compares the dispersion before and after sonication. This step is followed by sequential addition of dopamine, LiCl, and acrylamide for polymerization.

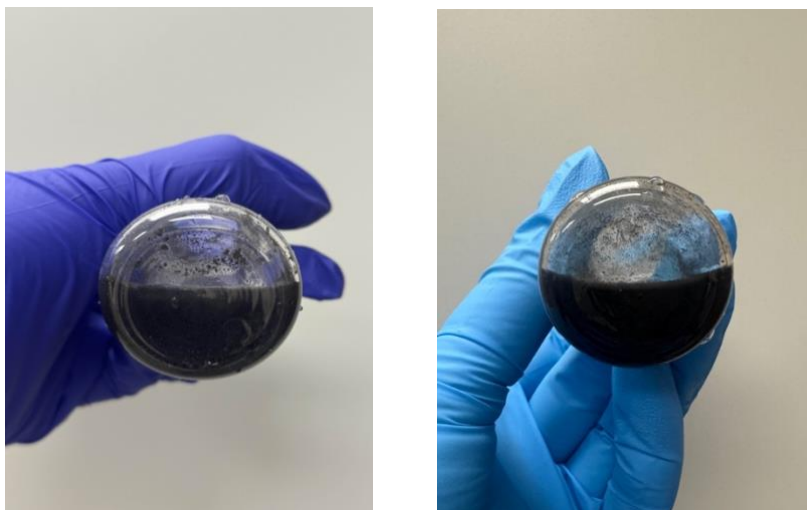


Figure 4.2: Photographs of $Fe_3O_4/xGNP$ nanoparticle suspension in aqueous solution before (left) and after (right) ultrasonic treatment.

4.2 Microstructural Characterization

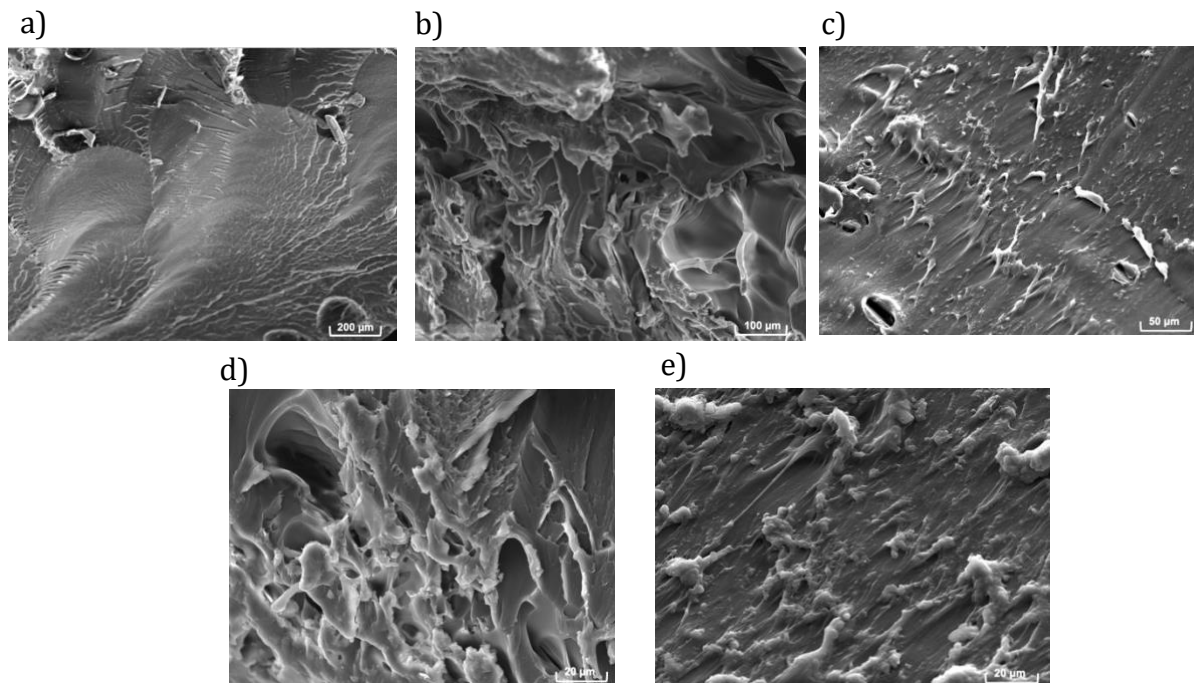


Figure 4.3 SEM images of hydrogel internal morphology: a) PAM, b) PDA-PAM, and c) $Fe_3O_4/xGNP/LiCl$ (2.8 wt%) @ PDA-PAM. Higher magnification images shown for d) PDA-PAM and e) $Fe_3O_4/xGNP/LiCl$ (2.8 wt%) @ PDA-PAM

As shown in the SEM micrographs in Figure 4.3, the pure PAM hydrogel has a relatively compact and featureless surface. There are no discernible pores or fibrils. Upon introduction of polydopamine, the internal network undergoes structural transformation. Pores and fine microfibrils span the surface. These appear as tangled, web-like fiber bundles that were absent in the PAM hydrogel. The $Fe_3O_4/xGNP/LiCl$ (2.8 wt%) composite reveals smaller pores that are

partially bridged. Fibrils span across collapsed pore walls, and the wall thickness is indicative of nanofiller embedding the structure.

Higher magnification images further confirm this trend. At 20 μm scale, the PDA–PAM hydrogel reveals open-cell voids and thin film-like walls with minimal surface texture. Whereas the $\text{Fe}_3\text{O}_4/\text{xGNP}/\text{LiCl}$ (2.8 wt%) composite displays extensive wall roughness, embedded particle-like granules, and micro-bridges spanning cracks.

4.3 Self-Healing Performance

Following the 12-hour healing the previously severed $\text{Fe}_3\text{O}_4/\text{LiCl}/\text{xGNP}$ -doped PDA–PAM hydrogel demonstrated complete restoration of form and function. Upon manual stretching, the hydrogel could be elongated to a similar extent as an uncut sample without rupturing at the former cut site. The process is demonstrated in Figure 4.4.

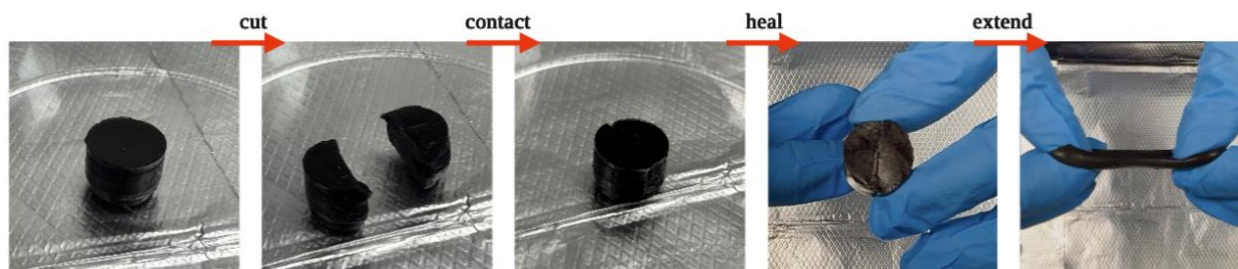


Figure 4.4 Demonstration of self-healing in the $\text{Fe}_3\text{O}_4/\text{LiCl}/\text{xGNP}$ -doped PDA–PAM composite hydrogel. The cylindrical gel was cut, rejoined, and allowed to heal for 12 hours under ambient conditions. Upon manual stretching, the hydrogel maintained interfacial integrity.

The LiCl ensured the gel remained hydrated and soft at the cut, allowing polymer chain interdiffusion across the interface during the 12 h contact period. The xGNP fillers, being dispersed throughout the network behaved as nano anchors. Graphene sheets at the surface would overlap and engage via π - π stacking with PDA, helping to bridge the gap before the bulk polymer chains rebonded. Thus, the qualitative self-healing success can be attributed to the synergistic mechanisms anticipated: hydrogen bonding, π - π stacking, and catechol-Fe coordination re-establishing across the cut.

4.4 Mechanical Properties: Tensile, Compression, and Adhesion

4.4.1 Tensile Results



Figure 4.5 Photographic comparison of hydrogels during tensile loading. (Top) Control (PDA-PAM 2.5 wt %) initial length = 1.2 cm; elongated length = 30.9 cm. (Bottom) Experimental (Fe₃O₄@PDA-PAM) initial = 1.3 cm; elongated = 23 cm.

Tensile testing revealed a difference in extensibility between the control and experimental hydrogel. The PDA-PAM stretched from 1.2 cm to 30.9 cm before failure, an elongation of approximately 2475% or more than 25x its original length. Starting at 1.3 cm, the experimental sample reached a final length of 23 cm, achieving a total elongation of approximately 1670%, or a 17.7x increase from its original size. The incorporation of the three dopants introduced additional filler polymer interactions that restricted chain mobility, thereby reducing maximum elongation.

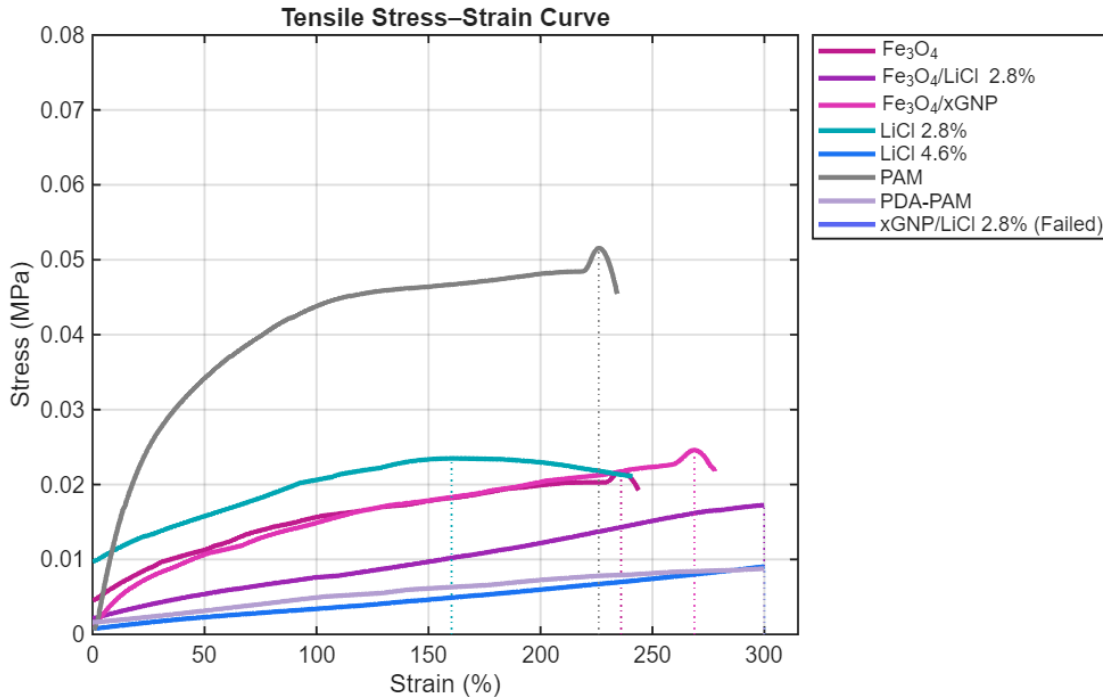


Figure 4.6 Tensile stress–strain curves of all the hydrogel formulations except for xGNP/LiCl 2.8 %. The hydrogel was overhydrated and could not retain shape for mechanical testing.

The stress strain profiles reveal that the pure PAM baseline breaks at a moderate strain with a relatively higher initial slope indicating a stiffer response. Incorporating PDA markedly softens the network and extends the failure strain. The PDA-PAM curve shows a lower initial slope and stretches well beyond the PAM sample before rupture. When conductive fillers are added, the curves steepen and shorten in extent. In particular, the PDA-PAM + Fe₃O₄ formulation portrays a much sharper stress rise and lower break strain, indicating strong stiffening and brittle behavior. The xGNP-doped hydrogel shows an even higher initial stiffness and the smallest ultimate strain, reflecting a stiffly saturated carbon network that resists deformation. On the contrary, the LiCl-doped samples are the most compliant. Both 2.8% and 4.6% LiCl curves have the gentlest rise and sustain the largest deformations. However, the salt-loaded gels reach lower peak stresses at failure. Thus, Fig. 4.6 shows that conductive fillers trade off elasticity for rigidity, whereas electrolyte doping produces a much softer and flexible hydrogel at the expense of peak strength.

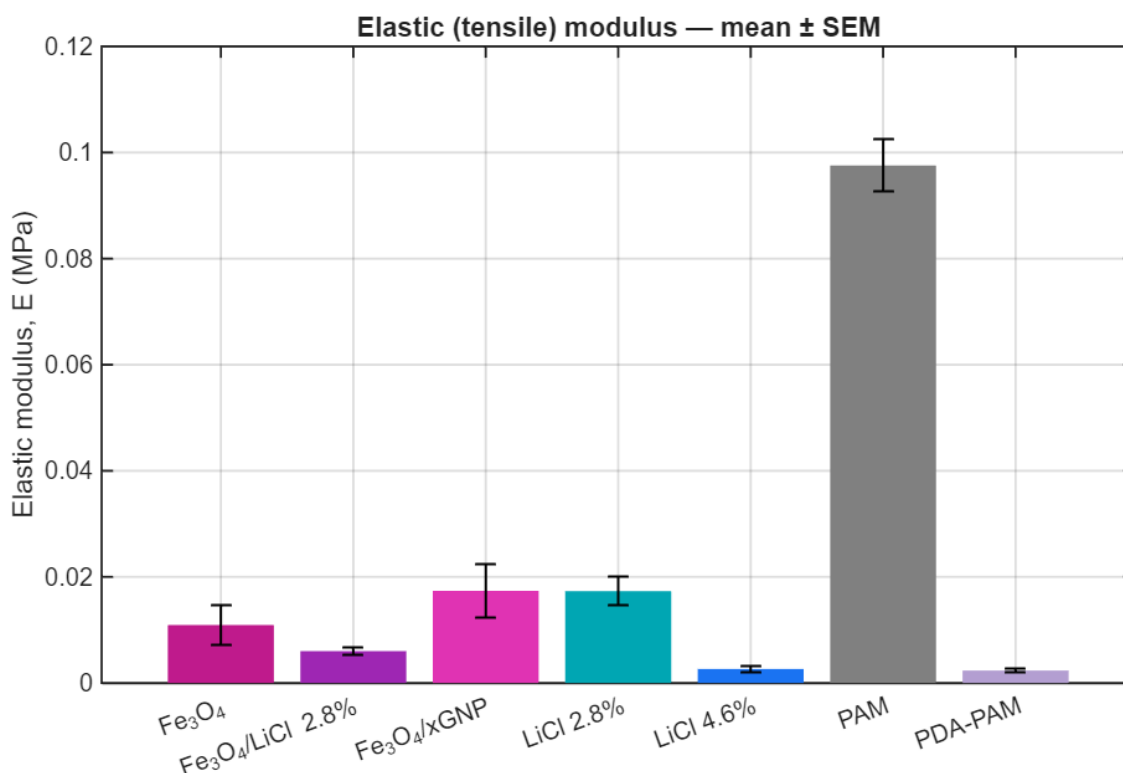


Figure 4.7 Tensile modulus of the hydrogel formulations.

The tensile modulus graph quantifies the initial stiffness of each formulation. The PDA-PAM modification lowers the modulus relative to pure PAM, whereas adding nanoparticles drives it upward. Both the Fe₃O₄ and xGNP samples exhibit significantly higher modulus values than PDA-PAM, with the xGNP group being the highest, confirming that fillers reinforce the gel and make it much stiffer. Conversely, the LiCl-doped hydrogels have the lowest moduli of all samples. The 4.6% LiCl gel is slightly softer than the 2.8% LiCl gel. In practical terms, the filler-containing gels are on the order of 2–3 \times stiffer than the base gel, while the high-salt gels approach the soft range of native skin (tens of kPa). These results show the following tradeoff: conductivity

enhancing additives such as Fe_3O_4 or xGNP substantially increase rigidity, whereas ionic electrolytes plasticize the network and produce tissue-like softness.

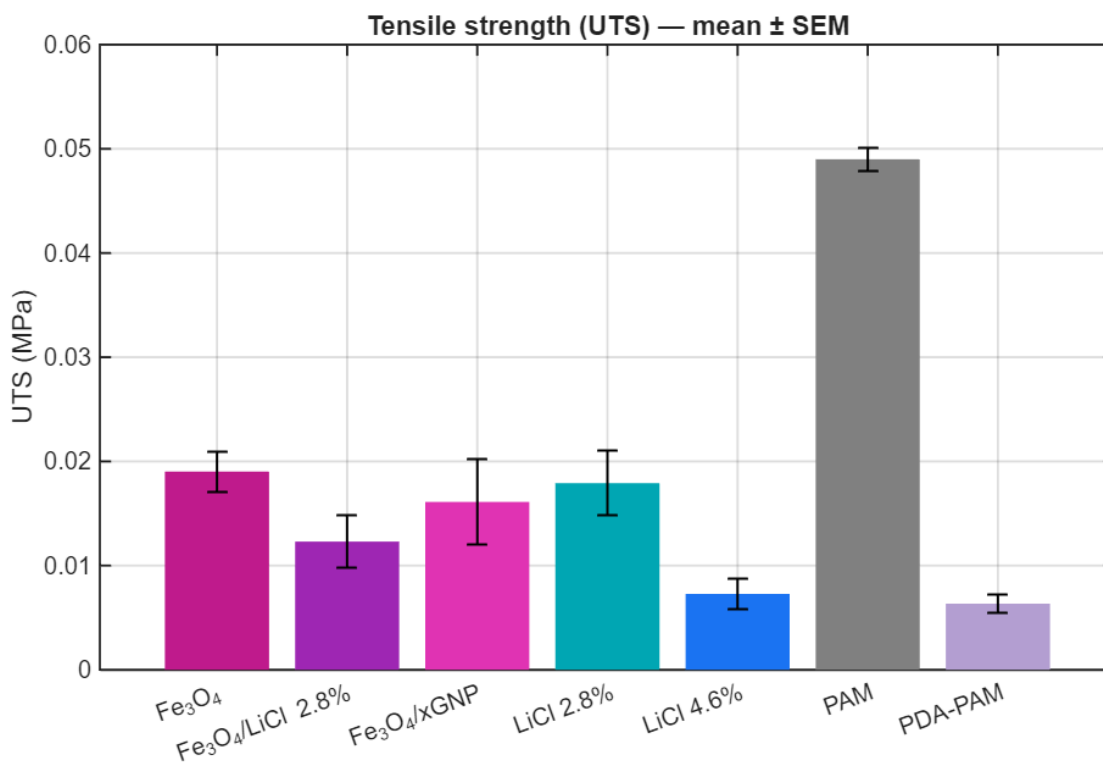


Figure 4.8 Tensile strength (ultimate stress) of the hydrogel formulations

The highest tensile strength was observed for the pure PAM hydrogel, indicating that the unmodified polymer network maintained the greatest load-bearing capacity before failure. Upon incorporation of PDA, the tensile strength slightly decreased. Further addition of Fe_3O_4 and xGNP fillers did not surpass the strength of the PAM control. Instead, these nanoparticle reinforced composites exhibited moderate to reduced ultimate stress values, reflecting a more rigid yet brittle

structure that limits the ability to withstand high tensile loads. The LiCl-doped formulations particularly the 4.6 wt % group showed the lowest tensile strength overall.

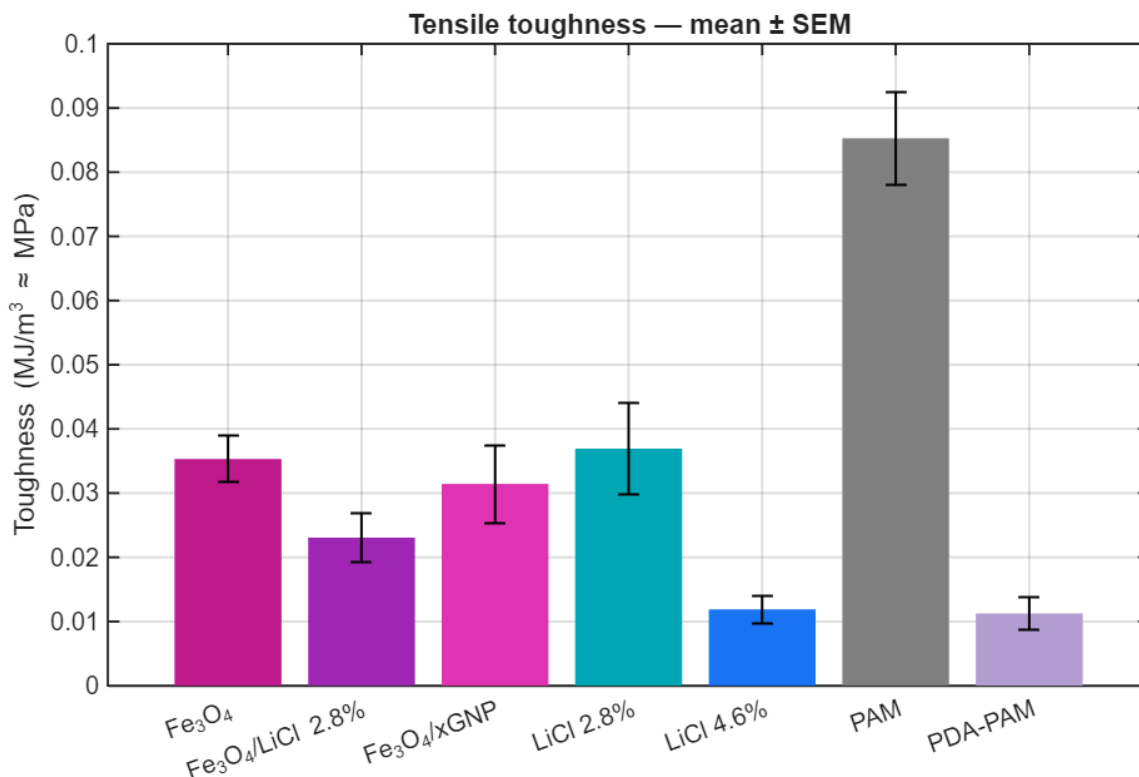


Figure 4.9 Tensile toughness (energy absorption, area under the stress–strain curve) of the hydrogel formulations.

The tensile toughness followed the same decreasing trend as tensile strength, with PAM revealing the highest energy absorption before failure. Introducing PDA slightly lowered toughness due to softer, reversible bonding. While Fe₃O₄ and xGNP fillers further reduced it by creating stiffer networks. The LiCl-doped gels showed moderate toughness from their higher stretchability, but excessive salt (4.6 wt %) weakened the network further.

4.4.2 Compression Results

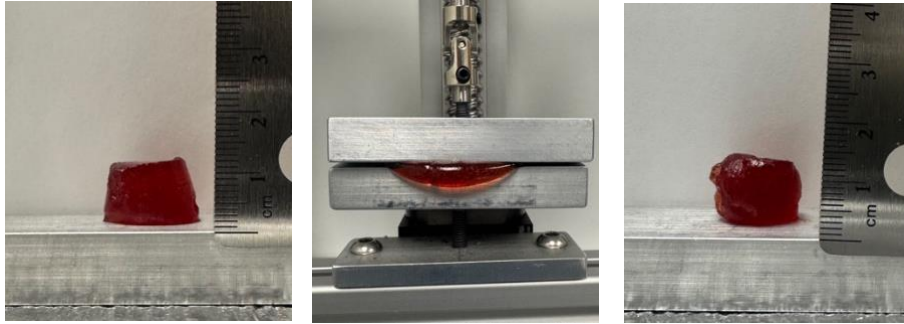


Figure 4.10 Photographs of the compression testing setup

Compression testing was conducted to assess the hydrogels' mechanical performance under load. A PDA-PAM hydrogel sample is shown in Figure 4.10, demonstrating the uniform cylindrical hydrogel and the basic setup used across all groups.

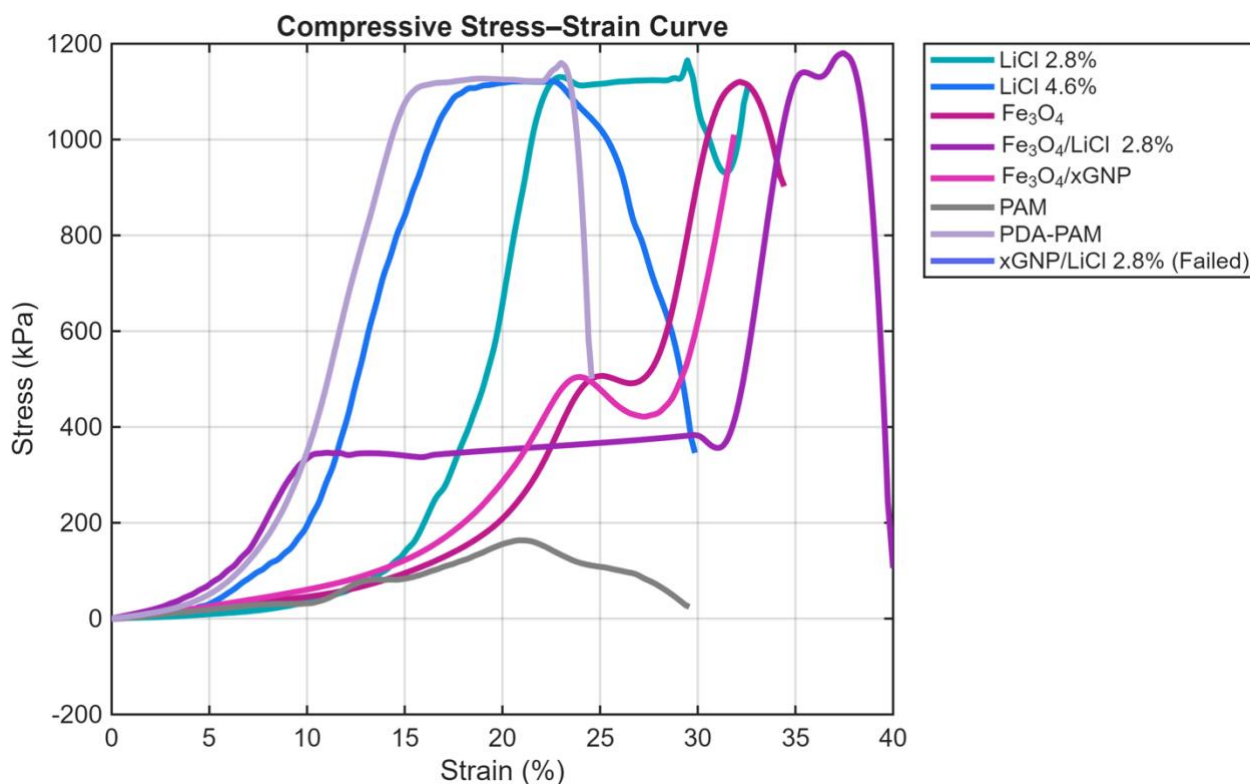


Figure 4.11 Compressive stress–strain curves for each hydrogel group.

The resulting compressive stress–strain curves shown in Figure 4.11 show distinct differences across formulations. PAM displayed a soft, easily compressible profile with low resistance to strain. Incorporating PDA increased the gel’s stiffness and delayed failure, while further reinforcement with Fe₃O₄ nanoparticles led to a much steeper curve and higher peak stress. Indicating enhanced load-bearing capability. Whereas gels containing LiCl displayed reduced mechanical integrity. The 2.8% LiCl group remained somewhat elastic, but at 4.6%, the network became overly plasticized, yielding prematurely under compression.

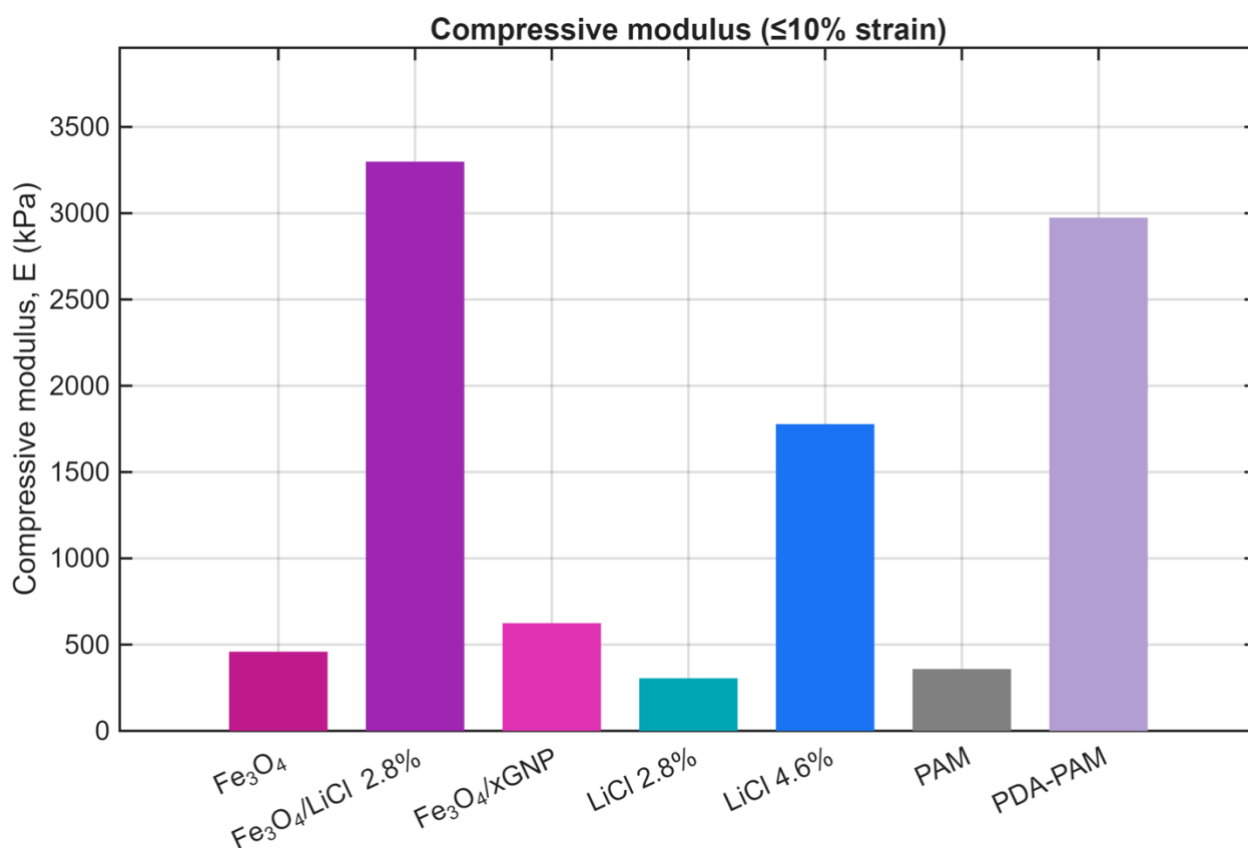


Figure 4.12 Compressive modulus, or average stiffness, of each hydrogel formulation. Bars represent the mean modulus obtained from the initial linear region of each stress–strain curve.

In Figure 4.12, the compressive modulus values calculated at 10% strain reveal substantial differences in stiffness across the hydrogel groups. The Fe₃O₄/LiCl 2.8% formulation displays the highest modulus, reaching over 3300 kPa, followed closely by PDA-PAM, which also maintains a notably stiff profile at ~3000 kPa. These results suggest that both ionic coordination from LiCl and the cohesive PDA network contribute to significant reinforcement of the hydrogel matrix. Interestingly, Fe₃O₄/xGNP, while expected to be highly reinforcing, shows a much lower modulus, indicating that graphene alone does not increase stiffness as effectively in this formulation. The

LiCl 4.6% group demonstrates intermediate stiffness at ~1800 kPa, higher than pure PAM, which has a modulus of ~500 kPa. However, far below PDA-PAM and Fe₃O₄/LiCl. Notably, the LiCl 2.8% gel is the softest, suggesting that at lower salt concentrations, ionic interference outweighs any potential reinforcing effect.

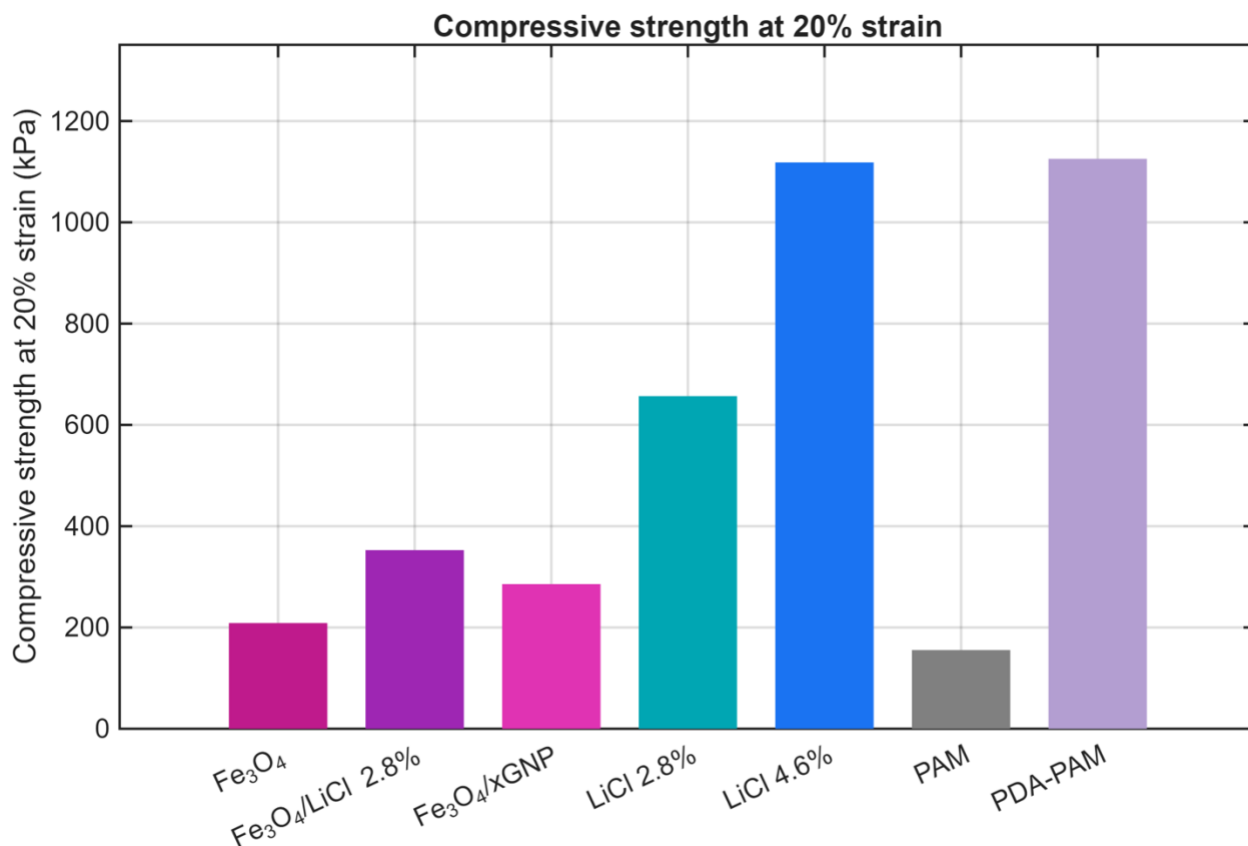


Figure 4.13 Compressive strength, the maximum stress before failure, of each hydrogel composite. Bars compare the peak load-bearing capacity of each formulation under compression.

On the other hand, Figure 4.13 shows compressive strength values measured at 20% strain, which follow a different trend. The highest strength is observed in LiCl 4.6% and PDA-PAM, both reaching approximately 1150–1200 kPa. This implies that while PDA-PAM retains stiffness, the salt-rich formulation can absorb and redistribute load under compression. The cause may be due to water migration or densification effects. LiCl 2.8% shows a drop in strength compared to 4.6%, as expected, but still outperforms many filler-based groups. Both $\text{Fe}_3\text{O}_4/\text{LiCl}$ 2.8% and $\text{Fe}_3\text{O}_4/\text{xGNP}$ show moderate strength, around 300–350 kPa. Fe_3O_4 alone registers the lowest at ~200 kPa. Despite having the highest modulus, $\text{Fe}_3\text{O}_4/\text{LiCl}$ 2.8% does not achieve the highest strength, indicating it may resist small strains but fails earlier under larger loads. PAM again serves as the soft baseline, barely exceeding 150 kPa.

4.4.3 Adhesion Results

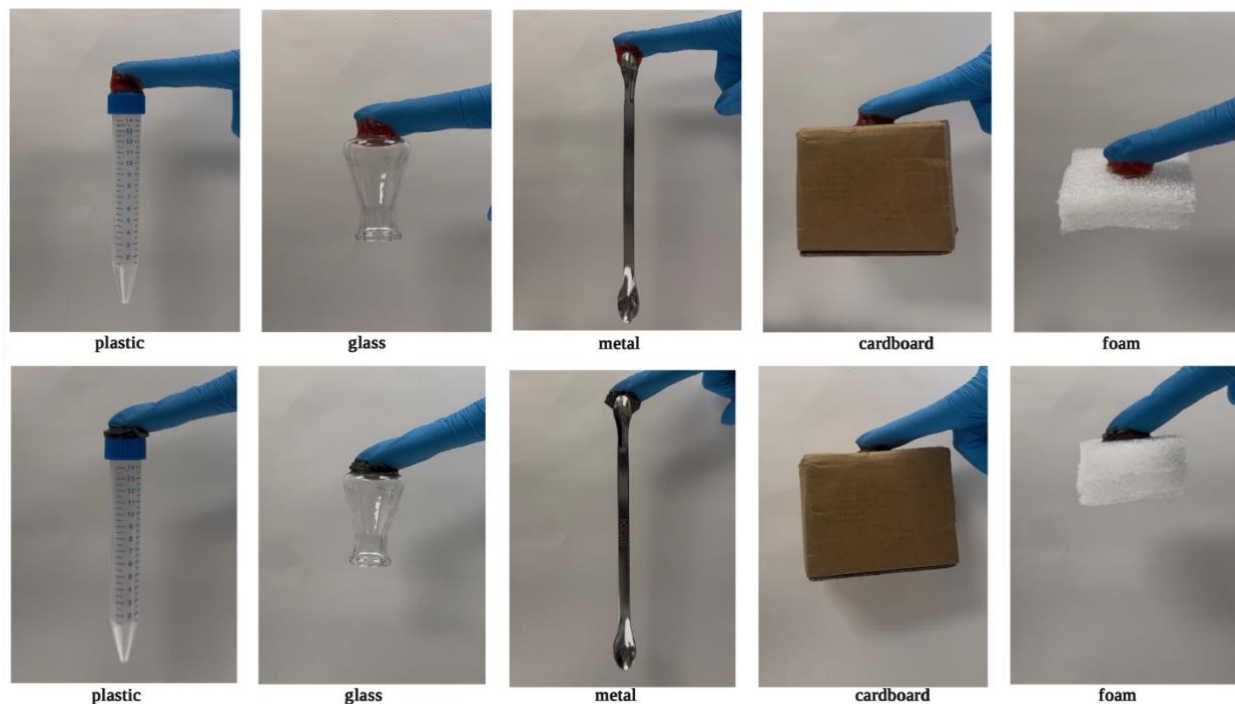


Figure 4.14 Adhesion demonstration of the PDA–PAM control group (top panel) and Fe₃O₄/xGNP/LiCl PDA–PAM experimental group (bottom panel). Both gels adhered to and lifted plastic, glass, metal, cardboard, and foam substrates when suspended between the gel and a gloved fingertip.

In the control group hydrogel tests, each substrate was successfully lifted by bonding one end of the gel to the gloved fingertip and the other end to the material (Figure 4.14, top). The gel formed strong contact with all five surfaces, with no slippage or detachment observed. This result is consistent with the well-known adhesive nature of PDA catechol networks, which readily stick

to a variety of materials. Similar mussel-inspired gels adhere effectively to both high energy (glass, metal) and low-energy (plastic, polymer) surfaces. In this test, even rough or porous substrates such as the cardboard and foam remained attached under the gel suggesting the control gel conformed to surface irregularities as well as maintained cohesive strength.

The experimental hydrogel performed identically. As shown in Figure 4.14 (bottom), every substrate was lifted in the same manner as with the control gel. In practice, the added Fe_3O_4 NPs, xGNP, and LiCl did not diminish adhesion. The experimental gel attached to plastic, glass, metal, cardboard, and foam with the same reliability as the undoped PDA–PAM. Thus, the adhesive strength was effectively identical for both formulations, indicating that the fillers did not disrupt the PDA catechol bonding or the gel's mechanical integrity. In summary, both gels exhibited vigorous interfacial contact and cohesion with all tested surfaces, and no quantitative difference in adhesion was evident between control and experimental groups.

4.5 Electrical Testing Evaluation

4.5.1 Conductivity Results

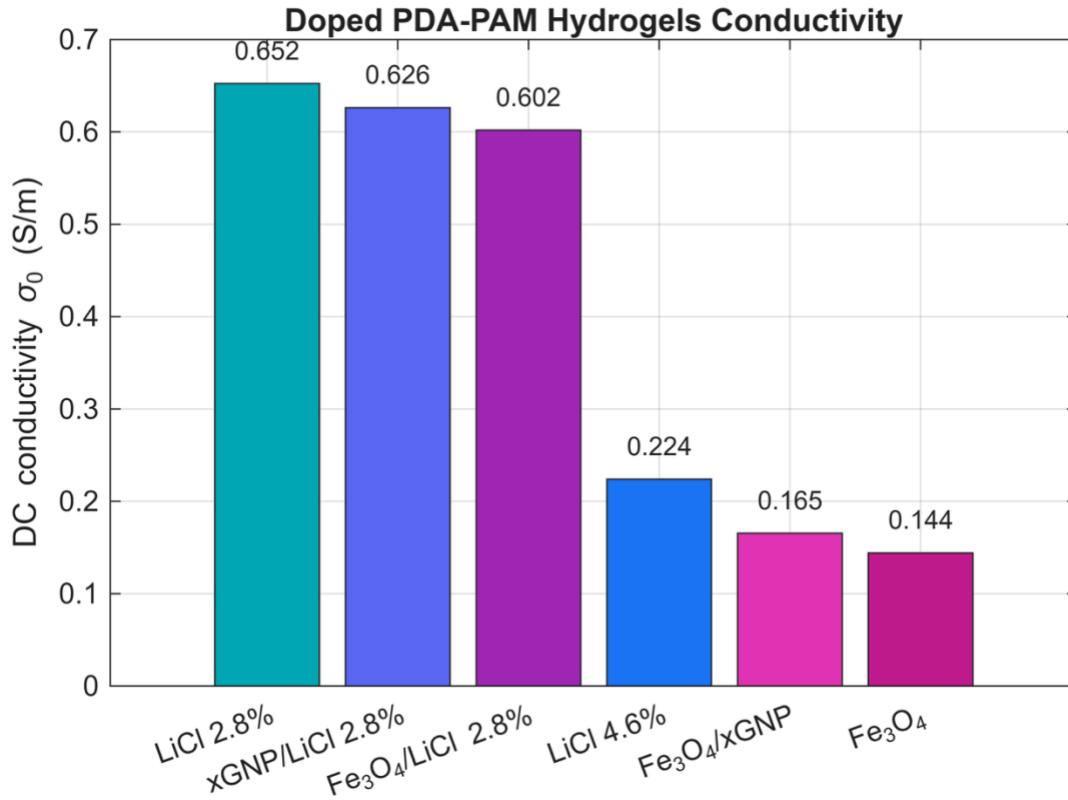


Figure 4.15 Average DC conductivity (σ_0) of doped PDA–PAM hydrogel formulations extracted from impedance spectroscopy. The LiCl 2.8 wt % hydrogel achieved the highest conductivity among all experimental groups. For full compositions and label definitions, refer to Table 3.2 (Section 3.2.3)

Ionic conductivity was measured by electrochemical impedance spectroscopy on each hydrogel. The real conductivity $\sigma(\omega)$ was extracted from the impedance spectra and plotted versus frequency. In all samples a low-frequency plateau (frequency-independent region) is shown

corresponding to the DC ionic conductivity σ_0 . The DC conductivity (σ_0) was obtained by fitting or averaging the conductivity within the low-frequency plateau region typically below ≈ 100 Hz, with all values converted from mS/cm to S/m (1 mS/cm = 0.1 S/m). Each hydrogel formulation was measured in triplicate. To ensure reliable results any extreme low outlier, such as those caused by defective samples or poor electrode contact, was discarded. And the two highest-conductivity replicates were averaged. Thus, the σ_0 values shown in Figure 4.15 represent the mean of the top two replicates. The results indicate that LiCl doping markedly enhances σ_0 . As shown in Figure 4.15, the LiCl (2.8 wt%) doped hydrogel exhibits the highest conductivity ($\sigma_0 \approx 0.652$ S/m) among all formulations. The incorporation of LiCl at this concentration introduces a large population of mobile Li^+ and Cl^- ions, which migrate through the hydrogel's water-rich microchannels and dynamically coordinate with carbonyl (C=O) and amide ($-\text{NH}_2$) groups of the PAM backbone as well as catechol moieties of PDA. These reversible ion-dipole interactions promote highly interconnected ionic pathways, resulting in a dramatic increase in σ_0 compared with the undoped control gels. Increasing the LiCl content to 4.6 wt% decreased the conductivity to 0.224 S/m, indicating that excessive ionic strength leads to ion-pairing and local dehydration effects that hinder carrier mobility. Thus, 2.8 wt% LiCl represents the optimal concentration for maintaining both high charge density and efficient ion diffusion. The presence of Fe_3O_4 or xGNP likely increases interfacial polarization and creates localized electron-hopping or double-layer conduction pathways that complement the dominant ionic transport. However, in the absence of LiCl, both $\text{Fe}_3\text{O}_4/\text{xGNP}$ ($\sigma_0 = 0.165$ S/m) and Fe_3O_4 -only ($\sigma_0 = 0.144$ S/m) hydrogels showed substantially lower conductivities, confirming that ionic carriers, not electronic fillers, primarily govern charge conduction in these hydrated systems.

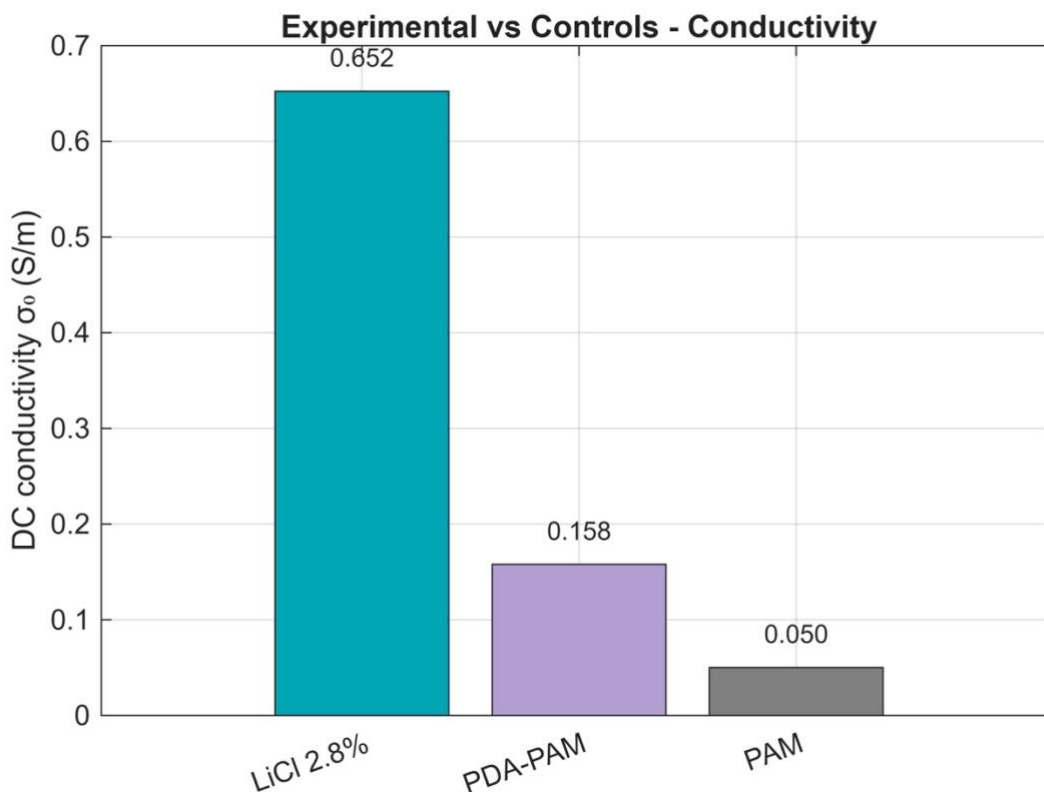


Figure 4.16 compares the best-performing LiCl-2.8% hydrogel directly to the PDA-PAM and PAM controls.

When compared against baseline controls as shown in Figure 4.16, the improvement achieved by ionic and composite doping becomes even more evident. The PDA-PAM control exhibited $\sigma_0 \approx 0.158$ S/m, while the pure PAM hydrogel registered $\sigma_0 \approx 0.050$ S/m. These results underscore that catechol functionality from PDA contributes moderately to charge transfer through proton-coupled electron hopping and improved water retention, yet ionic loading via LiCl provides a far greater effect enhancing conductivity by more than an order of magnitude.

Overall, the combination of optimized ionic content and polymer-dopant interactions defines the conductive performance hierarchy observed. The LiCl 2.8 wt% system demonstrates

superior carrier density and percolation efficiency without the mobility limitations associated with higher concentrations. Nanoparticle additives contribute structural reinforcement and secondary polarization pathways however remain auxiliary to the primary ionic conduction mechanism.

4.5.2 Chronoamperometry Results

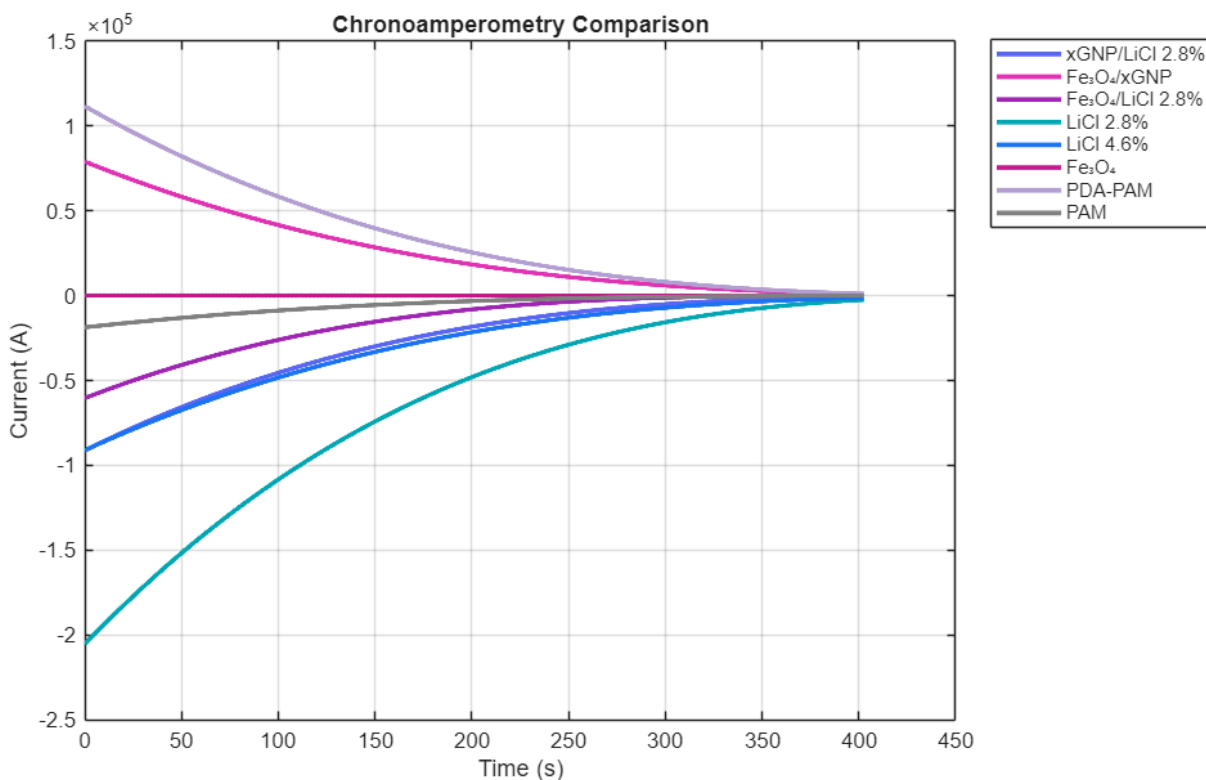


Figure 4.17 presents the mean chronoamperometric (CA) responses for all experimental and control hydrogel formulations, averaged over four replicates per group. The LiCl 2.8 wt. % sample demonstrated the largest initial current and slowest decay, reflecting efficient Li⁺ migration and balanced ionic–electronic conduction.

The 2.8 wt. % LiCl-doped hydrogel exhibited the highest initial current ($\approx 2.0 \times 10^{-4}$ A) and the most gradual decay toward equilibrium ($\approx 4.0 \times 10^{-5}$ A). The high peak current implies a large number of mobile charge carriers (Li^+ ions) and good ion mobility in the network. The slow decay of current also suggests a balance between capacitive and resistive transport after the initial transient, the Li^+ ions continue to migrate steadily under bias, maintaining charge transfer through the gel.

In comparison, the 4.6 wt. % LiCl sample showed a much lower initial current and a more rapid decay to steady state. Although some ions are present, the excessive salt appears to reduce performance. This behavior is consistent with “over-doping” effects. At high salt concentrations ion-ion interactions limit the number of free charge carriers. In polymer electrolytes, excess salt can exceed the matrix’s ability to solvate ions, causing recombination and a drop in ionic conductivity. The $\text{Fe}_3\text{O}_4/\text{LiCl}$ 2.8 % @ PDA-PAM and xGNP/LiCl 2.8 % @ PDA-PAM composites exhibited intermediate steady-state currents. Their modest current retention suggests that while the nanoparticles provide additional conductive pathways, partial agglomeration or polymer-filler interfacial resistance may slightly hinder full ion diffusion. The $\text{Fe}_3\text{O}_4/\text{xGNP}$ @ PDA-PAM hybrid produced a moderate curve showing that both fillers improve mixed conduction. Meanwhile, the Fe_3O_4 @ PDA-PAM gel, though magnetically active, exhibited lower current magnitudes ($\approx -4 \times 10^{-6}$ A), indicating that the absence of LiCl restricts ionic conduction despite its metallic character. The PDA-PAM and PAM controls yielded the weakest responses. In the context of this research, CA data directly relates to a sensor’s ability to maintain stable charge transfer over prolonged contact with biological tissue.

4.5.3 Cyclic Voltammetry Results

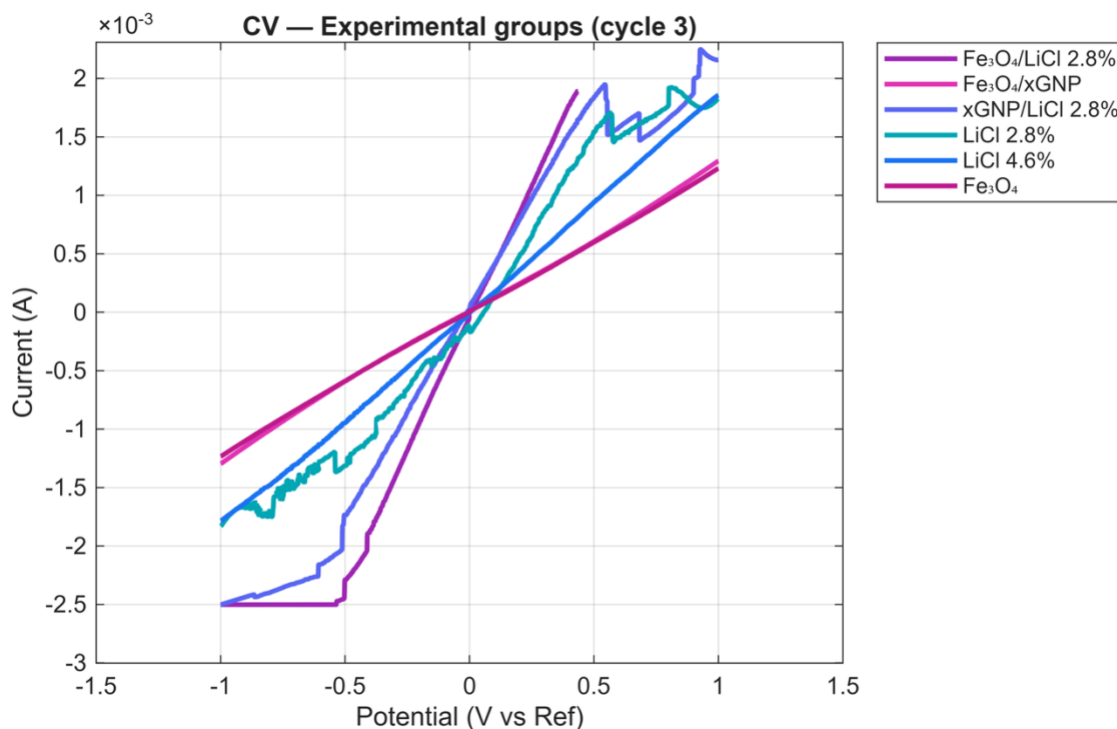


Figure 4.18 Cycle 3 - Average cyclic voltammetry curves comparing all experimental hydrogel variants.

The overlay of all cycle-3 CV curves shown in Figure 4.18 reveals clear differences among the six formulations. Hydrogels containing Fe₃O₄ nanoparticles exhibit pronounced redox peaks, reflecting the Fe²⁺/Fe³⁺ redox transitions and associated pseudocapacitance. In particular, the Fe₃O₄/LiCl (2.8%) composite shows the largest peak currents and broadest redox features. By contrast, the Fe₃O₄/xGNP sample also shows strong redox peaks which are slightly lower than the Fe₃O₄/LiCl sample, reflecting that graphene nanoplatelets provide a conductive network that effectively draws out the Fe₃O₄ pseudocapacitance. This is consistent with reports that graphene's

high conductivity and surface area enhance charge storage. The xGNP/LiCl electrode, which has no Fe_3O_4 , shows only moderate current with a nearly featureless, rectangular CV shape. This suggests primarily double-layer capacitance from the high-surface-area carbon plus increased ionic conductivity from LiCl however lacking faradaic peaks. This is expected in the absence of a redox-active metal oxide. The Fe_3O_4 sample, PDA-PAM matrix with Fe_3O_4 only, exhibits weak and poorly defined peaks of the lowest current. Finally, the LiCl-only doped hydrogels (2.8% and 4.6%) show very small and featureless voltammograms.

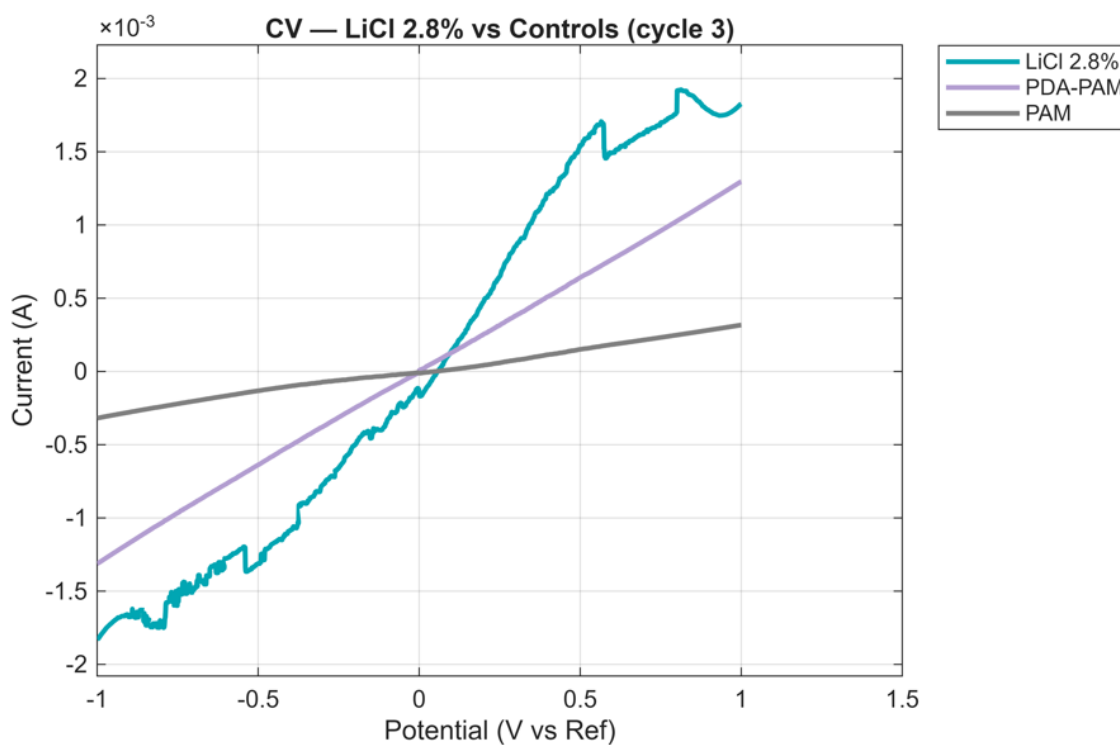


Figure 4.19 CV comparison of LiCl-doped versus control hydrogels (cycle 3). The LiCl 2.8% @ PDA-PAM hydrogel exhibits a much larger current response than either PDA-PAM or PAM.

A direct comparison of LiCl 2.8% with the undoped controls, PDA-PAM and PAM, underlines the essential role of LiCl as shown in Figure 4.19. Both PAM and PDA-PAM show very low currents and almost featureless CV profiles, indicating poor electrochemical response in the absence of added mobile ions. The LiCl-doped sample, however, exhibits a dramatic increase in both anodic and cathodic currents which are roughly 2–3× larger peaks and even hints of redox waves. This behavior demonstrates that introducing LiCl greatly boosts the ionic conductivity of the hydrogel matrix and enables more charge storage. The higher current and enclosed CV area with LiCl also suggests enhanced capacitive charge accumulation. Thus, LiCl doping converts an inert hydrogel such as PAM into a reasonably active electrode and can even unveil nascent pseudocapacitive peaks when combined with conductive phases.

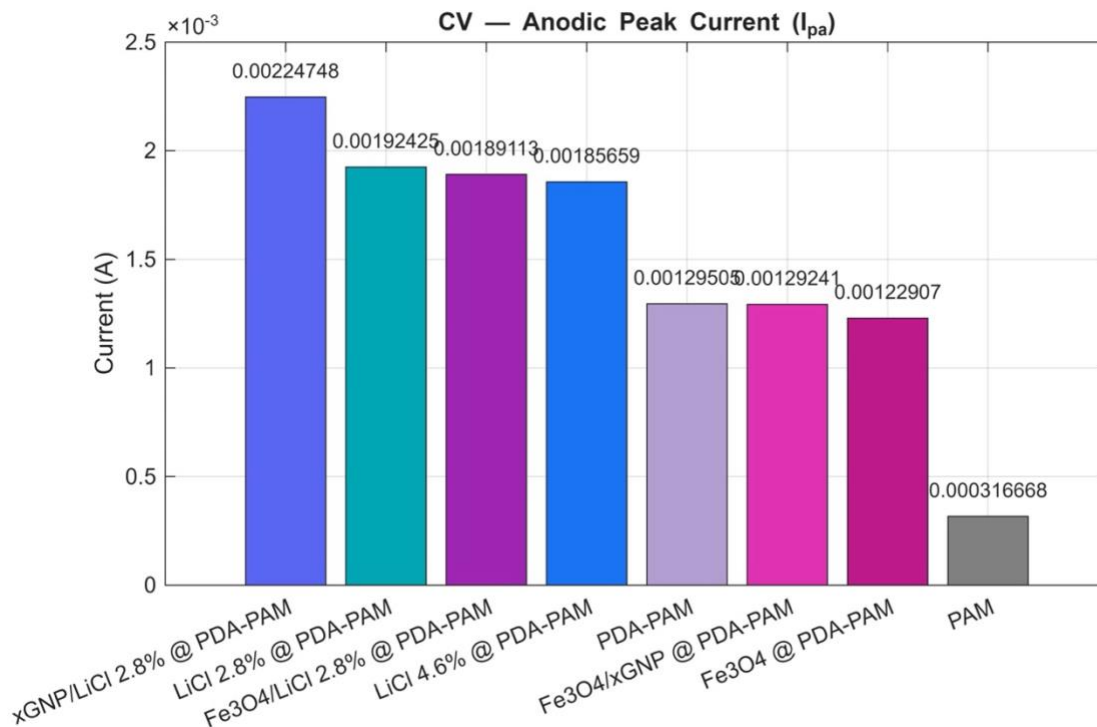


Figure 4.20 Anodic peak currents (I_{pc}) derived from CV measurements.

The xGNP/LiCl (2.8%) sample reaches the highest anodic peak current ($I_{pa} \approx 2200 \mu\text{A}$), markedly above all others. LiCl 2.8% is next ($\approx 1900 \mu\text{A}$), followed by Fe₃O₄/LiCl (2.8%) ($\approx 1800 \mu\text{A}$).

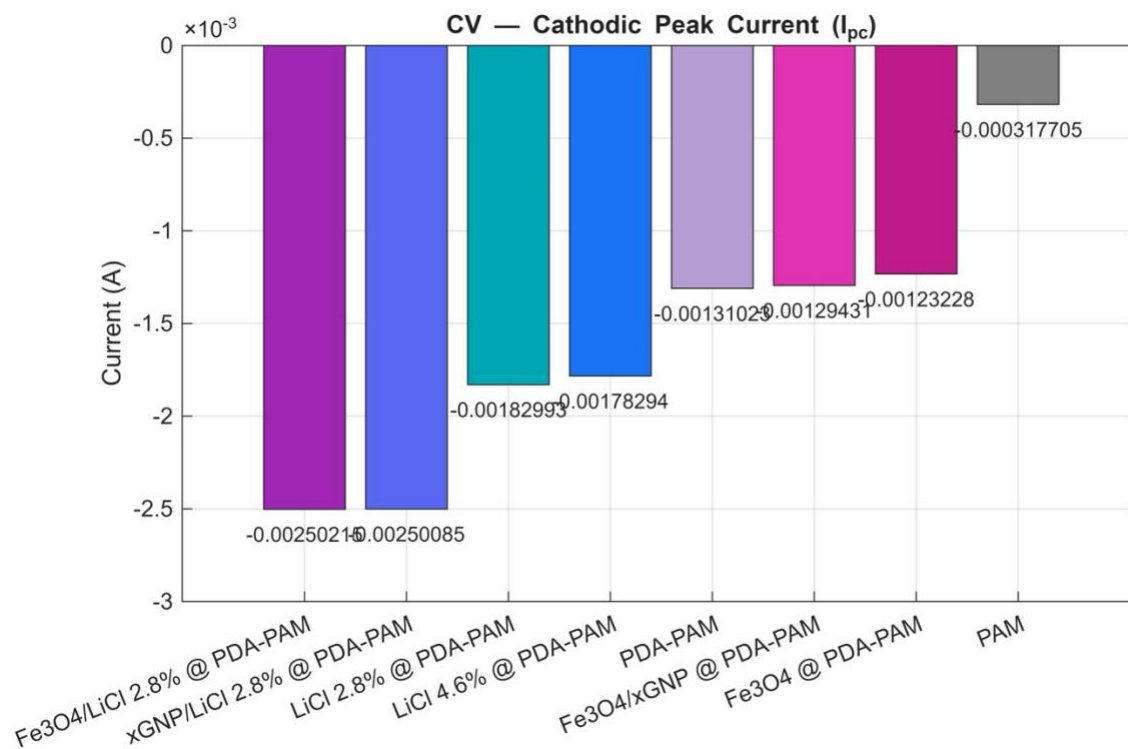


Figure 4.21 Cathodic peak currents (I_{pc}) derived from CV measurements.

The cathodic peaks presented in Figure 4.21 mirror the same ordering as the anodic peaks. Integrating the CV and peak current data reveals clear trends. Ionic dopants (LiCl) dramatically enhance performance by raising conductivity. This is seen in the jump from inert polymer to active LiCl-doped gels. Conductive nanocarbons (xGNP) increase double-layer capacitance and improve electron transport, which explains why Fe₃O₄/xGNP outperforms Fe₃O₄ alone. Redox-active particles such as Fe₃O₄ introduce Faradaic pseudocapacitance, as evidenced by the distinct peaks and extra charge storage. Combinations of two elements are better than either alone. The highest currents occur in bi-component systems that pair Fe₃O₄ with LiCl or with xGNP. This synergy is consistent with literature reports that metal-oxide/graphene hybrids or ionically doped polymers

deliver higher capacitance than single-phase materials. The large peak currents and well-defined redox waves in the best composites imply higher capacitance and faster kinetics, which translate to improved energy and power densities. The demonstration that a “triad” strategy embedding redox particles (Fe_3O_4), conductive nanocarbon (xGNP), and ionic salt (LiCl) in a PDA-PAM matrix markedly boosts electrochemical output is especially relevant. Such multi-component hydrogels can store more charge and deliver stronger signal response in sensing than plain polymer gels. In summary, the CV data show that tailoring hydrogel electrodes with both conductive additives and dopants can achieve synergistic enhancements in capacitance and redox activity.

4.6 Physiological Signal Sensing (ECG Signals)

4.6.1 Control Group Results

1. Resting State

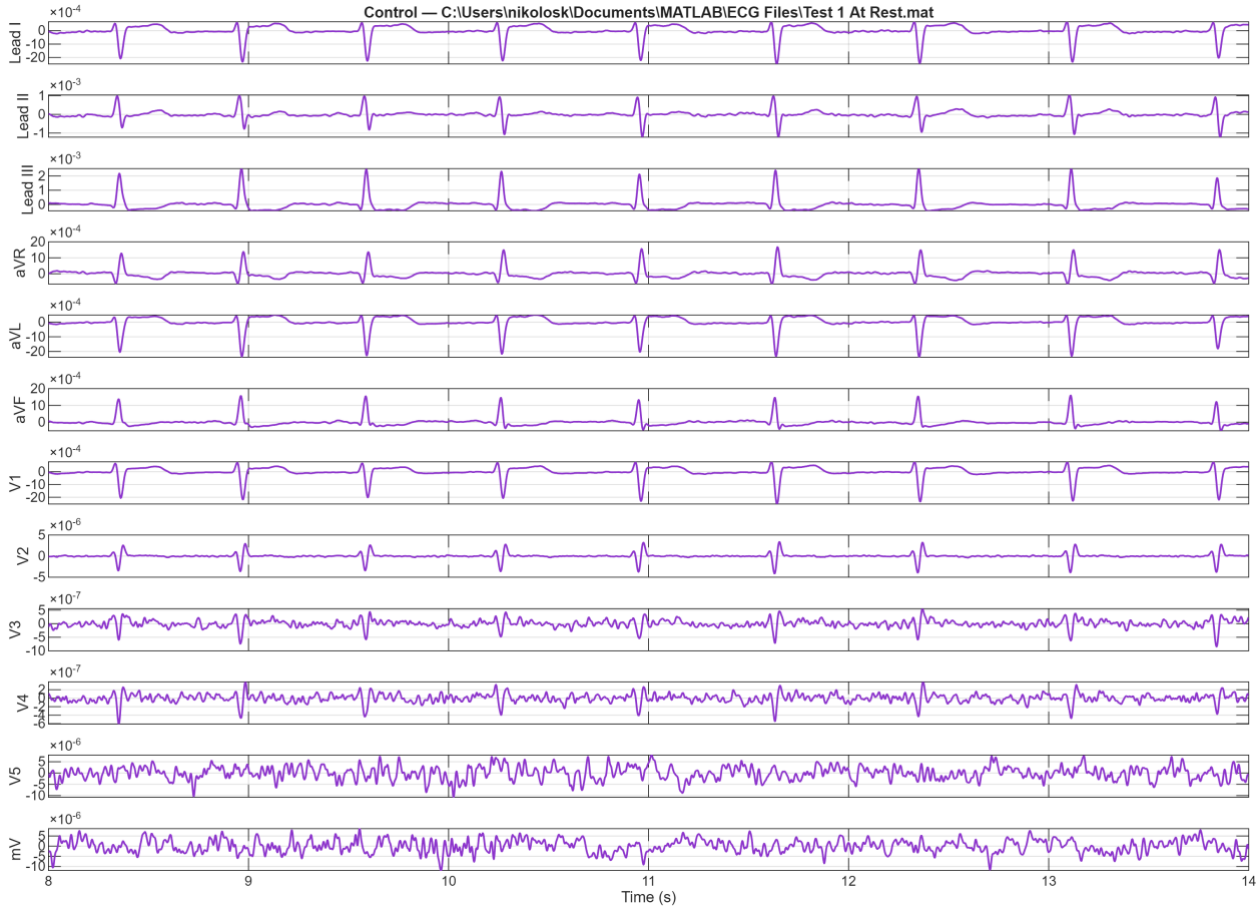


Figure 4.22 Control Group Test 1 – At Rest. (12 Lead Stacked ECG) Segment shown corresponds to $t = 8$ s

The 12-lead ECG recordings for the control group, shown in Figure 4.22, were obtained using the PDA-PAM hydrogel. All major waveform components such as P wave, QRS complex,

and T wave are visible across the leads, confirming successful signal acquisition. However, the isoelectric baseline between beats shows a slight low-frequency drift, suggesting minor instability in electrode-skin contact. There are also small and rapid fluctuations consistent with ambient noise.

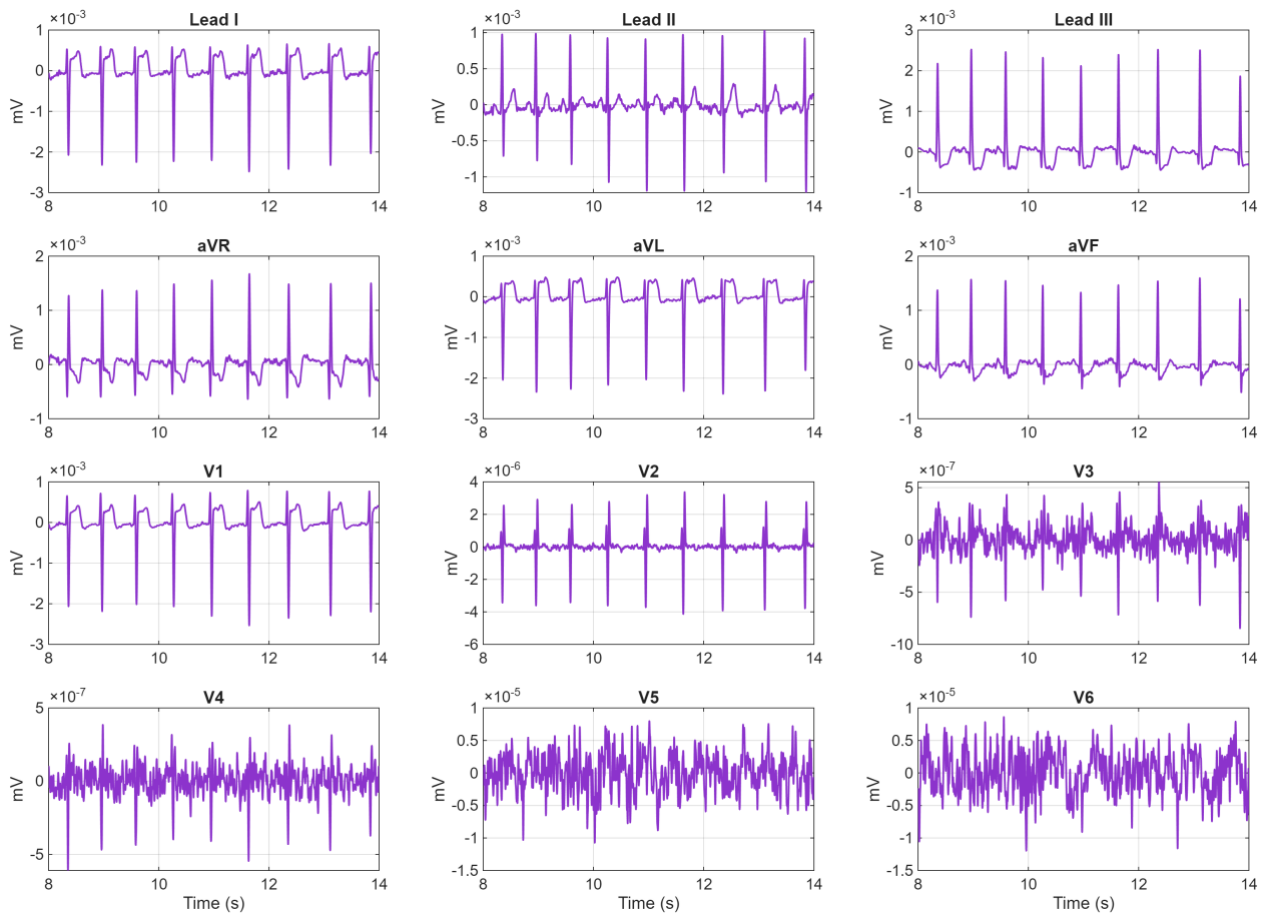


Figure 4.23 Control Group Test 1- At Rest (ECG Grid View) Segment shown corresponds to $t = 8$ s.

The standard 12-lead grid view in Figure 4.23 reinforces these observations. Each lead shows normal ECG morphology and amplitude, confirming correct lead placement. As with the stacked traces, some leads exhibit slight baseline offsets or tilts between complexes. This points to residual drift or imbalance.

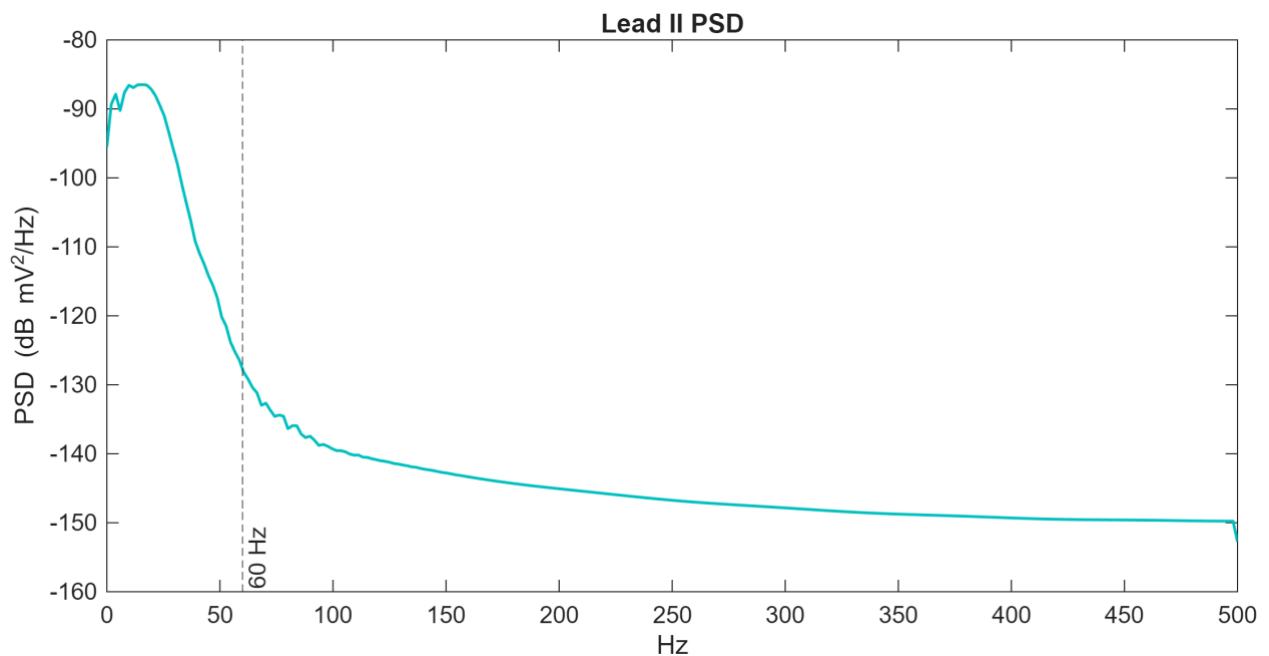


Figure 4.24 Control group test 1 - At rest (power spectral density of lead II). Segment shown corresponds to $t = 8$ s.

The frequency-domain representation in Figure 4.24 quantifies these issues through the power spectral density (PSD) of Lead II. Most signal power lies below ~ 10 Hz, reflecting heart rate fundamentals and harmonics that carry the ECG's physiological information. A distinct spectral peak near 60 Hz shows substantial mains interference. This is a common indicator of unstable electrode contact and a contributor to the noisy baseline seen in the time series.

2. Squat Activity (10 continuous standing squats)

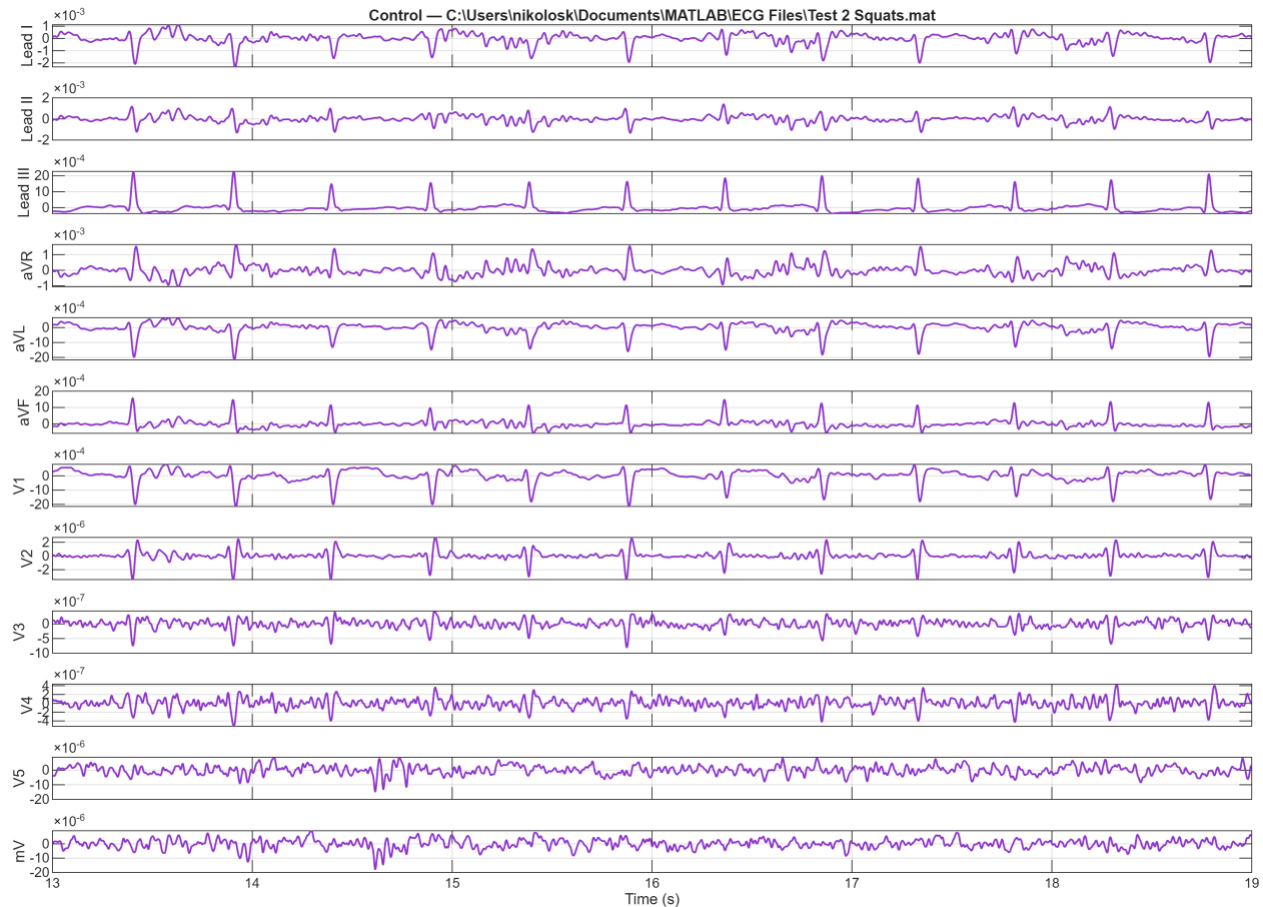


Figure 4.25 Control group test 2 - squat (12 lead stacked ECG). Segment shown corresponds to $t = 13$ s

The control group 12-lead ECG traces in Figure 4.25 show distinguishable P, QRS, and T components, however the waveforms are partially obscured by noise. In particular, the isoelectric baseline shows slow wander between beats, and small high-frequency fluctuations. This is likely due to muscle or motion artifact overlay the signal. These features degrade the clarity of the P and T waves. Despite the artifacts, the major QRS complexes remain identifiable. The overall

morphology suggests that low-frequency baseline drift and sporadic electrode/muscle noise are present.

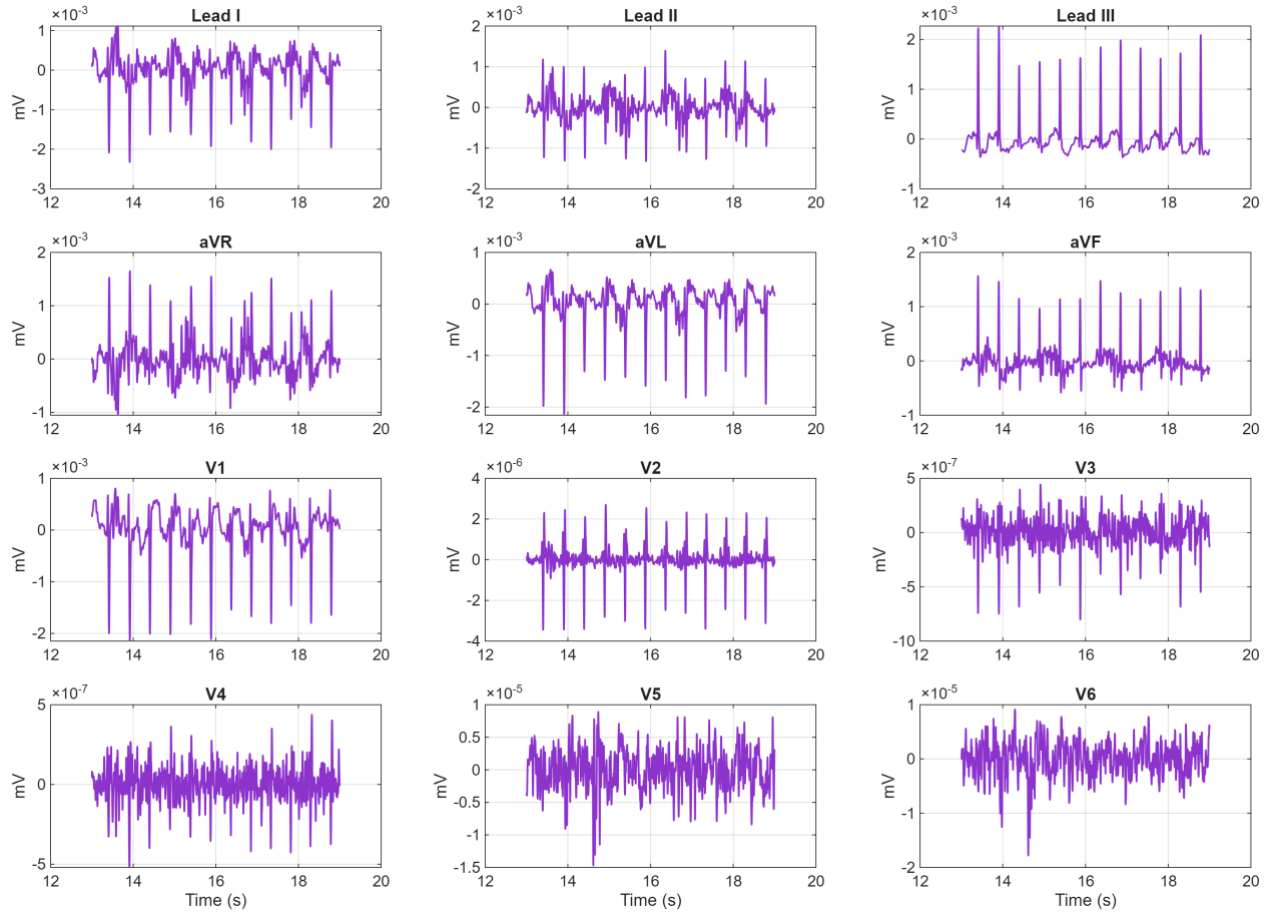


Figure 4.26 Control group test 2 - squats (ECG grid view). Segment shown corresponds to $t = 13$ s

Viewing the control data on a standardized ECG grid in Figure 4.26 confirms the baseline instability. The baseline shifts upward and downward slowly, and beat-to-beat amplitudes vary slightly. Minor high-frequency wiggles on the trace indicate muscle tremor or cable vibration.

The frequency-domain plot of Lead II for the control group in Figure 4.27 shows distinct peaks and a broadband noise floor. A sharp spike appears at ~60 Hz, attributable to mains interference, confirming that power-line noise contaminates the recording. Lower-frequency content (<0.5 Hz) is elevated, reflecting the baseline wander seen in the time traces. The dominant peak near 1–2 Hz corresponds to the heart rate (e.g. ~1.5 Hz for ~90 bpm). Additional spectral components in the 10–50 Hz range represent muscle and motion artifacts. In sum, the control PSD for test 2 reveals strong mains interference and baseline drift energy, as well as broadened peaks indicative of windowing effects and high-frequency noise.

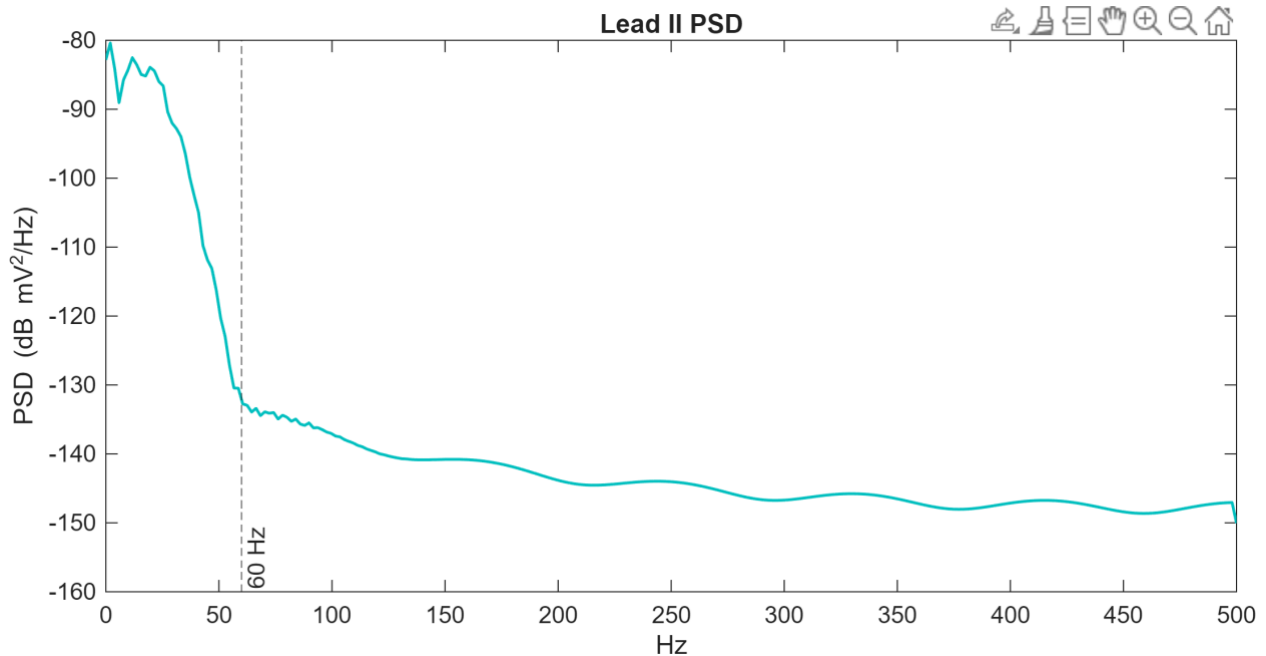


Figure 4.27 Control group test 2 - squats – (power spectral density of lead II). Segment shown corresponds to $t = 13$

s.

4. Push Up Activity (10 full pushups)

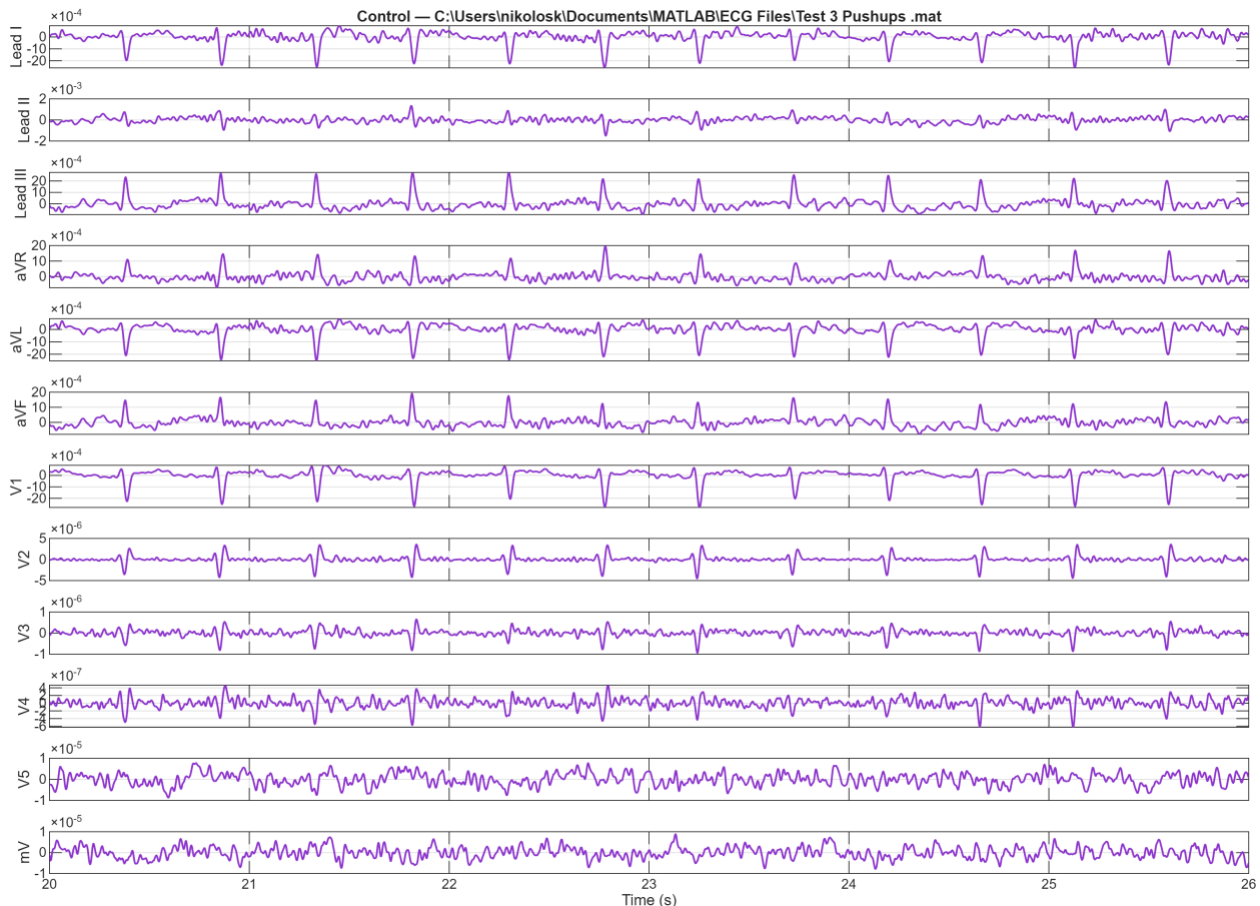


Figure 4.28 Control group test 3 - push ups (12 lead stacked ECG) Segment shown corresponds to $t = 20$ s

The multi-lead ECG shown in Figure 4.28 during push-ups shows clear P–QRS–T cycles in all leads, but with noticeable baseline drift and transient distortions. The control traces exhibit low-frequency wander on the order of a few millivolts, reflecting breathing and body motion. The

QRS amplitude is generally consistent, yet each heartbeat's baseline reference moves slightly between beats. Occasional large-amplitude spikes are evident during exertion phases, consistent with motion artifacts. Despite this noise, the cardiac waveform morphology remains identifiable, indicating that the fundamental ECG signal is still captured.

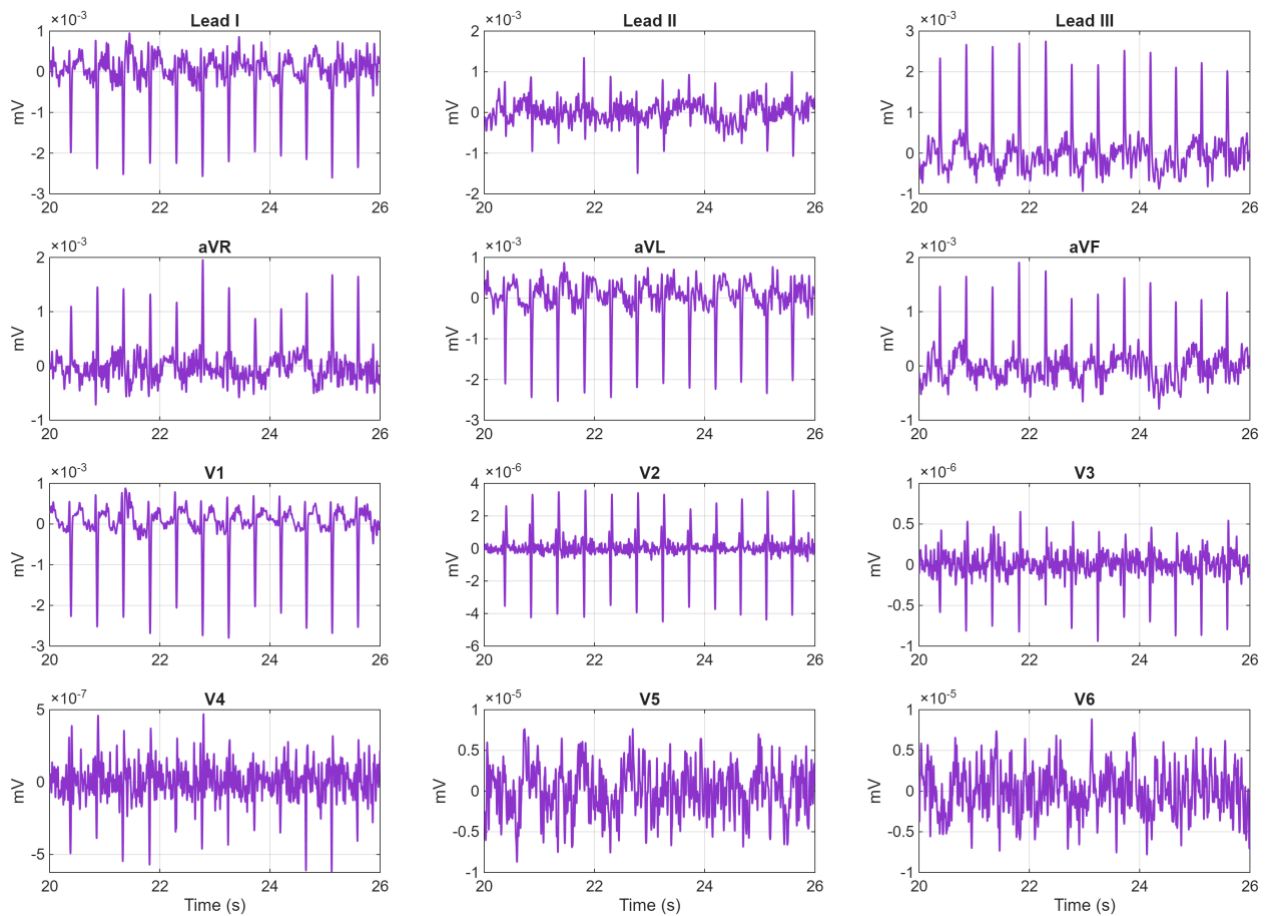


Figure 4.29 Control group test 3 - push-ups (ECG grid view). Segment shown corresponds to $t = 20$ s

Focusing on Lead II displayed in Figure 4.29 accentuates the control signal detail. The waveform shows well-formed R-peaks, but the baseline drifts quasi-periodically due to posture and respiration. There is higher-frequency jitter superimposed on the ECG likely muscle noise from active chest muscles and small electrode movements. The trace contains no flat-line dropouts however smaller components are partially obscured by noise. In summary, the control ECG trace is moderately stable but exhibits motion-induced perturbations consistent with known ambulatory ECG artifacts.

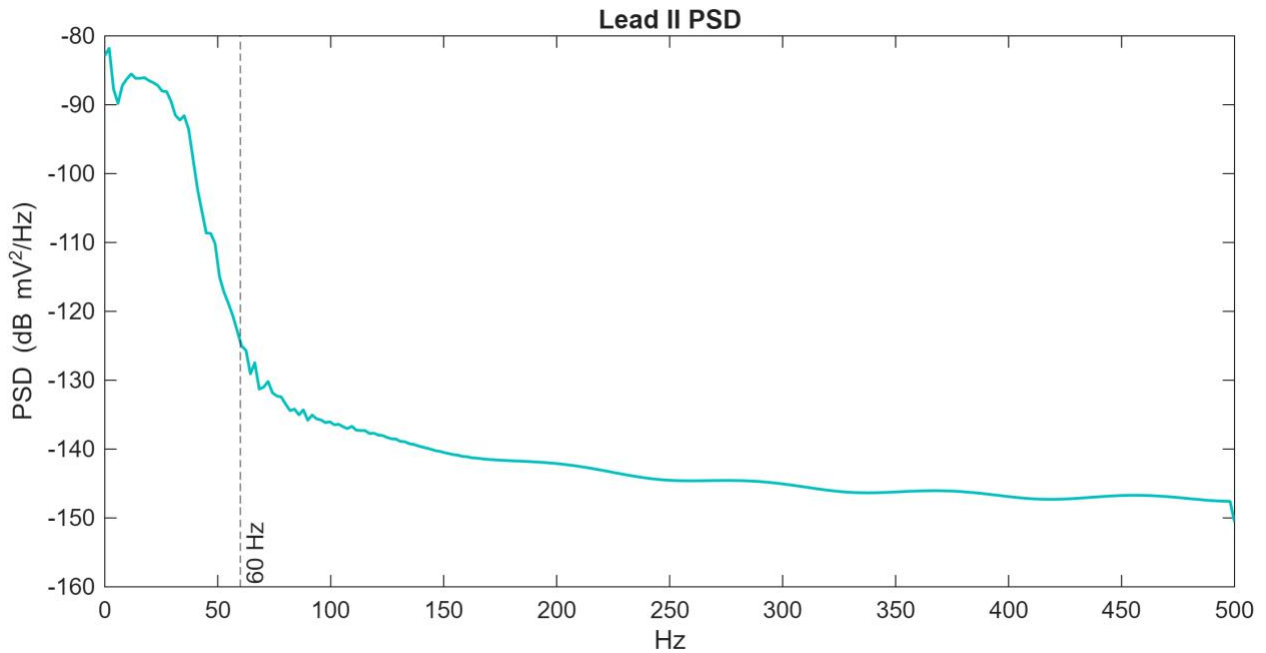


Figure 4.30 Control group test 3 – push-ups (power spectral density of lead II) Segment shown corresponds to $t = 20$ s.

The PSD of the control Lead II signal shows a dominant peak at the heart-rate frequency ($\sim 1\text{--}2$ Hz, corresponding to the subject's pulse) as seen in Figure 4.30. A sharp spike at ~ 60 Hz is present, indicating power-line interference. Above the cardiac fundamental, there is a broad elevation of power spanning roughly $10\text{--}40$ Hz, reflecting muscle and motion noise from the exercise. Likewise, substantial power appears below ~ 0.5 Hz, corresponding to baseline wander. Overall, the control PSD contains both the expected cardiac spectral content and significant broadband noise from movement.

4.6.2 Experimental Group Results

1. Resting State

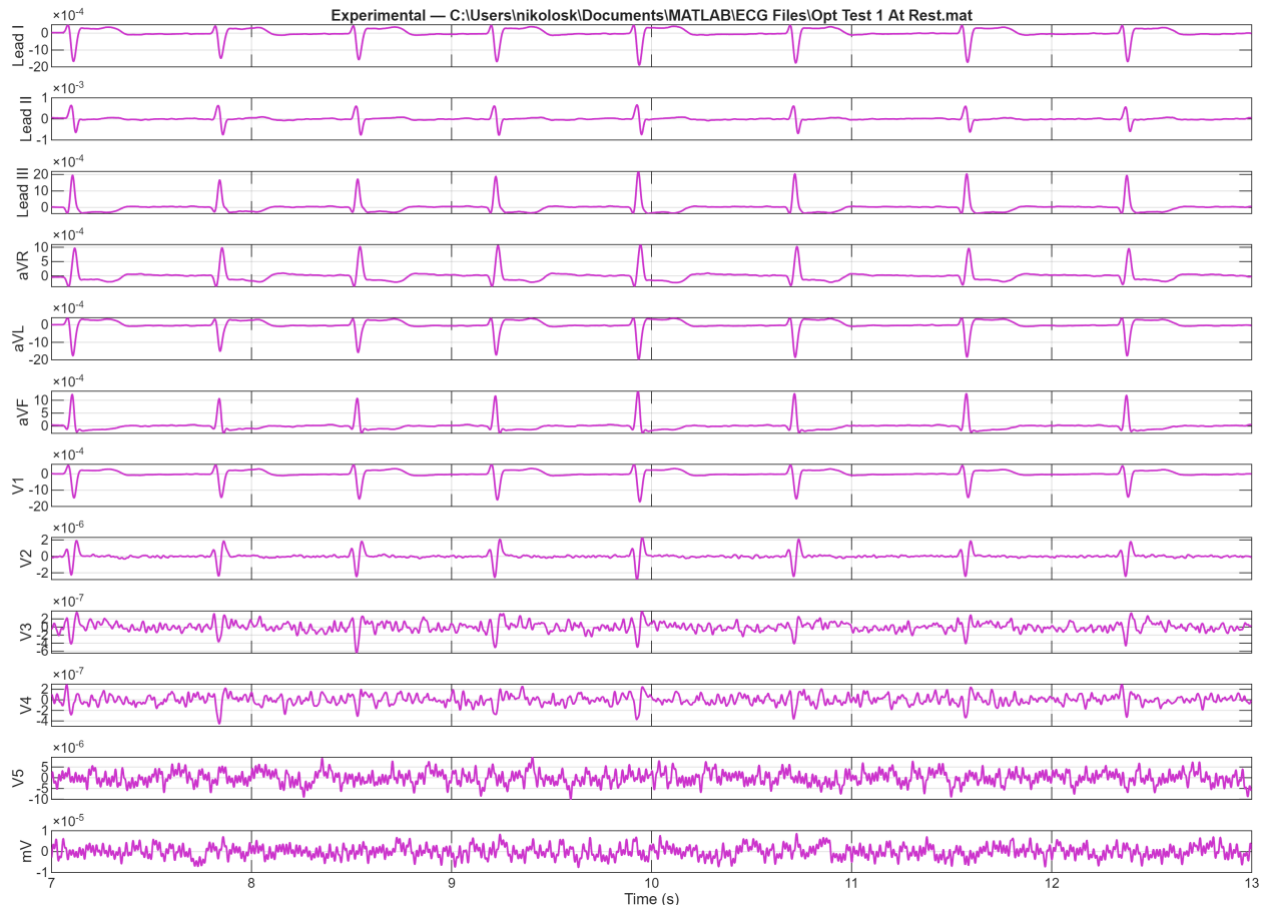


Figure 4.31 Experimental group test 1 – at rest (12 lead stacked ECG). Segment shown corresponds to $t = 7$ s

The 12-lead ECG traces for the experimental group, recorded using the experimental hydrogel, are shown in Figure 4.31. As with the control, all expected cardiac components such as the P wave, QRS complex, and T wave are clearly captured across leads. However, the baseline

between beats is now significantly flatter, with minimal low-frequency drift, indicating much more stable electrode–skin contact. This improvement directly addresses the baseline instability seen in the control. The traces also appear smoother, with fewer high-frequency fluctuations.

In Figure 4.32, the experimental ECG is presented in the standard 12-lead grid format. All leads again show proper ECG morphology with no missing channels. The isoelectric baseline across all leads is flat and well-aligned, with no visible drift or offset between beats. The lack of baseline jitter confirms that both motion and electrical interference have been effectively minimized. This clean and uniform presentation across the grid suggests that the experimental hydrogel consistently maintains strong electrode contact.

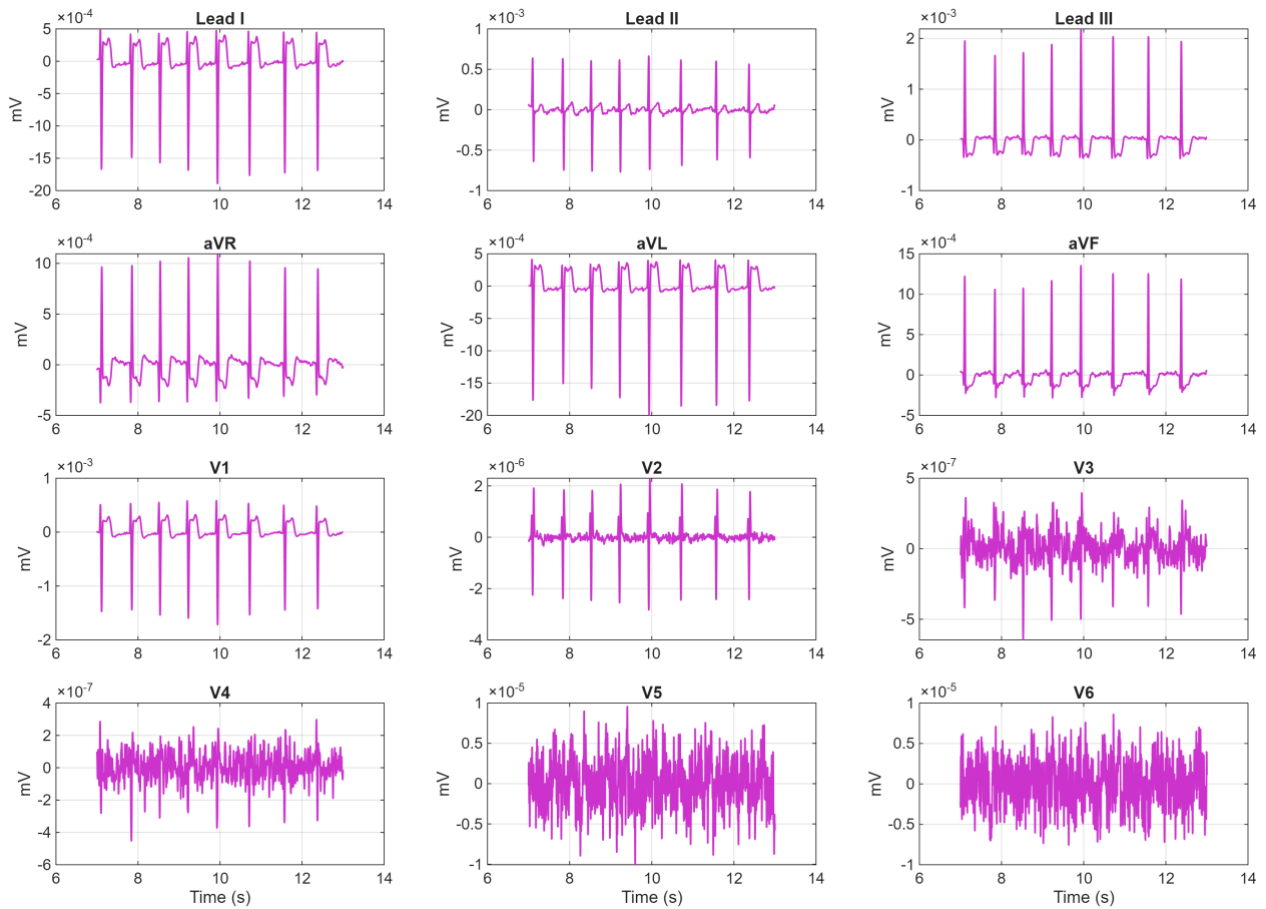


Figure 4.32 Experimental group test 1- at rest (ECG grid view). Segment shown corresponds to $t = 7$ s.

The PSD of the experimental group shown in Figure 4.33 further emphasizes the improvements. Strong peaks appear at ~ 1 Hz and its harmonics (~ 4 – 7 Hz), corresponding to the heart rate and waveform components. The magnitude of these cardiac peaks is much higher relative to the noise floor. The very-low-frequency region (< 0.5 Hz) is virtually empty, indicating that baseline drift has been nearly eliminated by the stable electrode interface. In other words, virtually no power is present where wandering normally appears. The frequency-domain profile matches that of a high-fidelity ECG with most spectral power concentrated in the physiological bands.

Overall, the experimental PSD exhibits a clean spectral signature with prominent cardiac peaks and an exceptionally low noise floor.

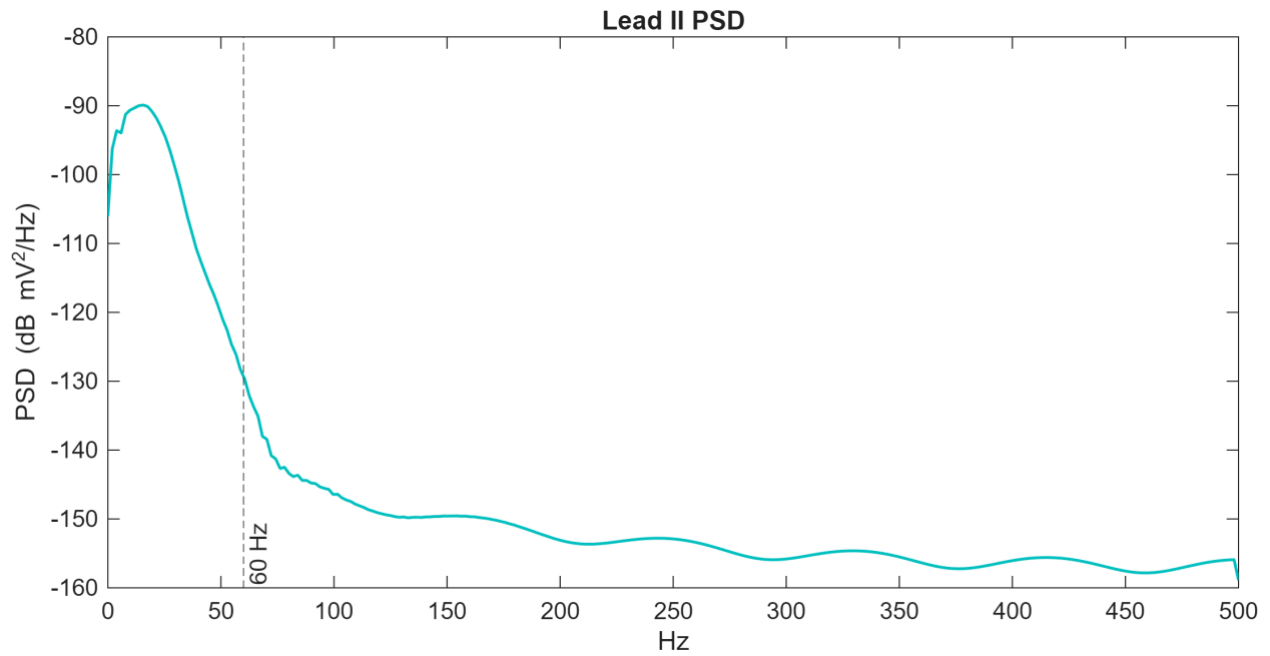


Figure 4.33 Experimental group test 1 – at rest (power spectral density of lead II) Segment shown corresponds to $t = 7$ s.

2. Squat Activity (10 continuous standing squats)

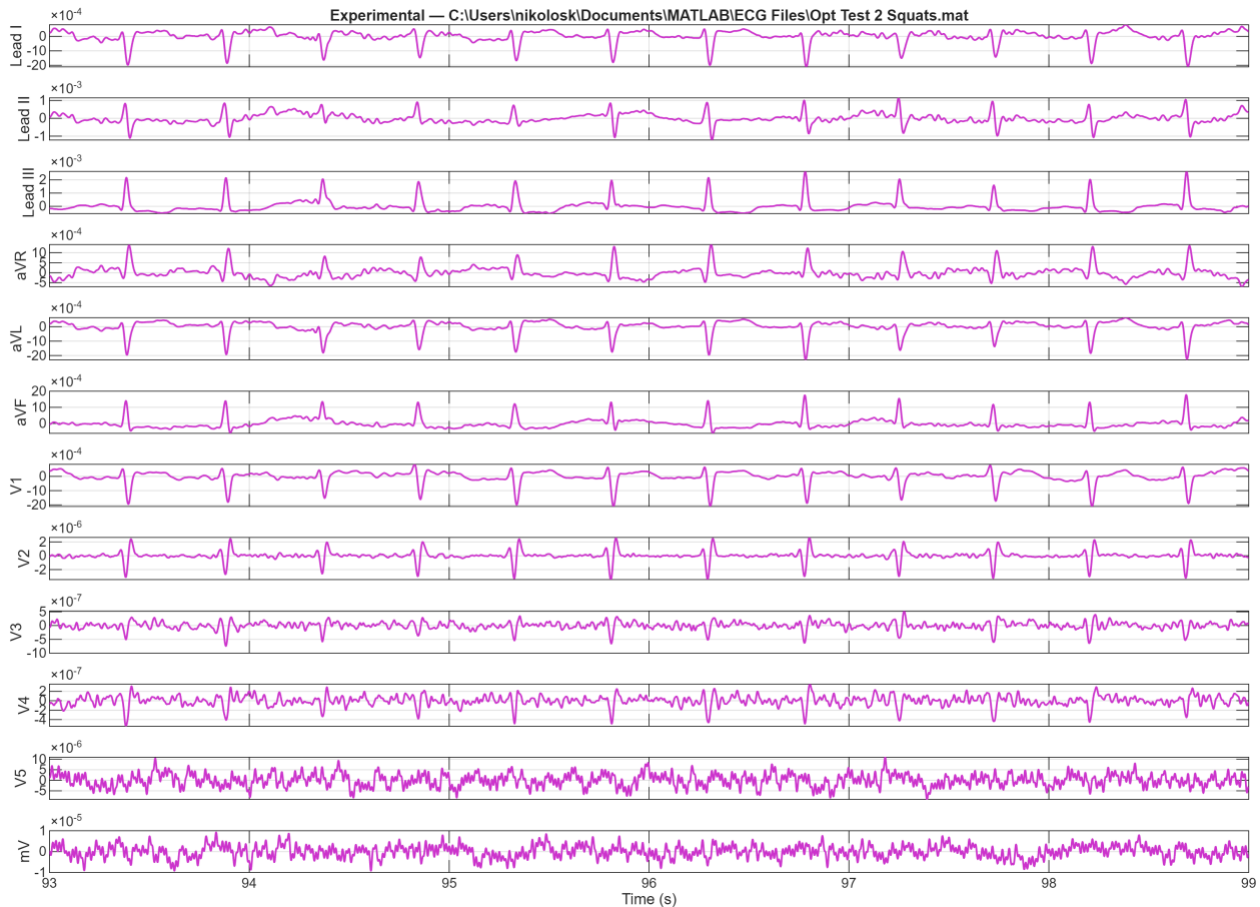


Figure 4.34 Experimental group test 2 – squats (12 lead stacked ECG). Segment shown corresponds to $t = 93$ s.

The experimental-group 12-lead traces illustrated in Figure 4.34 display noticeably cleaner waveforms. The baseline is much steadier between beats, and the P–QRS–T complexes appear sharper. Motion artifacts are substantially reduced the characteristic slow wander is minimal, and the high-frequency muscle-like noise is attenuated. Consequently, the morphological features of

each heartbeat stand out clearly. This indicates that the experimental group effectively suppresses drift.

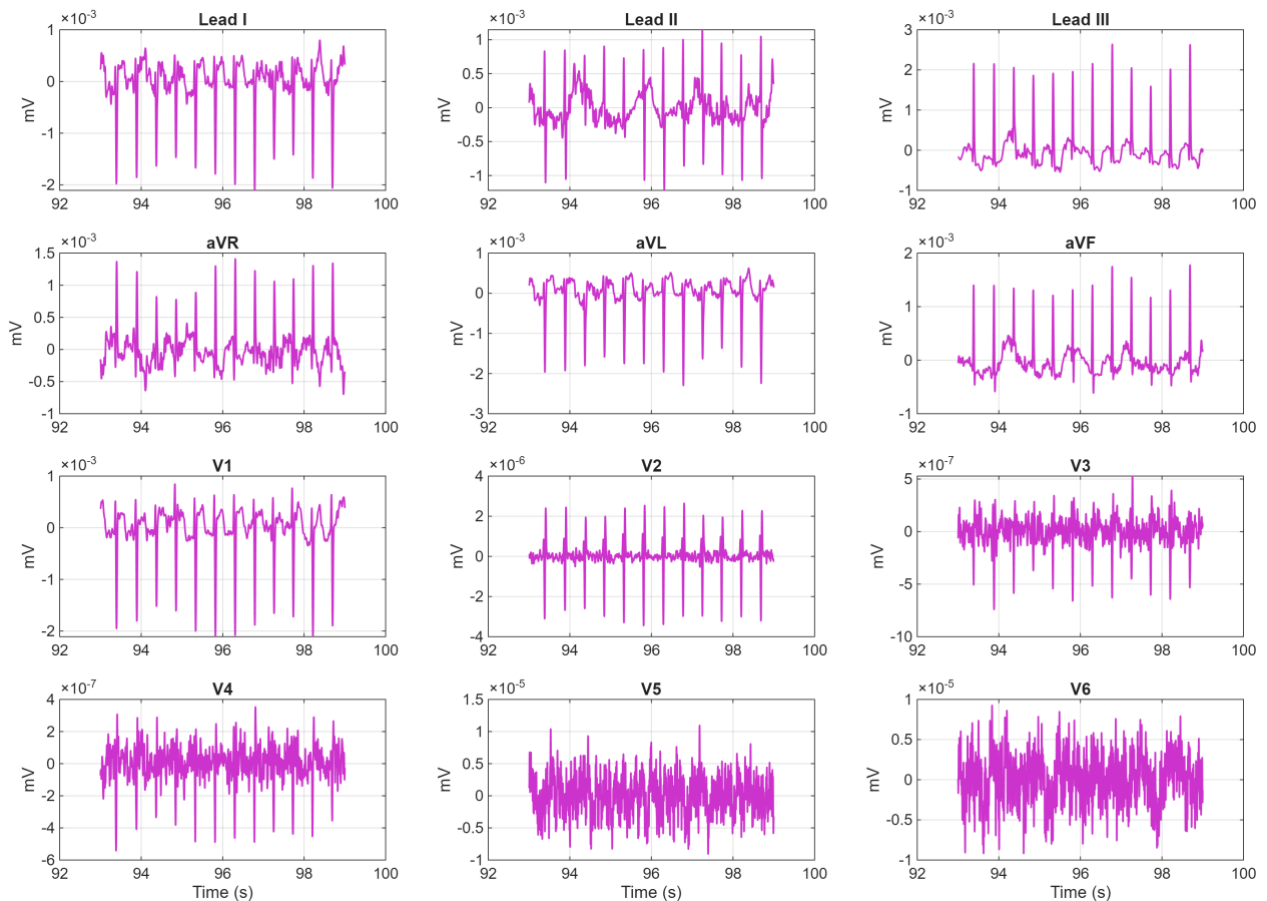


Figure 4.35 Experimental group test 2 - squats (12 lead stacked ECG). Segment shown corresponds to $t = 93$ s.

On the ECG grid in Figure 4.35, the experimental traces confirm the improvements in stability. The isoelectric baseline is essentially flat, with only slight undulations, showing that low-frequency drift has been largely mitigated. The R–R intervals are consistent and are reflecting a regular heart rhythm undisturbed by noise. Overall, the cardiac cycle amplitudes

remain constant, and waveform contours are crisp. These observations suggest that common artifacts have been suppressed in the experimental recording.

The PSD of Lead II for the experimental group has a cleaner profile. Taking a look at Figure 4.36 the mains-frequency peak at ~ 60 Hz is much smaller indicating effective reduction of powerline interference. Low frequency power below ~ 0.5 Hz is lower than in the control group., confirming the removal of baseline wander. The heart-rate peak remains prominent, but the surrounding noise floor is reduced. Importantly, the spectral lines are narrower and show fewer side lobes. This reflects reduced spectral leakage and less broadband contamination.

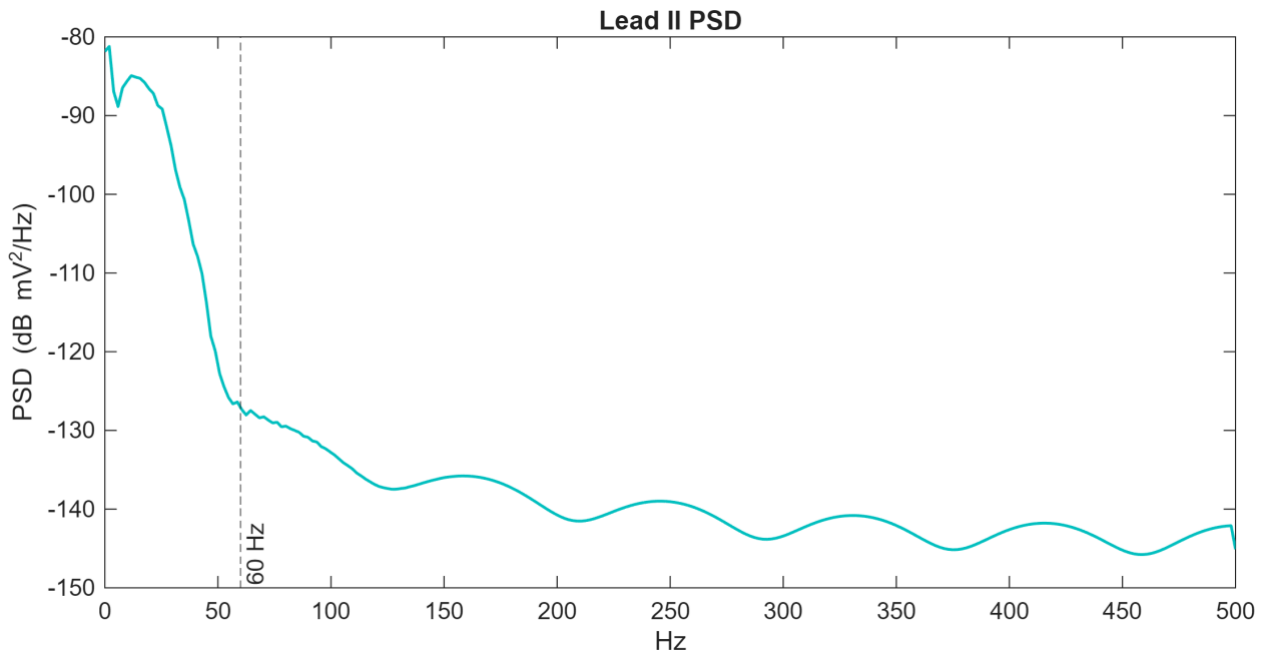


Figure 4.36 Experimental group test 2 - squats (power spectral density of lead II).

Segment shown corresponds to 93 s.

3. Push Up Activity (10 full pushups)

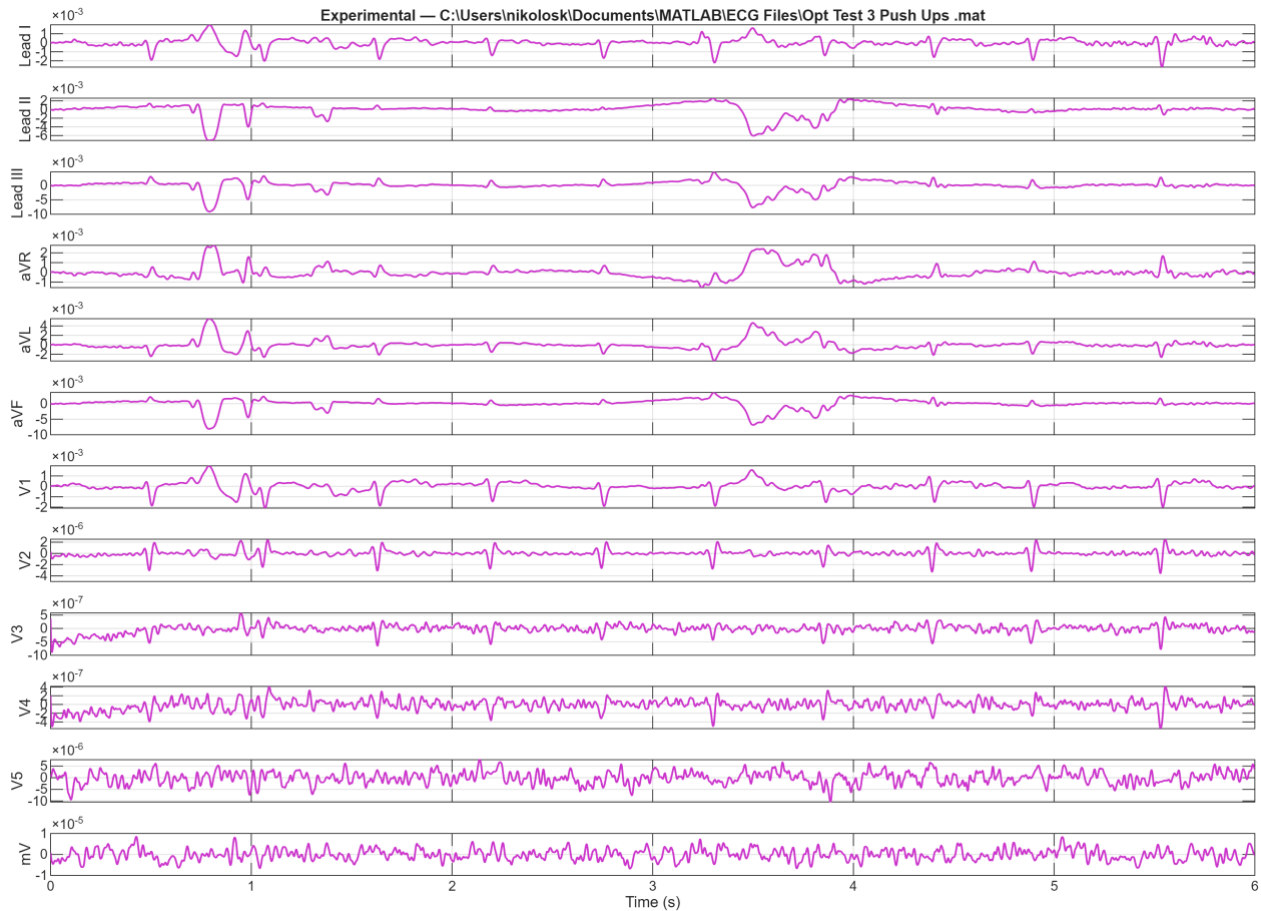


Figure 4.37 Experimental group test 3 – push-ups (12 lead stacked ECG). Segment shown corresponds to $t = 0$ s.

In the experimental group, the stacked ECG traces in Figure 4.37 show well-defined cardiac cycles similar to the control group, yet with greater stability. The QRS complexes remain sharp and of comparable amplitude, while the baseline wander is noticeably reduced. Minor low-frequency drift is still visible however it is smaller than in the control group. Importantly, the transient motion spikes seen in the control ECG are visibly attenuated under the experimental

condition. In other words, the experimental ECG waveform is more uniform beat-to-beat and is less perturbed by the push-ups.

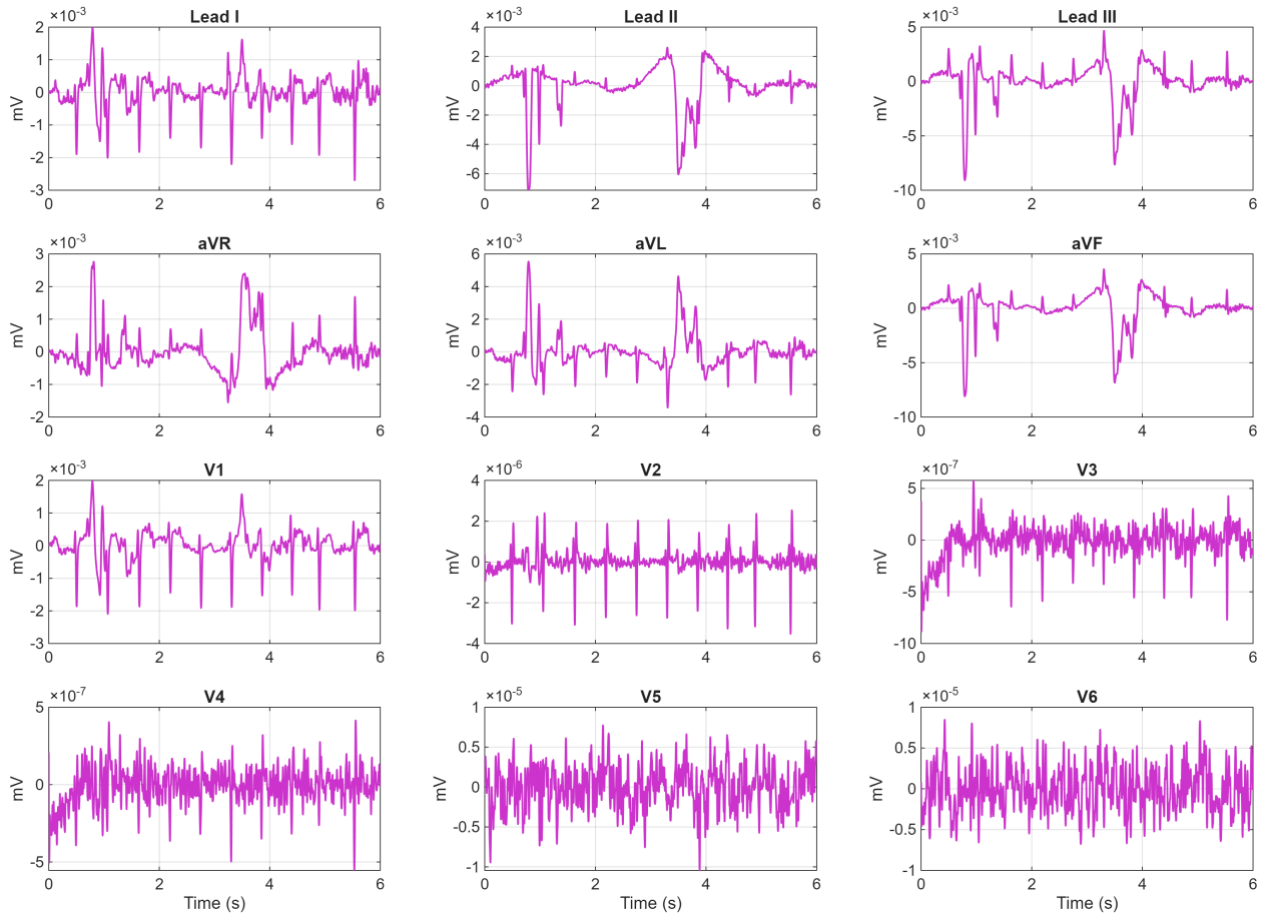


Figure 4.38 Experimental group test 3 – push-ups (ECG Grid View). Segment shown corresponds to $t = 0$ s.

The grid format Lead II demonstrated in Figure 4.38 for the experimental case shows a relatively flat baseline compared to control. Each heartbeat exhibits a clean P–QRS–T morphology with very little jitter. The experimental trace has fewer high-frequency fluctuations and no obvious

artifacts, indicating that muscle/EMG noise is reduced in the recorded signal. No signal dropouts occur, and the entire ECG segment appears uninterrupted. In effect, the experimental ECG under motion is qualitatively cleaner. The baseline drift is minimal, and waveform shapes remain consistent.

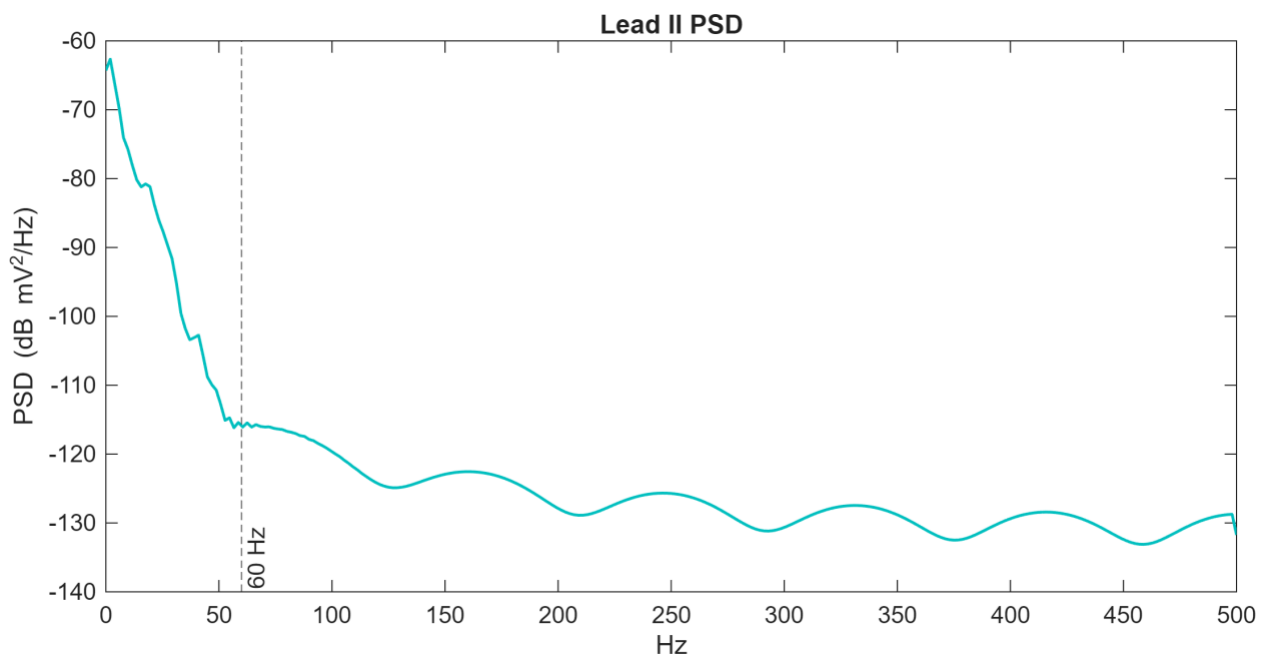


Figure 4.39 Experimental group test 3 – push-ups (power spectral density of lead II). Segment shown corresponds to $t = 0$ s.

The experimental Lead II trace shown in Figure 4.39 exhibits the principal peak at the cardiac frequency. The 60 Hz power-line peak is present however its relative amplitude is not higher than in the control group. The sub-0.5 Hz baseline power is also reduced which is consistent

with the observed steadier baseline. Overall, the experimental PSD retains the heart-rate harmonics although with a higher signal-to-noise ratio.

4.6.3 Comparison Results

This section analyzes the time-domain waveforms, stability over time, frequency-domain characteristics, and quantitative signal quality metrics. Explaining how each figure supports the improved performance of the experimental hydrogel from an electrophysiological perspective.

1. Resting State

Under resting conditions, the experimental hydrogel produced more stable and repeatable ECG signals compared to the control. This is clearest in the stacked waveform data, where the experimental traces maintain consistent R-peak amplitude and timing across multiple cardiac cycles. Whereas the control traces show beat-to-beat variability and subtle baseline drift. These inconsistencies in the control suggest motion-induced impedance changes. In Figure 4.40, the experimental waveforms rise and fall in near-perfect alignment over time. The control group, by contrast, demonstrates sagging between beats and irregular peak height, indicating that the signal is affected by minor motion or unstable conduction.

Both hydrogel groups resolve the P QRS T sequence across all twelve leads. The distinction between materials is most apparent in the limb leads and augmented leads of Figure 4.41. In Lead II and Lead III, the experimental hydrogel presents steadier baselines and a more repeatable beat-to-beat morphology than the control. The control traces show slow baseline excursions and small amplitude fluctuations. The augmented leads (aVR, aVL, aVF) show a similar pattern. The experimental waveforms sit on a flat baseline, while the control waveforms meander around zero with visible low-frequency drift. In the precordial set the difference is most obvious in V4–V6.

The spectral view depicted in Figure 4.42 isolates how each interface treats physiological content and external interference. In the 0.5–40 Hz cardiac band, both materials capture the expected energy distribution. The experimental curve remains at least comparable in magnitude while exhibiting a lower line component at 60 Hz.

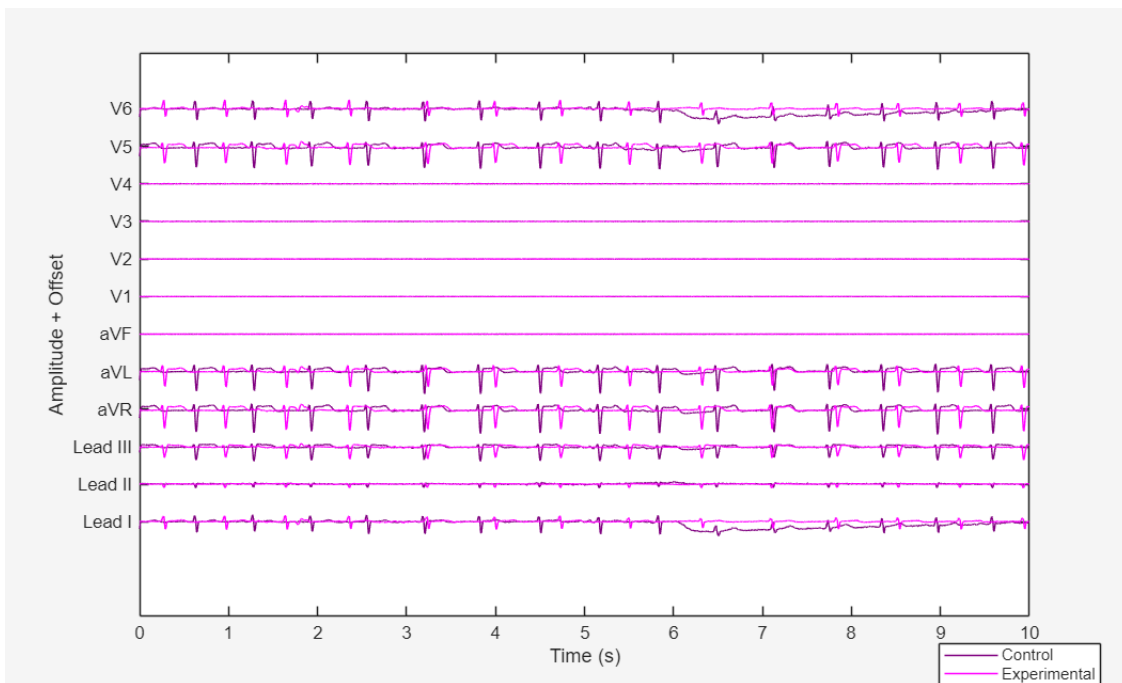


Figure 4.40 Test 1- at rest (stacked comparison graph)

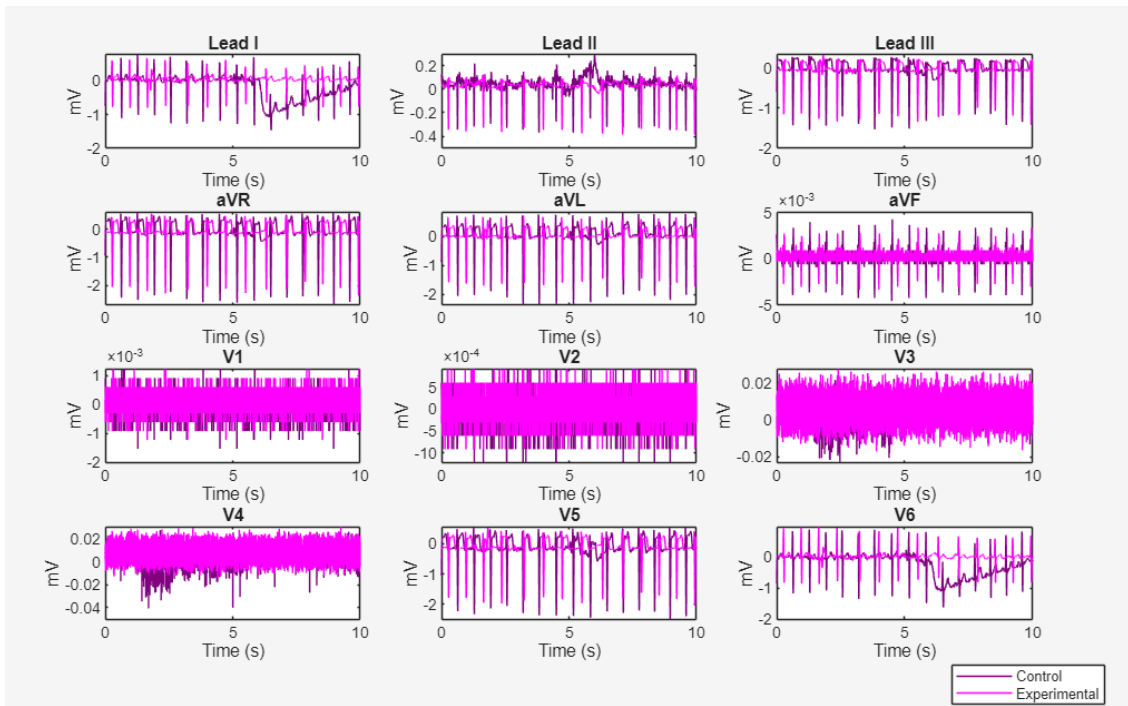


Figure 4.41 Test 1- at rest (12-lead grid comparison graph)

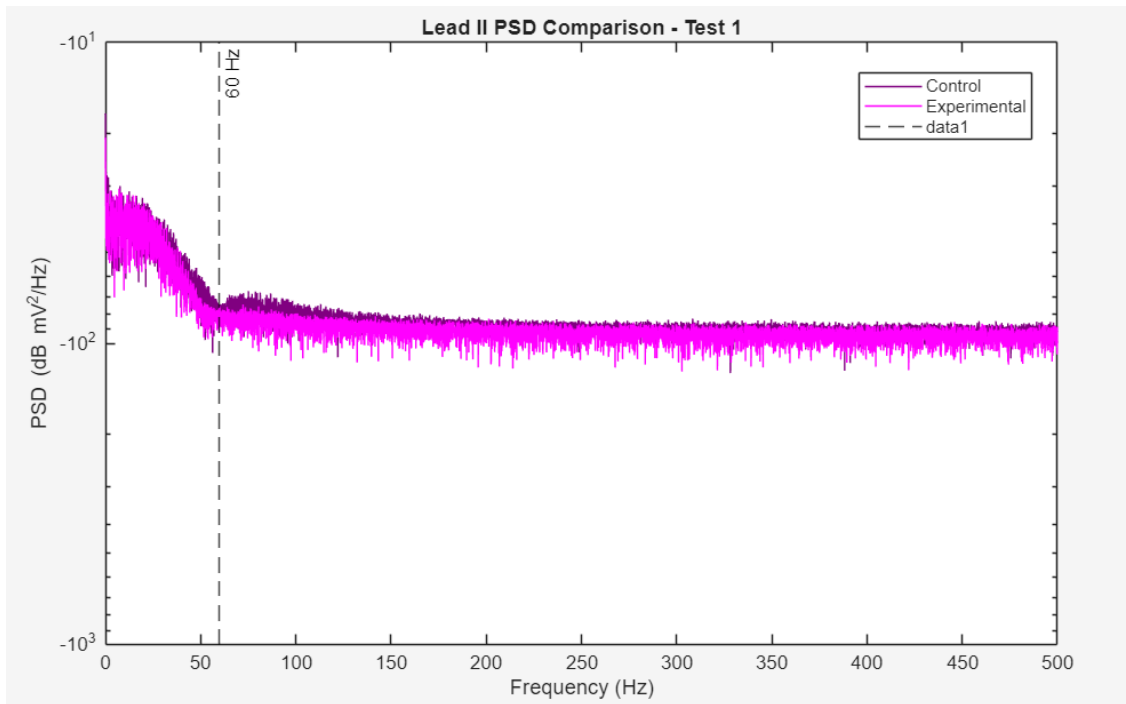


Figure 4.42 Test 1- at rest (PSD lead II comparison graph)

Quantitative differences are summarized in Table 4.2. The experimental hydrogel reduced baseline wander by 51.8% and 60 Hz noise by 4.78 dB relative to the control. This data is consistent with the flatter lines seen in Figures 4.40 and 4.41 and the smaller interference spike in Figure 4.42. The coefficient of variation in R-peak amplitude dropped by 238%, reflecting the consistent waveform heights seen in the stacked view of Figure 4.41. Although the slope index and SNR were slightly lower, the overall signal stability was improved for the experimental hydrogel.

Performance Summary – Test 1	
Δ SNR (avg across 12 leads)	-0.85 dB
60 Hz reduction (Lead II)	+4.78 dB
Baseline wander reduction	+51.82 %
QRS sharpness gain	-13.53 %
Cross-lead uniformity gain	+238.30 %

Table 4.2 Performance summary of test 1.

2. Squat Activity (10 continuous standing squats)

During the squatting motion, the experimental hydrogel maintains higher ECG signal fidelity than the control hydrogel. This is evident in Figure 4.43, where all control traces show pronounced baseline wander and occasional waveform distortion with each squat. For instance, the baseline in many leads drifts up and down. Whereas the experimental group traces remain much more stable and the baseline stays nearly flat.

With the control hydrogel, some leads especially those on the limbs exhibit irregular deflections and noise spikes. By comparison, all leads using the experimental hydrogel retain clear, well-defined waves with minimal distortion. These time-domain observations seen in Figure 4.44 suggest that the experimental hydrogel’s strong skin adhesion and conductivity suppress motion-induced artifacts.

The PSD comparison presented in Figure 4.45 shows that the experimental electrode significantly lowers noise power at frequencies associated with motion. At very low frequencies reflecting

baseline wander in the 0–1 Hz range. The control ECG has a high spectral density namely a signature of large baseline swings during squats whereas the experimental hydrogel’s spectrum in this region is much flatter, indicating ~48% less baseline drift. In effect, the experimental hydrogel prevents mains hum and motion harmonics from contaminating the signal.

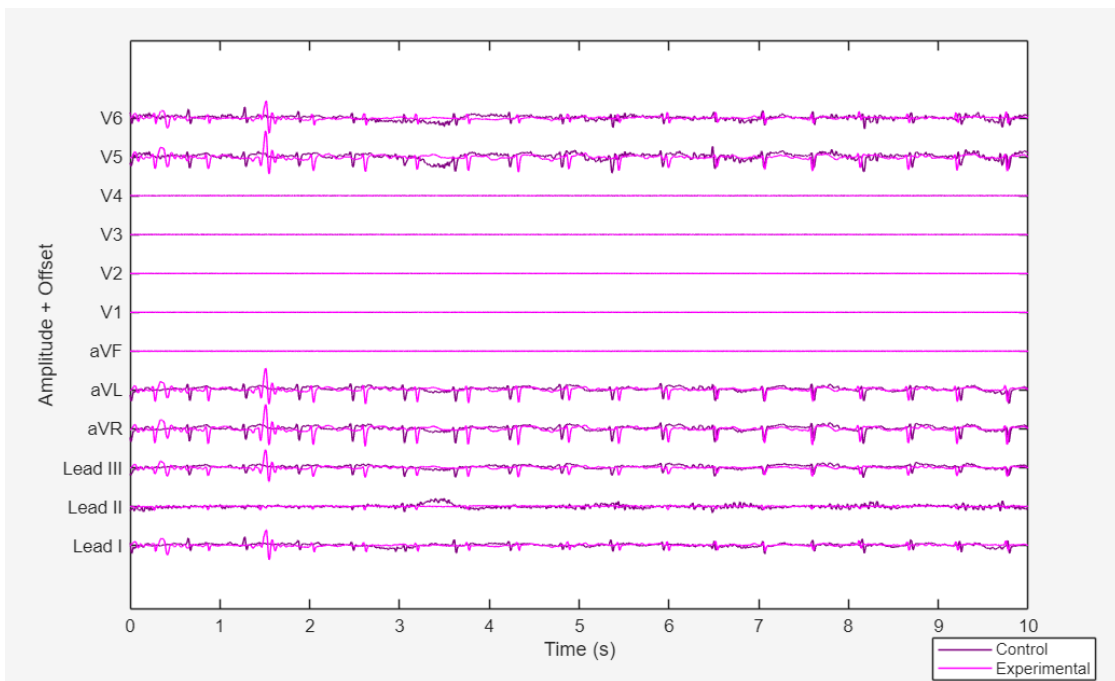


Figure 4.43 Test 2- squats (stacked comparison graph)

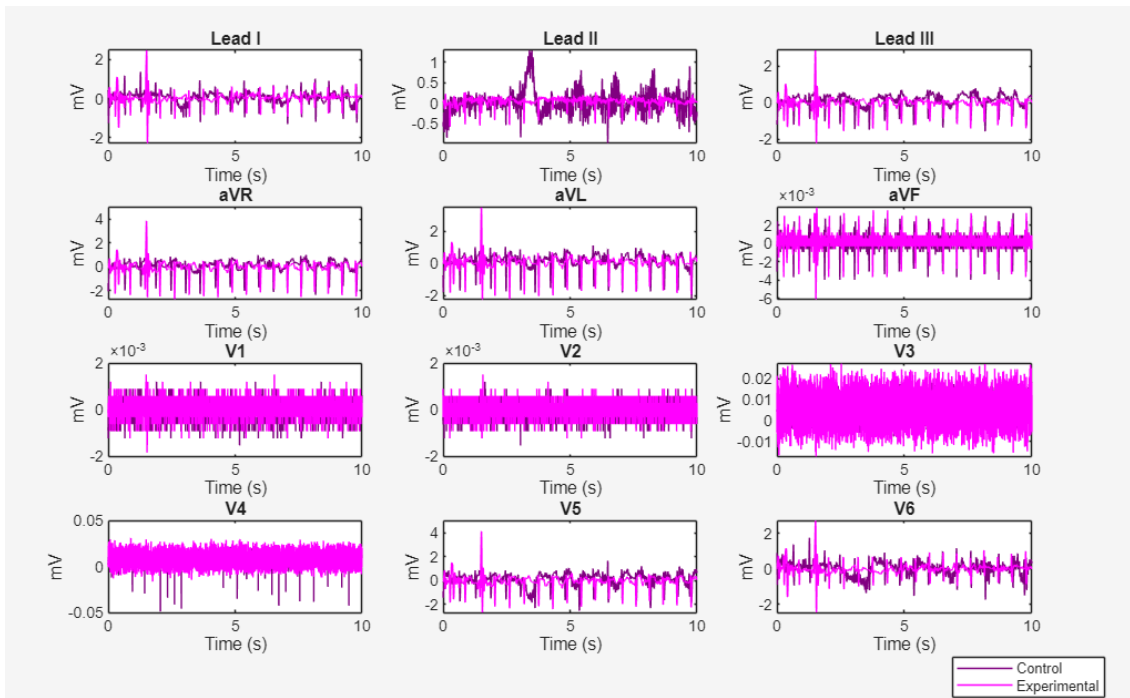


Figure 4.44 Test 2- squats (12-lead grid comparison graph)

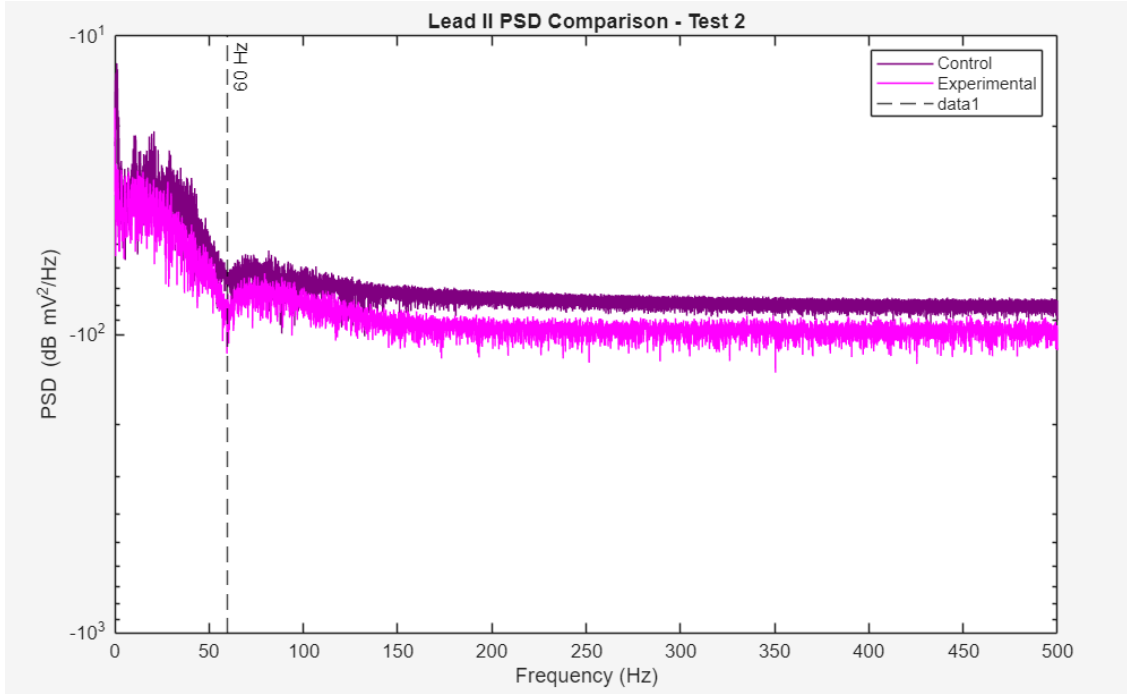


Figure 4.45 Test 2- squats (PSD lead II comparison graph)

Quantitative metrics from the summary table shown in Table 4.3 unambiguously show that the experimental hydrogel electrodes outperformed the control in every category during the squat test. On average, the experimental hydrogel recordings achieved a higher signal-to-noise ratio

compared to the control, meaning the ECG signals were captured more cleanly over the noise. The hydrogel also dramatically cut down interference for instance, the 60 Hz noise power was lower by on the order of 15–17 dB relative to the control electrodes. This indicates a much smaller hum in the signal. Baseline wander was reduced nearly half the amplitude of drift vs. the control. The hydrogel also preserved high-frequency details of the heartbeat better than the control. Finally, these improvements were uniform across all 12 leads. The cross-lead signal uniformity improved by over 40%, showing that every lead benefited similarly from the hydrogel interface.

Performance Summary – Test 2	
Δ SNR (avg across 12 leads)	+3.30 dB
60 Hz reduction (Lead II)	+16.64 dB
Baseline wander reduction	+47.89 %
QRS sharpness gain	+38.75 %
Cross-lead uniformity gain	+23.82 %

Table 4.3: Performance summary of test 2.

3. Push Up Activity (10 full pushups)

The experimental hydrogel electrode produces visibly cleaner ECG waveforms than the control during pushups. In a direct time-domain overlay of all 12 leads portrayed in Figure 4.46, the experimental hydrogel trace exhibits consistently sharp and well-defined cardiac complexes, whereas the PDA-PAM control shows slight distortion and noise superimposed on the signal. Smaller features such as P-waves and T-waves are more discernible with the experimental hydrogel.

The per-lead ECG analysis showcased in Figure 4.47 further demonstrates the advantage of the experimental hydrogel in maintaining consistent signal quality across all channels. With the experimental hydrogel, each lead produced QRS complexes with matching form and amplitude. Baseline levels remained stable throughout the recording. In the control data, however, there was a clear lack of uniformity one lead showed significant baseline drift. This was likely triggered by a brief contact loss during movement, and variations in R-wave amplitude were evident between several leads. These discrepancies suggest weaker adhesion or inconsistent mechanical contact in the control configuration, which would make individual leads more susceptible to movement artifacts.

Analyzing the PSD of lead II presented in Figure 4.48 reveals spectral advantages in using the experimental hydrogel. The control trace shows a sharp peak at 60 Hz whereas the experimental hydrogel cuts this component by over 10 dB, reflecting a significant drop in AC noise pickup. Across the broader frequency range, the hydrogel maintains a consistently lower noise floor. Baseline drift, visible in the sub-1 Hz region, is also attenuated, supporting earlier time-domain observations of a steadier ECG line. In the 5–40 Hz band, where QRS energy

dominates, the hydrogel preserves more spectral power, pointing to its ability to retain the fast transitions of the heartbeat.

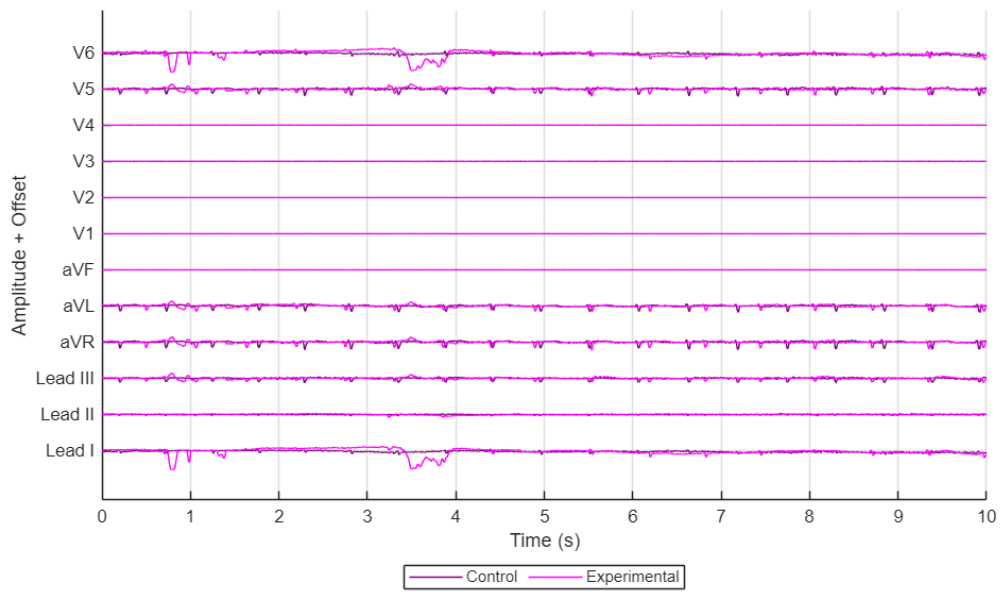


Figure 4.46 Test 3- push-ups (stacked comparison graph)

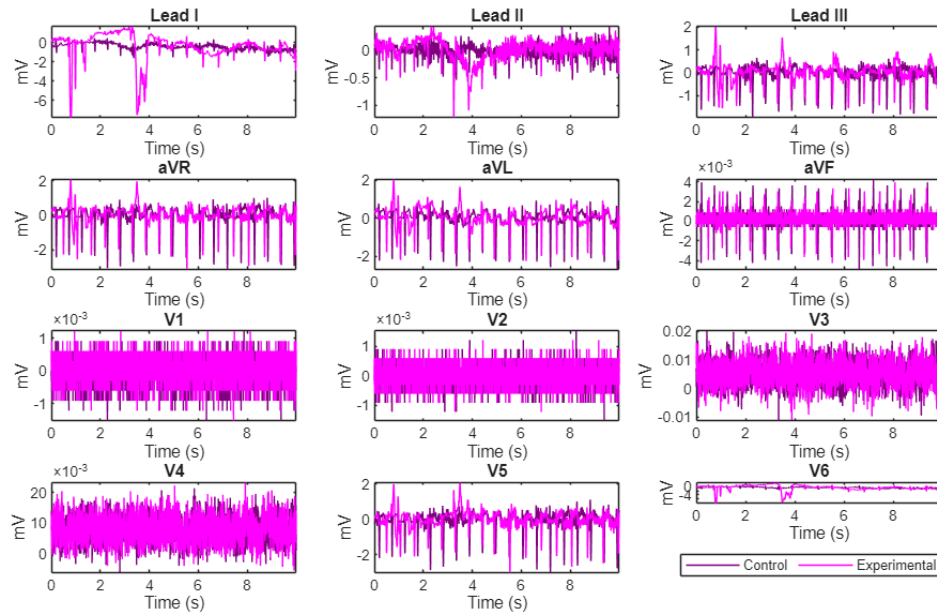


Figure 4.47 Test 3- push-ups (12-lead grid comparison graph)

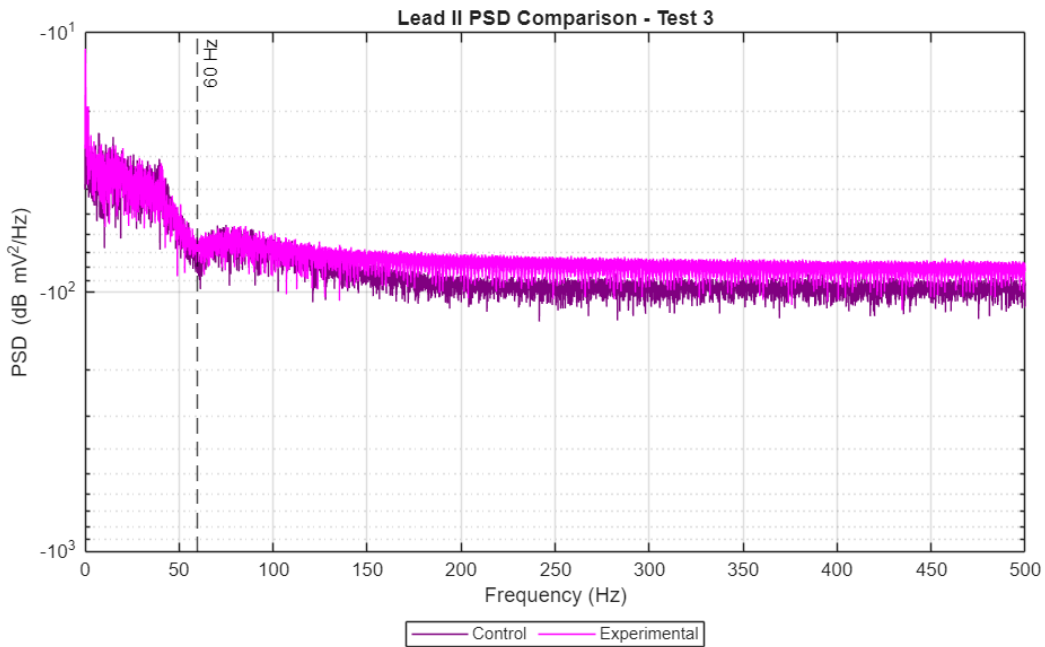


Figure 4.48 Test 3- push-ups (PSD lead II comparison graph)

The quantitative performance summary showcased in Table 4.4 shows the experimental hydrogel achieves a higher signal-to-noise ratio about a 5 dB gain on average across the 12 leads relative to the control. This indicates that the true cardiac signal was captured much more cleanly above the background noise. Consistent with visual observations, the experimental hydrogel also reduced baseline wander amplitude by roughly 54%, demonstrating a far more stable baseline during pushups. Likewise, QRS sharpness is enhanced by ~139% with the experimental material, more than doubling the clarity of the R-wave upstroke compared to the control. Furthermore, the cross-lead uniformity improved dramatically the variability between different leads' signals dropped by over a factor of three. This reflects that no single electrode placement with the experimental hydrogel was a weak link.

Performance Summary – Test 3	
Δ SNR (avg across 12 leads)	+5.04 dB
60 Hz reduction (Lead II)	-10.54 dB
Baseline wander reduction	-53.78 %
QRS sharpness gain	+138.97 %
Cross-lead uniformity gain	-214.02%

Table 4.4: Performance summary of test 3.

CHAPTER 5: CONCLUSION

5.1 Summary of Findings

In this study, a PDA–PAM hydrogel composite incorporating Fe_3O_4 , xGNP, and LiCl was synthesized and tested to reproduce the compliance, conductivity, and adhesive characteristics of natural skin. To identify an optimal formulation, six doped variants of the PDA–PAM hydrogel were prepared. Fe_3O_4 , graphene, and LiCl each influence a different property of the hydrogel, and their combined use leads to outcomes that do not occur in one- or two-dopant systems. Pairs of dopants ($\text{Fe}_3\text{O}_4 + \text{xGNP}$, $\text{xGNP} + \text{LiCl}$, or $\text{Fe}_3\text{O}_4 + \text{LiCl}$) each lacked one essential function: ionic transport, electronic conduction, or structural cohesion. Only the full trio combined all three, reducing skin impedance and preserving contact under strain, which enabled consistent high-quality signal capture. Final ratios were set at 1 wt% Fe_3O_4 , 0.5 to 1 wt% xGNP, and 1–2 M LiCl, resulting in a total salt content near 5–10% by weight. Comparative testing between the final $\text{Fe}_3\text{O}_4/\text{xGNP}/\text{LiCl}$ (2.8 wt%) @ PDA–PAM hydrogel and the PDA–PAM control revealed notable improvements in material performance. During synthesis, both hydrogels formed successfully via in-situ dopamine polymerization and acrylamide crosslinking, turning from a clear solution to a darkly colored gel as PDA developed. The $\text{Fe}_3\text{O}_4/\text{xGNP}/\text{LiCl}$ (2.8 wt%) @ PDA–PAM hydrogel assumed a deeper black-brown hue compared to the control's translucent coffee-brown. Although both remained pliable, the experimental hydrogel had a more resilient tactile feel. This qualitative difference foreshadowed a few of the quantitative improvements observed in the composite material.

The SEM micrographs revealed how the experimental hydrogel's internal architecture differed from the control. The PDA–PAM control exhibited a porous and open-cell structure typical of soft polyacrylamide gels. Its pores were irregular and relatively large reflecting the

loosely crosslinked single-network matrix. As opposed to the experimental hydrogel showed a denser and more homogeneous microstructure. The pore sizes in the composite were generally smaller and uniformly distributed. There was also no evidence of large agglomerates from the Fe₃O₄ NPs and xGNPs. Both were well dispersed and confirmed by the even texturing of the SEM images.

Self-healing tests showed that the experimental hydrogel could fully restore its structure after damage. A Fe₃O₄/xGNP/LiCl (2.8 wt%) @ PDA–PAM sample that was cut and rejoined healed completely within 12 hours at room temperature. The healed gel stretched like an uncut sample and did not fail at the original cut, indicating complete recovery of strength. This regeneration results from dynamic hydrogen, π – π , and Fe³⁺ coordination bonds, aided by LiCl's moisture retention that promotes chain reconnection. The recovery was similar in extent to that of the PDA–PAM control.

Mechanically, the PDA–PAM control was highly stretchable, whereas the experimental composite traded extensibility for added stiffness. Under uniaxial tension, the control hydrogel stretched from an initial length of 1.2 cm to approximately 30.9 cm before failure. This corresponds to an elongation of about 2475 %, more than 25 times its original length. The experimental hydrogel reached a maximum length of 23 cm from a 1.3 cm starting point, resulting in a total strain of roughly 1670 % or 17.7 times its initial length. This reduction in stretchability reflects the taut filler polymer interactions introduced by the Fe₃O₄ nanoparticles and graphene. The nanofillers restrict polymer chain mobility and act as stress concentrators prompting earlier rupture. Stress strain curves confirm that incorporating conductive fillers makes the hydrogel appreciably stiffer and less extensible than the PDA–PAM alone. The control's stress–strain

response had a lower initial slope and a long, gradual extension, whereas the experimental hydrogel's curve rose steeply.

The $\text{Fe}_3\text{O}_4/\text{xGNP}/\text{LiCl}$ (2.8 wt%) @ PDA–PAM hydrogel retains the excellent adhesive properties imparted by PDA. Qualitative peel tests on diverse substrates, including plastic, glass, metal, cardboard, and foam, showed that it adhered as strongly as the PDA–PAM control. The presence of graphene, iron oxide, and salt did not diminish the sticky catechol-based surface bonding. Both hydrogels could attach firmly to smooth or rough surfaces and resist detachment. No significant difference in adhesion strength was observed between the control and experimental groups.

When evaluated for electrical performance, the experimental hydrogel achieved a DC conductivity of 0.60–0.65 S/m. Around fourfold higher than the salt-free PDA–PAM ~ 0.15 S/m. From a device perspective, this conductivity regime is well within the range necessary for low-impedance skin–electrode interfaces. Hydrogels doped with LiCl conducted significantly better than the PDA–PAM control and combining LiCl with Fe_3O_4 and xGNP only amplified this effect. Chronoamperometry results captured this well. Where the control gel's current dropped off quickly, the doped hydrogels sustained steady-state currents for longer and at higher levels. These results suggest that ionic mobility was vastly improved, while the network's structure remained conductive and stable. Cyclic voltammetry reinforced this, showing that even under repeated voltage sweeps, the hydrogels behaved consistently and without degradation. No new redox peaks emerged in the doped gels. This confirms that electrical performance improved without compromising the hydrogel's electrochemical integrity. Therefore, the $\text{Fe}_3\text{O}_4/\text{xGNP}/\text{LiCl}$ (2.8 wt%) @ PDA–PAM hydrogel is identified as the most promising candidate in this work for reliable bioelectrical signal acquisition in hydrogel-based electronic skin applications.

Comparative signal acquisition experiments confirmed finer sensing performance of the experimental hydrogel electrode relative to the PDA–PAM control. For example, ECG signals recorded with the experimental hydrogel showed a much sharper R-wave upstroke approximately 139% steeper in slope than that recorded with the PDA–PAM control. Furthermore, the overall signal quality improved. The experimental hydrogel’s ECG traces had about a 5 dB higher signal-to-noise ratio than the control, and the background 60 Hz mains noise was ~10 dB lower. These metrics collectively validate that the hydrogel’s optimized ionic and electronic pathways facilitate high-fidelity biopotential recording.

In summary, the final optimized formulation (PDA–PAM with LiCl, Fe₃O₄, and xGNP) exemplified a balance of properties. Demonstrating self-healing, strong tissue adhesion, softness, and excellent electrical performance. Together, these results validate that the developed biomimetic hydrogel interface is indeed a platform capable of faithfully capturing physiological signals, thereby fulfilling the central aim of this work.

5.2 Limitations

Achieving reproducibility in the hydrogel formulation was a consistent limitation throughout this work. Although Fe₃O₄ nanoparticles were introduced to improve conductivity, maintaining uniform dispersion across the gel matrix was difficult. A few samples showed signs of uneven particle distribution. In parallel, the formation of polydopamine relied on oxidation conditions that were not always perfectly controlled. The polymerization outcome was highly dependent on when and how dopamine was introduced, how long it was allowed to oxidize, and the pH environment during gelation. These factors, though seemingly minor, resulted in inconsistent PDA crosslinking and affected the final gel’s adhesive and mechanical properties. As

a result, identical synthesis procedures sometimes led to non-identical outcomes. This reveals the need for tighter control over both chemical and physical parameters in future iterations.

Following the variability observed in hydrogel synthesis, the custom tensile testing setup introduced its own challenges in obtaining consistent mechanical data. The custom tensile device captured essential stress–strain behavior but remained limited by its open-loop configuration. Without feedback correction, small shifts in step count or compliance led to deviations between commanded and actual displacement. Calibration was performed using motor step count and screw lead, which introduced further uncertainty during low-speed tests. The 22 N load cell’s resolution also imposed noise at very low forces. These constraints made it difficult to resolve subtle transitions in the elastic region and introduced small fluctuations in the recorded stress–strain curves. Environmental factors further compounded this uncertainty, as tests conducted in ambient air could not fully maintain hydrogel hydration. Even brief surface drying during mounting altered stiffness and fracture behavior, producing variation between trials. The inconsistencies noted during hydrogel synthesis and mechanical testing reveal how interdependent material fabrication and characterization truly are.

5.3 Future Research Directions

Building on the findings of this project and addressing the limitations above, several avenues are recommended for future work. Continued refinement of both synthesis precision and testing control will be necessary for producing reproducible hydrogel data and establishing a stronger foundation for future device integration. For one, enhancing the reproducibility of the hydrogel formulation is a priority. This can be achieved by imposing tighter control over chemical and physical synthesis parameters.

Another important avenue is honing the mechanical testing methodology to obtain more reliable data. The custom tensile tester could be upgraded to a closed-loop system with feedback control, that way the actual displacement matches the commanded displacement more accurately.

APPENDIX A: BUILD AND CONTROL INFORMATION OF TENSILE DEVICE

Mechanical Assembly

The frame is constructed from ten 1"×1" four-slot aluminum rails (12" length each) and two 2"×2" six-slot rails (30" length). These are joined by 28 corner brackets into a rectangular tower (eight rails in the main frame, two rails held aside for alternative test setups). A central vertical column houses the G1610 ball screw (10 mm lead, 800 mm travel), which is supported at the base and top to prevent bending. The ball screw is directly coupled to a NEMA-23 stepper motor (1200 RPM rating) via a keyed coupling. The motor is rigidly mounted to the base extrusion. Atop the ball screw a platform (with a Z-bracket) carries the 22 N load cell. The sample clamps attach to the load cell on one end and to the stationary base at the other, so that upward motion applies tension. All hardware (rails, brackets, screws) is secured so the entire assembly is stable under load. In alternative mode, reversing the clamps allows the same column to compress short cylindrical samples.

Electrical Wiring

Power is supplied by a Meanwell LRS-350-24 (24 V, 350 W) to accommodate the stepper driver’s voltage and current needs. The stepper driver (DM542T) pins and load cell are wired as shown in Table A.1.

Device	Pin / Signal	LabJack Connection	Notes
Stepper Driver	PUL+ (pulse+)	FIO0	Step signal input to driver
Stepper Driver	DIR+ (direction+)	FIO1	Direction control input to driver
Stepper Driver	PUL-, DIR-	GND	Common ground tied to LabJack
Stepper Driver	ENA+ (enable+)	(not used)	Driver defaults to active
Load Cell	Excitation (+)	DAC1 (0–2.4 V)	Provides excitation voltage
Load Cell	Excitation (-)	GND	Reference ground
Load Cell	Signal (+)	AIN0	Measurement channel
Load Cell	Signal (-)	AIN1	Differential measurement reference
Load Cell	Shield	GND	Noise shielding

Table A.1: Electrical connections between the LabJack T7-Pro, stepper driver, and load cell.

This configuration lets the LabJack drive the stepper and read the sensor. The LabJack provides up to ± 10 mA on FIO pins (sufficient to trigger the DM542T inputs), and provides the load-cell excitation current via DAC1. The excitation voltage is also fed back into analog input AIN2 for monitoring and calibration. A 17.6-gram reference weight is used for calibration: LabVIEW

applies a scale factor to convert the measured voltage difference into a force in Newtons. At the start of each test, the software tares the readings to zero out clamp and fixture offsets.

Software and Control

The control sequence begins with a Lua initialization script on the LabJack (see *Figure A.1*). This script configures the LabJack counters so that FIO0 and FIO1 output step and direction pulses continuously at the requested frequency and polarity. Once the counters are set, the stepper is free to run under LabVIEW control. The LabVIEW VI then provides the user interface (see *Figure A.2*). In the VI, the user selects “up” or “down” motion, enters a speed (in mm/s), and presses Start. LabVIEW computes the needed pulse frequency (using the 10 mm lead) and writes a value to a LabJack register that adjusts the counters. The VI simultaneously reads AIN0/AIN1 to get raw load-cell voltage, subtracts the tare offset, and converts it to force. Displacement is calculated from step count: each step moves the carriage by (lead/steps per rev). Strain is computed as $\Delta L/L_0$ (with L_0 from sample geometry input). The program plots force vs. displacement (or stress vs. strain) live, and logs data to an Excel/CSV file with timestamps.

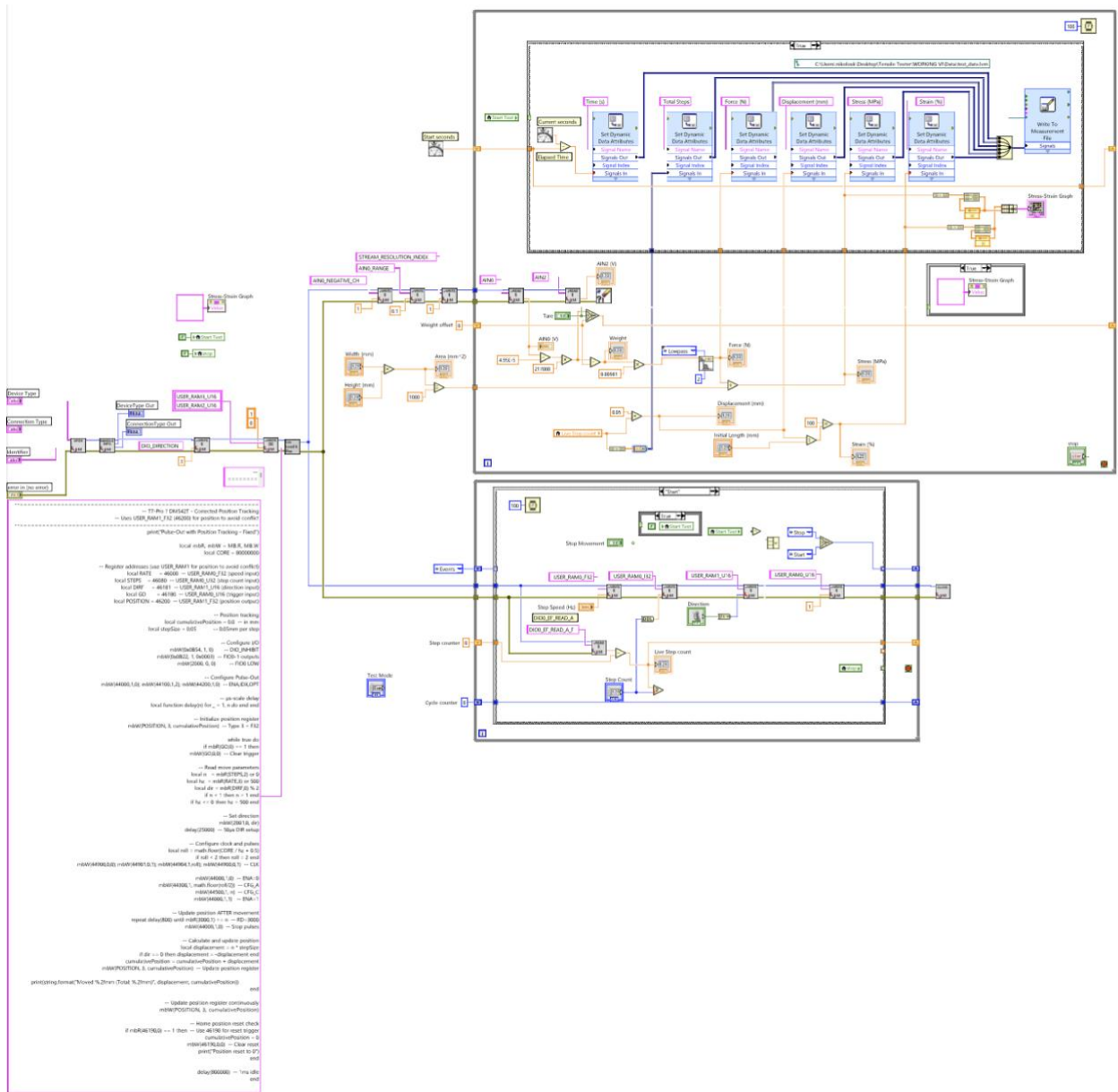


Figure A.1 Snapshot of the complete LabVIEW block diagram for the custom tensile testing VI. The VI coordinates Lua-script-based motor pulses with LabJack T7-Pro analog inputs to generate force–displacement data for hydrogel testing.

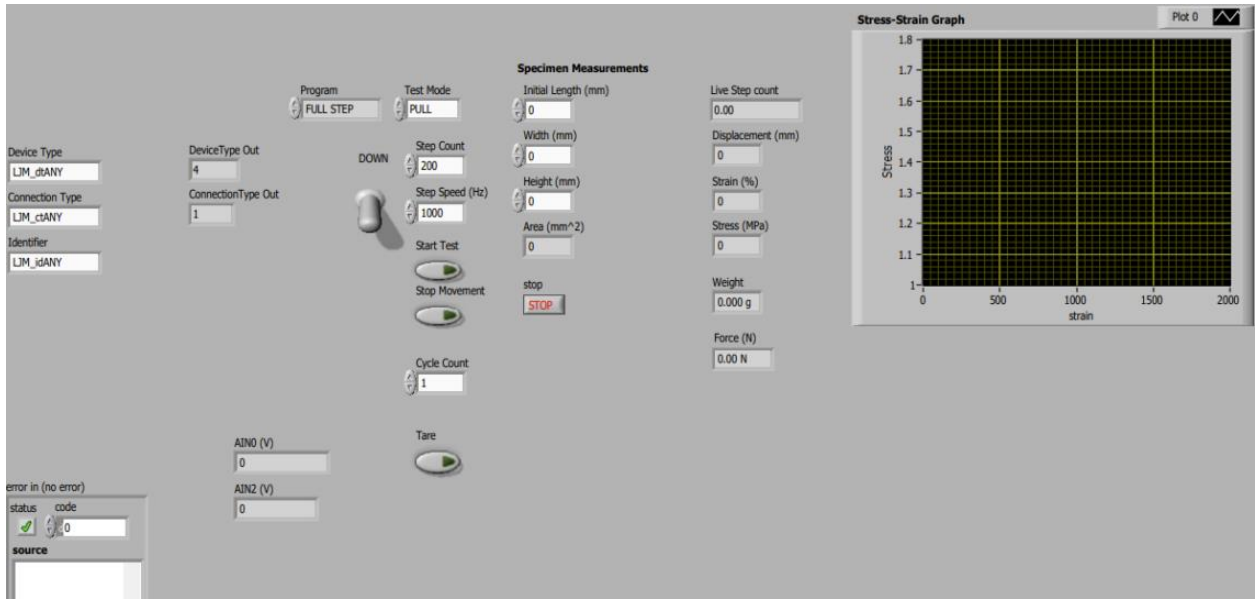


Figure A.2 Screenshot of the LabVIEW VI front panel during a test.

REFERENCES

- [1] Q. Han, C. Zhang, T. Guo, *et al.*, "Hydrogel nanoarchitectonics of a flexible and self-adhesive electrode for long-term wireless electroencephalogram recording and high-accuracy sustained attention evaluation," *Adv. Mater.*, vol. 35, art. 2209606, 2023, doi: 10.1002/adma.202209606.
- [2] Y. Gong, Y. Hu, Y. Cheng, *et al.*, "An electrically conductive polyvinyl alcohol/poly (acrylic acid-co-acrylamide)/polydopamine-decorated carbon nanotubes composite hydrogel with appropriate mechanical properties for human movement monitoring," *J. Mater. Sci.*, vol. 57, pp. 12947-12959, 2022, doi: 10.1007/s10853-022-07435-x.
- [3] A. Choi and B. Ben-Nissan, "Hydrogel for biomedical applications: 3D/4D printing, self-healing, microrobots, and nanogenerators," 2024, doi: 10.1007/978-981-97-1730-9.
- [4] Z. Jin, L. Yang, S. Shi, T. Wang, G. Duan, X. Liu, and Y. Li, "Flexible polydopamine bioelectronics," *Adv. Funct. Mater.*, vol. 31, art. 2103391, 2021, doi: 10.1002/adfm.202103391.
- [5] L. Han, L. Yan, K. Wang, *et al.*, "Tough, self-healable and tissue-adhesive hydrogel with tunable multifunctionality," *NPG Asia Mater.*, vol. 9, art. e372, 2017, doi: 10.1038/am.2017.33
- [6] S. Roy, K. A. Deo, H. P. Lee, J. Soukar, M. Namkoong, L. Tian, A. Jaiswal, and A. K. Gaharwar, "3D printed electronic skin for strain, pressure and temperature sensing," *Adv. Funct. Mater.*, vol. 34, art. 2313575, 2024, doi: 10.1002/adfm.202313575.

[7] X. Li, X. Zhao, R. Liu, H. Wang, S. Wang, B. Fan, C. Hu, and H. Wang, "Mussel-inspired PDA@PEDOT nanocomposite hydrogel with excellent mechanical strength, self-adhesive, and self-healing properties for a flexible strain sensor," *J. Mater. Chem. B*, iss. 12, 2024.

[8] E. Kaymazlar, C. Dikbas, G. H. Matar, *et al.*, "Self-healable and conductive mussel inspired PVA/borax@PDA–LiTFSI hydrogel-based self-adhesive for human motion sensor," *Polym. Bull.*, vol. 81, pp. 8751-8764, 2024, doi: 10.1007/s00289-023-05122-8.

[9] A. Salih, N. Roth, O. Buganim, and A. D. Pelosi, "A low-cost open-source uniaxial tensile system for soft tissue testing," *Hardware*, vol. 2, no. 4, pp. 292-305, 2024, doi: 10.3390/hardware2040015.

[10] S. J. M. Yazdi and J. Baqersad, "Mechanical modeling and characterization of human skin: A review," *Journal of Biomechanics*, vol. 130, Art. no. 110864, Jan. 2022, doi: 10.1016/j.jbiomech.2021.110864.

[11] D. M. Reilly and J. Lozano, "Skin collagen through the lifestages: importance for skin health and beauty," *Plastic and Aesthetic Research*, vol. 8, p. 2, 2021. [Online]. Available: <http://dx.doi.org/10.20517/2347-9264.2020.153>

[12] L. Hu, P. L. Chee, S. Sugiarto, *et al.*, "Hydrogel-based flexible electronics," *Adv. Mater.*, vol. 35, art. 2205326, 2023, doi: 10.1002/adma.202205326.

[13] P. Zhu, Z. Li, J. Pang, P. He, and S. Zhang, "Latest developments and trends in electronic skin devices," *Soft Science*, vol. 4, p. 17, 2024. [Online]. Available: <http://dx.doi.org/10.20517/ss.2024.05>

[14] A. Taghizadeh, M. Taghizadeh, M. K. Yazdi, P. Zarrintaj, J. D. Ramsey, F. Seidi, F. J. Stadler, H. Lee, M. R. Saeb, and M. Mozafari, "Mussel-inspired biomaterials: From chemistry to clinic," *Bioengineering & Translational Medicine*, vol. 7, no. 3, p. e10385, Aug. 2022, doi: 10.1002/btm2.10385.

[15] L. Han, L. Yan, M. Wang, K. Wang, L. Fang, J. Zhou, J. Fang, F. Ren, and X. Lu, "Transparent, adhesive, and conductive hydrogel for soft bioelectronics based on light-transmitting polydopamine-doped polypyrrole nanofibrils," *Chem. Mater.*, vol. 30, no. 16, pp. 5561-5572, 2018, doi: 10.1021/acs.chemmater.8b01446.

[16] H. Gao, Y. Han, M. Huang, J. Li, H. Sun, G. Li, L. Dong, X. Liu, C. Liu, and C. Shen, "Design of highly stretchable, self-adhesive ionic conductive hydrogels for wearable strain sensors," *Adv. Sensor Res.*, vol. 4, 2025, doi: 10.1002/adsr.202500005.

[17] F. Ji, M. Jiang, Q. Yu, X. Hao, Y. Zhang, J. Zhu, S. Luo, and J. Li, "Ionic conductive organohydrogel with ultrastretchability, self-healable and freezing-tolerant properties for wearable strain sensor," **Frontiers in Chemistry**, vol. 9, 2021, doi:10.3389/fchem.2021.758844.

[18] Y. Ren, X. Bai, M. Wang et al., "A photosensitive hydrogel based on a combination of iron tetraoxide and polydopamine," *Colloid Polym. Sci.*, vol. 303, pp. 313-326, 2025, doi: 10.1007/s00396-024-05351-x.

[19] T. Chen, Z. Zhang, X. Zhou, Z. Zhang, J. Liu et al., " Fe_3O_4 @PDA nanoparticle-doped smart hydrogel scaffold for osteochondral defect repair by synergistical stimulation," *Advanced Functional Materials*, 2025, doi: 10.1002/adfm.202501354

[20] J. H. Arrizabalaga, A. D. Simmons, and M. U. Nollert, "Fabrication of an economical Arduino-based uniaxial tensile tester," *J. Chem. Educ.*, vol. 94, no. 4, pp. 530-533, Apr. 2017, doi: 10.1021/acs.jchemed.6b00639.

[21] M. Kranjec, J. Korinšek, M. Ambrož, and R. Kunc, "Control system for a tensile-testing device using low-cost hardware and open-source software," *Strojniški vestnik - J. Mech. Eng.*, vol. 66, pp. 155-163, 2020, doi: 10.5545/sv-jme.2019

CURRICULUM VITAE

Daniela Nikoloska

dk.nikoloska@gmail.com

[daniela-nikoloska](https://www.linkedin.com/in/daniela-nikoloska)

Education

Master of Science in Engineering, Electrical Engineering

University of Nevada, Las Vegas

December 2025

GPA: 3.5

Bachelor of Science in Engineering, Electrical Engineering

University of Nevada, Las Vegas

May 2023

Minor in Mathematics

Research Experience

Graduate Research Assistant | University of Nevada, Las Vegas

June 2024 – Aug. 2024

- Conducted thesis research focused on conductive hydrogel development and characterization.
- Designed and developed a force tensile test device for material analysis.

Graduate Research Fellow | Nevada NASA Space Grant Consortium

Aug. 2023 – Aug. 2024

- Comprehensive Study Using Sonic-Powered Microgravity-Assisted Tissue Chips to Simulate Space Radiation Effects on the Human Immune System.

Undergraduate Research Assistant | University of Nevada, Las Vegas

Jan. 2022 – May 2023

- Conducted Extensive Research in the Field of Acoustic-Levitated Microgravity Simulator and Organ-On-a-Chip Design, Evaluation, and 3D Manufacturing.

University Projects

Text and Emotion Recognition Design Project

Aug. 2022 – May 2023

- Developed NuSpex, a biomedical device intended to enhance the daily life and independence of visually impaired and blind individuals by enabling them to read everyday texts such as signs, labels, and instructions.
- Incorporated a real-time emotion recognition technology, providing social cues to users by interpreting emotions on people's faces.

Frequency Sound Generator Design Project

Nov. 2021 – Dec. 2021

- Designed, simulated, and tested a tone generator circuit system using LTspice.

Work Experience

Server | Park on Fremont

Jun. 2025 – Oct. 2025

- Provide fast-paced table service in a high-volume, nightlife-focused restaurant and bar.
- Handle guest interactions, take complex orders, and process transactions using POS systems.

Graduate Teacher Assistant | University of Nevada, Las Vegas

Jan. 2025 – May 2025

- Served as a teaching assistant for EE 360 Signals and Systems I under Dr. Ebrahim Saberinia, supporting a class of 30 students.
- Graded student homework, quizzes, and exams for the lecture section.
- Taught the lab section of the course every week and assigned MATLAB computer assignments.

Graduate Teacher Assistant | University of Nevada, Las Vegas

Aug. 2024 – Dec. 2024

- Served as a teaching assistant for CPE 200 Digital Logic Design II under Dr. Sarah Harris, supporting a class of 64 students.
- Graded student homework and conducted weekly office hours to provide additional assistance.

Learning Center Instructor | Sapience

Oct. 2023 – Jan. 2024

- Provided individualized tutoring in higher-level mathematics to students in grades K-12.

Electrical Engineering Intern | VisionAid

May 2023 – Aug. 2023

- Designed the prototype of CaneIQ, an assistive device that improves the mobility of visually impaired individuals.

Server | Hofbräuhaus

Jun. 2022 – Oct. 2022

- Provided efficient service in a high-volume, Bavarian-themed restaurant.
- Processed orders using digital POS systems and handled daily cash transactions.

Server | Sakamoto

Jan. 2017 – Jan. 2019

- Accurately memorized complex orders and delivered exceptional service in a family-style Japanese restaurant.
- Worked collaboratively with kitchen staff to ensure timely food delivery and high guest satisfaction.

Presentation

Nikoloska D, Comprehensive Study Using Sonic-Powered Microgravity-Assisted Tissue Chips to Simulate Space Radiation Effects on the Human Immune System, *NASA Nevada EPSCoR Statewide Meeting*, 2024 April 19, Las Vegas, NV

Awards

NASA Space Grant Graduate Fellowship

2023 – 2024

- Awarded a competitive fellowship to support graduate research in the field of space science and technology.

Roy and Helen Kelsall Engineering Scholarship

2023 – 2024

- Received a merit-based scholarship to support graduate studies in the field of engineering.

Differential Fees Undergraduate Scholarship

2022 – 2023

- Awarded a scholarship based on academic achievement and financial need to support undergraduate studies in engineering.

Wolzinger Family Engineering Scholarship

2021 - 2022

- Received a scholarship recognizing academic excellence and potential in the field of engineering.

Academic Activities

GPSA Council Representative | University of Nevada, Las Vegas

Jan. 2024 – May 2025

- Graduate & Professional Student Association (GPSA) Council Representative for the Electrical and Computer Engineering department.

RebelSat Member | University of Nevada, Las Vegas

Jan. 2023 – May 2023

- Member of the avionics team, contributing to developing a small satellite project.

Skills

- **Programming Languages:** C/C++, Python, RISC-V Assembly, System Verilog, LabVIEW

- **Microcontroller Platforms:** Arduino, Raspberry Pi, NVIDIA Jetson Nano, FPGA

- **3D CAD Design Software:** SolidWorks

- **Electrical Engineering Software:** LTspice, MATLAB, Multisim

- **Nano/Micro Biomaterials Characterization:** Electrical Impedance Spectroscopy (EIS), Fourier Transform Infrared Spectroscopy (FTIR), Scanning Electron Microscope, Fluorescence Spectroscopy
- **Languages:** English, Spanish (intermediate), and Macedonian (intermediate)

Professional Organizations

IEEE Engineering in Medicine and Biology Society

2022 - Present

Biomedical Engineering Society

2022 –Present

IEEE Institute of Electrical and Electronics Engineers

2022 –Present